ABSTRACT

Title of Document: MOLECULAR DYNAMICS STUDIES OF ORGANIC-COATED NANO AEROSOLS

Purnendu Chakraborty, Ph.D., 2008

Directed By: Professor Michael R. Zachariah, Departments of Mechanical Engineering and Chemistry

Atmospheric aerosols play an important role in atmospheric processes. These aerosol particles can affect climate through scattering, transmission and absorption of radiation as well as acting as cloud condensation nuclei. It has recently been found that fatty acids reside on the surfaces of marine and continental aerosols. In this research, an attempt has been made to understand the structures and properties of such organic coated aerosols using Molecular Dynamics simulation. The model particle consisted of a water droplet coated with fatty acid. The density profile (using both Coarse-Grained and Atomistic/United atom models) demonstrated that such aerosol particles have an inverted micelle structure consisting of an aqueous core and with the hydrophobic hydrocarbon tails exposed to the atmosphere. For smaller chains, with the organic molecules directed radially outwards from the water – organic interface) the normal pressure profile showed that the organic coating is under tension resulting in a 'negative' surface tension. As a result, such particles would have an inverse Kelvin vapor pressure effect and would be able to process water vapor despite the hydrophobic surface.

Following the work on surface tension, the rate of water uptake by coated aerosols was computed. It was found that the sticking coefficient of water vapor on

such particles was about a sixth of that on pure water droplets. This may seem to imply that the net condensation rate is lower, but we also need to take into account the evaporation of water from such particles. With a significant reduction in the evaporation rate (the coating lends greater stability to the particle resulting in reduced evaporation rate), the equilibrium vapor pressure of water on such particles reduced, resulting in a "net water attractor". Thus if such structures were created in sufficient concentration, they might be important contributors in the cloud condensation process.

Next the effect of longer Fatty acid molecules and branched surfactants on the structure and properties of coated particles was studied. It was found that in either case, due to stronger organic – organic interactions, the surfactant molecules tend to align themselves parallel to each other forcing local flattening of the underlying water substrate and consequently such particles behaved in a manner consistent with an "oily" drop, in sharp contrast to the case of shorter chains, where the particle was a "net water attractor".

Finally, the effect of organic coating on the Stokes drag of functionalized nanoparticles was studied. This work was motivated by a recent experimental study in which the thickness of Self Assembled Monolayers on Gold nanoparticles was characterized using a measurement process that relies on the determination of the size of a charged particle through knowledge of the drag force. The thickness of the coating was found to ~35% less than that predicted by a rigid core-shell model. This suggests that the functionalized Au-NP would have an inverted micelle structure. The MD simulations showed that the drag on the coated particle was indeed less than that on the corresponding pure particle, consistent with the experimental observation.

MOLECULAR DYNAMICS STUDIES OF ORGANIC-COATED NANO AEROSOLS

By

Purnendu Chakraborty

Dissertation submitted to the Faculty of the Graduate School of the
University of Maryland, College Park, in partial fulfillment
of the requirements for the degree of
Doctor of Philosophy
2008

Advisory Committee:
Dr. Michael R. Zachariah, Chair
Dr. Russell R. Dickerson
Dr. Harland M. Glaz
Dr. George W. Mulholland
Dr. John D. Weeks

To

My parents

Sanyukta and Biswanath Chakraborty,

And my wife

Shamita.

Thank you for your unconditional love and support. Thank you for your unwavering faith and absolute belief in my abilities. You have sacrificed so much and waited so long for this moment to come true and I dedicate this thesis to you.

Acknowledgements

First and foremost, I thank my thesis advisor, Professor Michael R. Zachariah, for guiding me during my PhD research. I still remember the day when I first walked me into his office and he drew a circle with jagged lines arranged ‘radially outwards’. That was the starting point of this research. Without his invaluable ideas, strategic insights and probing questions this thesis would not have been possible.

I would like to thank Dr. Takumi Hawa for helping me get started with Molecular Dynamics and Dr. Michael Shay for teaching me the nitty-gritty of parallel programming. A special thanks to my fellow group members who have made this journey thoroughly enjoyable.

I would like to thank Professors Russell R. Dickerson, Harland M. Glaz, George W. Mulholland and John D. Weeks for serving on my Ph.D. committee.

Table of Contents

List of Tables

List of Figures

1 Introduction

1.1 Aerosols

Aerosols are tiny liquid or solid particles suspended in the atmosphere. Their sizes can vary from a few nanometers to several hundreds of micrometers and they can affect the environment. Aerosols scatter sunlight resulting in reduced visibility[1, 2]. They also absorb sunlight and IR radiation resulting in warmer air in the atmosphere where they reside, which could suppress the formation of clouds[2]. There has been wide realization of the effect aerosols have on Earth's radiation balance. Incoming sunlight is mainly in the visible range. Earth's surface being much cooler than the sun, the radiated energy is primarily in the infrared range. The atmosphere absorbs this long wave energy more effectively. The Greenhouse gases (water vapor, carbon dioxide, methane, nitrous oxide, ozone) in the atmosphere radiate the long wave energy back to Earth's surface. Such emission of greenhouse gases results in an increase in surface temperature (the 'greenhouse effect') and affect climate[2, 3, 4]. Aerosol particles influence global climate and climate change by moderating or intensifying greenhouse gas effects, through absorption and scattering of sunlight. Acting as Cloud Condensation Nuclei (CCN), they can modify the radiative properties of clouds[3]. Cloud droplets require an aerosol particle (nucleus) to grow on. Hygroscopic materials are efficient as growth nuclei as are mineral dust and combustion products coated with hygroscopic materials. The composition of CCN thus plays an important role in cloud formation. The number and size distributions also have a major impact. Increased concentration of CCN results in a larger number of cloud droplets with reduced droplet size. Increased scattering within the cloud results in higher cloud al-

bedo (measure of reflectivity of cloud). Furthermore, clouds laden with more and smaller droplets persist longer in the atmosphere, having more time to exert their effect[3]. Thus the knowledge of the structure, composition and properties of aerosols is of utmost importance as they may significantly affect the processing of water vapor in the atmosphere, cloud formation and the radiation balance of the earth.

1.2 Organic Aerosols

Marine aerosols play an important role in many atmospheric processes[5]. Sea-salt aerosols are formed either by bubbles bursting during whitecap formation due to surface wind, or through sea spray[5]. It is believed that as marine aerosols form, they acquire a coating of organic origins[6-9]. There has only been indirect evidence supporting this theory based on the fact that amphiphilic molecules can self-assemble as monolayers at air/water interfaces[10, 11]. In a recent work, Tervahattu et. al.[12] found, using Time-Of-Flight Secondary Ion Mass Spectrometry (TOF-SIMS), evidence of palmitic (hexadecanoic) acid distribution on small particles. Their results showed that fatty acids are important ingredients on the surface of marine aerosols. In a subsequent work[13], the presence of fatty acid population on a variety of continental aerosols was reported. Using TOF-SIMS, fatty acids of carbon chain lengths up to C32 acids were found on sulfate aerosols.

1.2.1 Model

A chemical model for the composition, structure and atmospheric processing of organic aerosols has been suggested[9]. The model is stimulated by field measurements showing that organic compounds are a significant component of atmospheric

aerosols. The proposed model organic aerosol is an **inverted micelle** consisting of an aqueous core encapsulated in an inert, hydrophobic organic monolayer. The organic materials that coat the aerosol particles are surfactants of biological origin. The model is sketched in Figure 1.1 and is a film of hydrophobic hydrocarbons covering an aqueous particle. **The proposed model emphasizes that all of the hydrophobic organics will be on the surface of the aerosol and not dissolve within the droplet.**

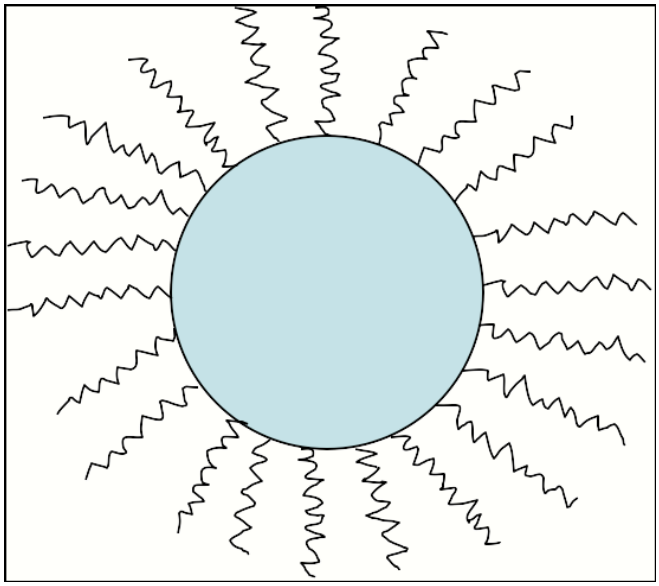

Figure 1.1: Inverted Micelle model for Organic Aerosols (adapted from Ref. 14)

In this model, the surfactants lie with their polar heads inserted into the ionic aqueous core with their hydrophobic hydrocarbon tails exposed to the atmosphere. Indeed for surfactants with packing parameter ($v/a_0 l_c$, where v is the hydrocarbon chain volume, l_c is the critical chain length, and a_0 is the optimal surface area occupied by each head group) greater than 1, the inverted micelle structure is favored[15]. Recently, Wyslouzil et. al.[16] has shown, using small angle neutron scattering, evidence for surface segrega-

tion of organic/water systems. Wilemski et. al.[17], using Monte Carlo methods, mapped out the stability regions of binary water/organic droplets.

1.3 Functionalized Nanoparticles

Nanoparticles are widely used for many applications. Some major applications are biosensors drug delivery vehicles[18-20]. The fabrication of nanoparticles with the desired morphology and structure is challenging and is a major hurdle[20-22]. Gold (Au) is a common material of choice because of its many interesting and unique properties[23] including its resistance to oxidation. Gold nanoparticles (Au-NPs) coated with a self-assembled monolayer (SAM) provides many additional uses in applications including lithography, lubrication, catalysis, biocompatible materials, and biosensors[24]. Characterization of such SAM coated Au-NPs is important. An important aspect of regulatory approval for use in humans will include rigorous physical and chemical characterization of the nanoparticles measuring properties such as the physical size of the particle, the size distribution, particle structure and the composition of chemical or biological coatings[25].

In a recent experimental study[25] the thickness of monolayers functionalized on nanoparticles was characterized using ion-mobility spectrometry. The measurement relied on determination the size of a charged particle through knowledge of the drag force. In that work, functionalized Au-NPs were studied using electrospray-differential mobility analysis (ES-DMA). Commercially available monodisperse Au colloids (10nm, 20nm, 30nm and 60nm) were functionalized with 11-mercaptoundecanoic acid (99+ %, MUA). It was observed that for the MUA coated Au-NPs, the size distribution indeed shifted to larger sizes. The presence of SAM

conjugation on the Au-NPs was thus detected based on the difference in the electrical mobility between conjugated and bare Au-NPs. It was found, for a 30nm Au-NP that the thickness of the coating was ~35% less than that predicted by a rigid core-shell model. The most obvious reason would be that the SAM coating is not really a dense material and as such the surface can be thought of as somewhat porous. This suggests that the functionalized Au-NP would have an inverted micelle structure.

1.4 Organization of the thesis

In light of the above mentioned research efforts aimed towards a better understanding of the properties of organic coated aerosols and functionalized nanoparticles, the objective of the present research has been to study the structure, properties and effects of organic coated aerosols and SAM functionalized nanoparticles. The present work focuses on the Molecular Dynamics study of the structure and properties of organic coated aerosols and functionalized nanoparticles.

Chapter 2 presents an overview of the Molecular Dynamics (MD) method used exclusively for this work. For the work on negative surface tension, a large-scale parallel, using the Message Passing Interface (MPI) communication library, software was written in Fortran 90. The different computational aspects and challenges of the MD method and algorithms are discussed in this chapter.

The most important results are summarized in Chapters 3 to 5, which are arranged in the following way. Chapter 3 is based on Ref. 26, which describes the work done on surface tension of organic aerosols using a coarse-grained model with the help of the software developed. The model problem consists of a pure water droplet coated with fatty acid. For that purpose a pure water droplet was first constructed.

Upon equilibration, the surface water sites were identified and to these surface water sites, the polar head of the fatty acid molecules were attached. Upon equilibration of the coated particle, density and pressure calculations were carried out. It was found that the organic coated water droplet indeed exhibited an inverted micelle structure with the organic coating (on the surface) being under tension. This negative normal pressure led to 'negative' surface tension for the particle. The implication of this negative surface tension, the coated particle can process (absorb/adsorb) water vapor despite its hydrophobic surface, is also discussed in this chapter.

The following chapter (Chapter 4) is based on Ref. 27. In this chapter, an attempt has been made to quantify water processing. A systematic Molecular Dynamics simulation was carried out to compute the rate of water uptake by such coated particles. It was found that the sticking coefficient of water vapor on such coated particles is about a sixth of that on a pure water droplet. This may seem to imply that the condensation rate for the coated particles is reduced. However, one needs to take into account the evaporation of water from such particles as well. As has been shown, the evaporation rate is considerably reduced resulting in a net increase in condensation.

Next, in Chapter 5, the works on surface tension and sticking coefficient were extended to look at the effect of fatty acid chain length, chain branching and oxidation of terminal group on the morphology, internal pressure profile, surface tension and water processing abilities of the organic coated water droplets. It was concluded that, if the interface energy dominates, the particle would have a spherical structure resulting in a negative surface pressure and tension and enhanced water-processing abilities. On the other hand, if the chains were long enough (or branched) such that

the chain-chain interactions are strong, the surfactant molecules would tend to line up parallel to each other and result in the deformation in the underlying water substrate. As such, they will act very much like an oily surface. This manuscript is ready for submission.

Finally, in chapter 6, the MD results on the effect on drag for SAM coating on functionalized nanoparticles is presented. It has been found that the Stokes drag on the functionalized nanoparticles is indeed less than the drag on the corresponding pure particle, consistent with the experimental observation.

2 Molecular Dynamics

2.1 Introduction

All the simulations in this research were carried out using the Molecular Dynamics (MD) method. This chapter gives an overview of the MD method. Section 2.2 gives a very brief general review of Statistical Mechanics followed by an introduction to Molecular Dynamics. The computational challenges of the MD simulation method are described in Section 2.4. And finally, the parallelization algorithm employed in the software developed is discussed in section 2.5.

2.2 A brief review of Statistical Mechanics

Phase space[28, 29, 30]: An important concept in computer simulations is the concept of 'phase space'. For a system consisting of N atoms, $6N$ values are required to define the state of the system (three coordinates per atom and three components of the momentum). Each combination of $3N$ positions and $3N$ momenta (usually denoted by Γ_N) defines a point in the $6N$-dimensional phase space; an ensemble can thus be considered to be a collection of points in the phase space. A single point in phase space describes a state of the system. An ensemble thus is a collection of points in phase space satisfying the conditions of a particle thermodynamic state i.e. it is a collection of all possible systems, which have different microscopic states but have an identical macroscopic or thermodynamic state. A Molecular Dynamics simulation generates a sequence of points in phase space as a function of time, these points belong to the same ensemble and they correspond to the different conformations of the system and their respective momenta.

Ensemble Averages, Time Averages[28, 29, 30]: An experiment is usually made on a macroscopic sample that contains an extremely large number of atoms or molecules sampling an enormous number of conformations. In Statistical Mechanics, averages corresponding to experimental observables are defined in terms of ensemble averages; one justification for this is that there has been good agreement with experiment. An ensemble average is an average taken over a large number of replicas of the system considered simultaneously.

$$\langle A \rangle = \int d\mathbf{p}^N d\mathbf{r}^N A\left(\mathbf{p}^N, \mathbf{r}^N\right) \rho\left(\mathbf{p}^N, \mathbf{r}^N\right) \tag{2.1}$$

where $A\left(\mathbf{p}^N, \mathbf{r}^N\right)$ is the observable of interest and is expressed as a function of the momenta, $\mathbf{p}^N$, and the positions, $\mathbf{r}^N$, of the system. The integration is over all possible values of $\mathbf{r}^N$ and $\mathbf{p}^N$. Here, the angle brackets, $\langle\ \rangle$, represent the ensemble average. $\rho\left(\mathbf{p}^N, \mathbf{r}^N\right)$ is the probability density of the ensemble, i.e. the probability of finding a configuration with a given momentum at a given position. Under the conditions of constant number of particles, volume and energy, the probability density is the well known Boltzmann distribution

$$\rho\left(\mathbf{p}^N, \mathbf{r}^N\right) = \frac{1}{Z} e^{\frac{-E\left(\mathbf{p}^N, \mathbf{r}^N\right)}{k_B T}} \tag{2.2}$$

where $E\left(\mathbf{p}^N, \mathbf{r}^N\right)$ is the energy, T is the temperature, k_B is the Boltzmann's constant and

$$Z = \iint e^{\frac{-E\left(\mathbf{p}^N, \mathbf{r}^N\right)}{k_B T}} d\mathbf{p}^N d\mathbf{r}^N \tag{2.3}$$

is the partition function.

This integral is generally *extremely* difficult to calculate because one must compute all possible states of the system. In an MD simulation, the points in the ensemble are calculated sequentially in time. So, to calculate an ensemble average, the MD simulations must pass through all the possible states corresponding to the particular thermodynamic constraints. Another way, as done in an MD simulation, is to determine a time average of A, which is expressed as

$$\langle A \rangle_{\text{time}} = \lim_{\tau \to \infty} \frac{1}{\tau} \int_{t=0}^{\tau} A(\mathbf{p}_N(t), \mathbf{r}_N(t))\, dt \approx \frac{1}{M} \sum_{t=1}^{M} A(\mathbf{p}_N(t), \mathbf{r}_N(t)) \tag{2.4}$$

where t is the simulation time, M is the number of time steps in the simulation and $A(\mathbf{p}_N(t), \mathbf{r}_N(t))$ is the instantaneous value of A. The dilemma appears to be that one calculates time averages by MD simulations, but the experimental observables are assumed to be ensemble averages. Resolving this leads us to one of the most fundamental axioms of statistical mechanics, the ergodic hypothesis, which states that the time average equals the ensemble average

$$\langle A \rangle = \langle A \rangle_{\text{time}}. \tag{2.5}$$

The basic idea is that if a system is allowed to evolve in time indefinitely, that system will eventually pass through all the possible states. One goal, therefore, of a molecular dynamics simulation is to generate enough representative conformations such that this equality is satisfied. In such a case, experimentally relevant information concerning structural, dynamic and thermodynamic properties may then be calculated using a feasible amount of computer resources. Because the simulations are of fixed duration, one must be certain to sample a sufficient amount of phase space. The first computer simulation of fluids was performed in 1952 by Metropolis, Rosenbluth, Teller and Teller, who developed a scheme for sampling from the Boltzmann distribution to give

ensemble averages. This gave rise to the Monte Carlo simulation method. Not long afterwards, in 1957, Alder and Wainwright recognized that it was, in fact, possible to integrate the equations of motion for a relatively small number of particles (hard spheres) and to mimic the behaviour of a real system using periodic boundary conditions. This led to the first MD simulations of molecular systems.

2.3 Molecular Dynamics

Molecular Dynamics[29, 30] computes the 'real' dynamics of a system, from which time averages of properties can be calculated. Sets of atom positions are derived in sequence by applying Newton's equations of motion. It is a deterministic method, i.e. the state of the system in any future time can be predicted from its current state. The first MD simulations were performed using very simple potentials such as hard-sphere potentials. The particles moved in straight lines at constant velocities between collisions, which were perfect and occurred when the separation between a pair of spheres equaled the sum of their radii. After a collision, the new velocities of the colliding spheres were calculated using the principle of conservation of linear momentum. The hard-sphere models have provided very useful insights but are obviously not ideal for simulating atomic or molecular system. In potentials such as Lennard-Jones potential, the force between two atoms or molecules changes continuously with their separation. The continuous nature of the more realistic potentials requires the equations of motion to be integrated by breaking the calculation into a series of very short time steps (typically between 10^{-15} sec and 10^{-14} sec). At each step, the forces on the atoms are computed and combined with the current positions and velocities generate new positions and velocities a short time ahead. The force acting on each atom is con-

sidered to be constant during that time interval. The atoms are then moved to the new positions, an updated set of forces is computed and so on. In this way MD simulation generates a trajectory that describes how the dynamics variables change with time. MD simulations typically run for hundreds and thousands of picoseconds (the longest simulation run for this research was for 30 nanoseconds). Thermodynamic averages are obtained from MD as time averages using Equation 2.4.

In the MD method, successive configurations of the system are generated by integrating Newton's laws of motion

$$m_i \frac{d^2}{dt^2}\mathbf{r}_i = -\nabla_{\mathbf{r}_i} U\left(\mathbf{r}_1,\mathbf{r}_2,\cdots,\mathbf{r}_N\right) \qquad \forall\ i = 1,2\cdots N \tag{2.6}$$

where N is the total number of sites. The result is a trajectory that specifies how the positions and velocities of the particles in the system vary with time. In more realistic models of intermolecular interactions, the force on each particle changes whenever the particle changes its position, or whenever any of the particles with which it interacts changes position. For more realistic systems, defined by continuous potentials, the motions of all the particles are coupled together, giving rise to a many body problem that cannot be solved analytically. Under such circumstances, the equations of motion are integrated using the finite difference method. Clearly, no integration algorithm will provide an essentially exact solution for a long time. Fortunately we do not need to do this. In essence, Molecular Dynamics served two roles. Firstly, we need essentially exact solutions of equations of motion for times comparable with the correlation times of interest so that we can accurately compute time correlation functions. Secondly, we use the method to generate states sampled from the initial configuration. We do not need exact classical trajectories to do this must lay great em-

phasis on energy conservation as being of primary importance. Momentum conservation is also important by can be easily arranged. For an isolated system, particle trajectories must stay on the appropriate constant energy hypersurface in the phase space; otherwise correct ensemble averages will not be generated. Energy conservation is degraded as the time step is increased and so all simulations involve a trade-off between economy and accuracy. A good algorithm permits a large time step while preserving acceptable energy conservation. The original Verlet algorithm [1967] is

$$r(t+\Delta t) = r(t) - r(t-\Delta t) + \frac{f(t)}{m}(\Delta t)^2. \tag{2.7}$$

This algorithm does not use velocity to compute new positions. Velocity is computed as

$$v(t) = \frac{r(t+\Delta t) - r(t-\Delta t)}{2\Delta t}. \tag{2.8}$$

The global error associated with the Verlet algorithm is third order for position and second order for velocity. This method is also known as the "explicit central difference method". This "original Verlet" is not self-starting. Another problem is the velocity is computed from the difference of two quantities of the same order of magnitude. Such operations result in a substantial round-off error.

A mathematically equivalent version, and also the most commonly used integrator (as used in this work), of the "original Verlet" is the velocity form of Verlet algorithm:

$$r(t+\Delta t) = r(t) + v(t)\Delta t + \frac{f(t)}{2m}(\Delta t)^2, \tag{2.9}$$

$$v(t+\Delta t) = v(t) + \frac{f(t+\Delta t) + f(t)}{2m}. \tag{2.10}$$

With this algorithm, we can compute the new velocities only after we've computed the new positions and from those, the new forces. Storage required for this method is 6*N*. The advantages of this algorithm are

- self-starting
- time reversible
- symplectic[31] (preserves volume in phase space).

2.4 Force field and Some Computational Issues

Force field is the core of MD and determines the behavior of the system. The force field constitutes a set of potential functions that sum up to the potential energy of the system. The potential energy describing a particular model can be written as $V = V_{\text{bond}} + V_{\text{angle}} + V_{\text{dihedral}} + V_{\text{improper}} + V_{\text{LJ}} + V_{\text{coulomb}}$. The bond potential V_{bond}, the angle potential V_{angle} and the dihedral potential V_{dihedral} are described within a single molecule for atoms that are separated by at most three covalent bonds. The improper dihedral potentials are applied to keep a planar group planar. The non-bonded potentials V_{LJ} and V_{coulomb} describe the interactions between all pairs of atoms/sites in the system. The Lennard-Jones potential describes the attractive dispersion forces (r^{-6}) along with an effective implementation of the hard-core repulsion (r^{-12}) at short distances. The Coulombic interaction, V_{coulomb}, is of course the Coulomb interaction between all charged atom pairs. For this work, the coarse-grained force-field models developed by Shelley et. al.[32] has been used for the work on surface tension (as described in Chapter 3). For the subsequent work with atomistic/united atom setups, the force-field from the GROMACS[33] software package was used.

2.4.1 Computing Potential – Non-bonded cutoff

The most time consuming part of a Molecular Dynamics simulation is the calculation of the non-bonded energies and the corresponding forces[29, 30]. The numbers of bond-stretching, bending or torsional terms in a force field model are all proportional to the number of atoms but the number of non-bonded terms that need to be evaluated increases as the square of the number of atoms (for a pairwise model) and is thus of the order of N^2. In principle, the non-bonded interactions are calculated between every pair of atoms in the system. However the Lennard-Jones 12-6 potential falls off rapidly with distance; at 2.5σ the value of the potential is just 1% of the well depth. This reflects the r^{-6} distance dependence of the dispersion interaction. The most popular way to deal with the non-bonded interactions is to use a non-bonded cutoff. When a cutoff is employed, the interactions between all pairs of atoms that are further apart than the cutoff value are set to zero. A cutoff introduces a discontinuity in both the potential energy and the force near the cutoff value. This creates problems since in molecular dynamics simulations where energy conservation is required. One approach is to use a switching function with which the new potential becomes:

$$\begin{aligned} U(r) &= V_{LJ}(r) && r \le r_c \\ &= V_{LJ}(r) * H(r) && r_c \le r \le r_u \\ &= 0 && r > r_u \end{aligned} \qquad \text{where} \qquad H(r) = \frac{1}{2} + \frac{1}{2}\cos\left(\pi \frac{r - r_c}{r_u - r_c}\right).$$

Figure 2.1 is a plot of the original and modified Lennard-Jones 12-6 potential.

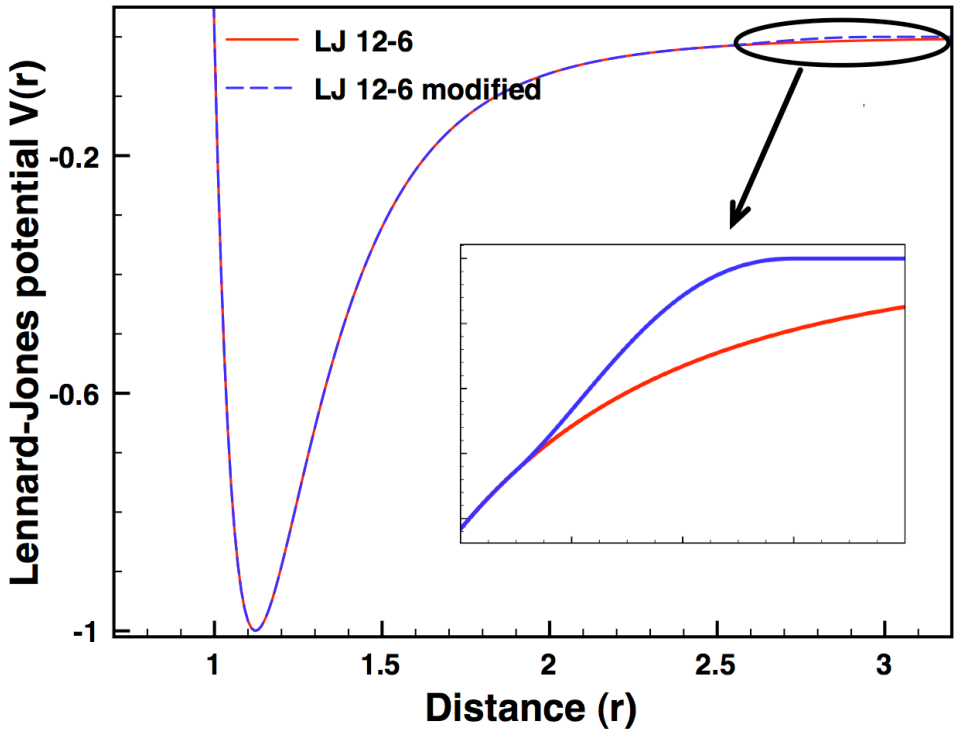

Figure 2.1: Lennard-Jones potential modified using a switching function

2.4.2 Computing Potential – Non-bonded Neighbor List

By itself, the use of a cutoff may not dramatically reduce the time taken to compute the number of non-bonded interactions because we'd still have to calculate the distance between every pair of atoms on the system simply to decide whether they are close enough to calculate their interaction energy[29, 30]. Calculating all the $N(N-1)$ distances takes almost as much time as calculating the energy itself. In simulation of fluids, an atom's neighbors (i.e. those atoms that are within the cutoff distance) do not change significantly over 10 or 20 molecular dynamics time steps. If we 'knew' which atoms to include in the non-bonded calculations, then it would be possible to identify directly each atom's neighbors without having to calculate the distances to all the other atoms in the system. The non-bonded neighbor list (first proposed by Verlet)

is just such a device. The Verlet neighbor list [Verlet 1967] stores all atoms within the cutoff distance, together with all the atoms that are slightly further away than the cut-off distance. This is most efficiently done using a large neighbor list array, L, and a pointer array, P. The pointer array indicates where in the neighbor list the first neighbor for that atom is located. The last neighbor of atom i is stored in the element $P[i+1]-1$ of the neighbor list as shown in Figure 2.2.

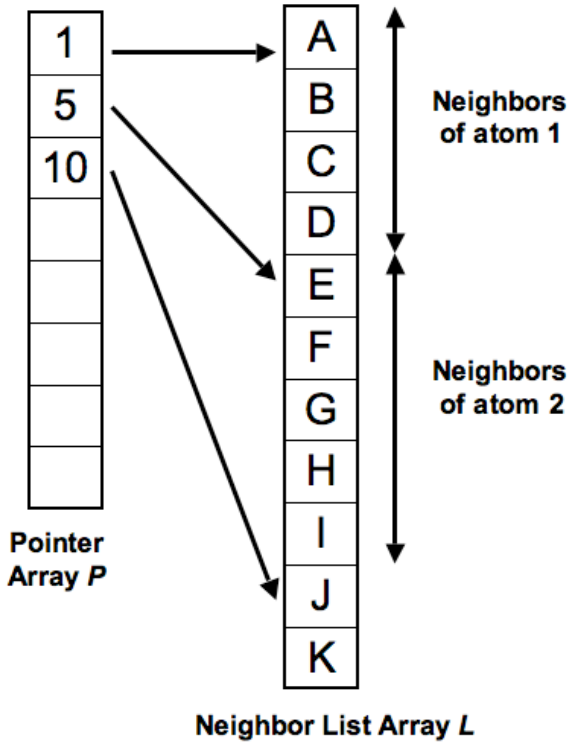

Figure 2.2: Schematic of Neighbor and Pointer Arrays (taken from Ref. 29)

Thus the neighbors of atom i are stored in elements $L[P(i)]$ through $L[P(i+1)-1]$ of the array L. The neighbor list is updated at regular intervals throughout the simulation. Between updates, the neighbor and pointer lists are used to directly identify the nearest neighbors of each atoms i. The distance used to calculate each atom's neigh-

bors should be larger than the actual non-bonded cutoff distance so that no atom, initially outside the neighbor cutoff, gets closer than the non-bonded cutoff distance before the neighbor list is updated again. It is important to update the neighbor list at the correct frequency. If the update frequency is too high the procedure is inefficient; too low and the energies and forces may be calculated incorrectly due to atoms moving within the non-bonded cutoff region. An update frequency between 10 and 20 steps is common.

2.4.3 Conservation of Momentum

Under the influence of a conservative force field, the linear and angular momenta are conserved. However, due to round-off errors, the momenta don't stay conserved over long periods of time. So we need to reset it to its initial value (zero) for more accurate computation of physical properties. The total linear and angular momenta of the system are removed by removing the linear and angular components of velocity[34]

$$\mathbf{v}_i^{new} = \mathbf{v}_i^{old} - \sum_j \frac{\mathbf{v}_j^{old}}{N} - \omega \times \mathbf{r}_i \qquad \forall\ i = 1:N, \tag{2.11}$$

where $\omega = \mathbf{I}^{-1}\mathbf{L}$, with $\mathbf{I}$ = Moment of Inertia tensor and $\mathbf{L}$ = Angular Momentum.

2.5 Parallelization: Spatial Decomposition Algorithm

There is a natural parallelism in MD in that the force calculations and position/velocity updates can be done simultaneously for all atoms. Almost all the algorithms proposed are variations of two basic methods. In the first class of methods, a pre-determined set of force computations is assigned to each processor. The assignment remains fixed for the duration of the simulation. The simplest way of doing this

is to give a subgroup of atoms to each processor. This method is called an atom decomposition (AD) method. The processor computes forces on its atoms no matter where they move in the simulation domain. The cost of communication is $O(N)$. By contrast, in the second class of methods, called the spatial decomposition (SD) methods, each processor is assigned a portion if the physical simulation domain. Each processor computes only the forces on atoms in its sub-domain. As the simulation progresses, processors exchange atoms as they move from one sub-domain to another. Communication cost is $O(N/P)$.

The more efficient parallel MD algorithm is the SD algorithm[35] and has been employed in our software. In this case, the physical domain is divided into small 3D simulation boxes, one for each processor (spatial decomposition of the workload). Each processor then computes forces on and updates the positions and velocities of all atoms within its domain at each time step. As atoms near the boundary of each simulation box move around, they are reassigned to new processors if they move through the physical domain. In order to compute forces on its atoms, a given processor needs to know the positions of atoms only in the nearby boxes. The communication therefore 'local' in nature for the SD method as opposed to global in the AD case. Each processor in our SD algorithm would require the atom positions from the nearby processors, the shaded region in Figure 2.3, to compute the force on each atom it owns.

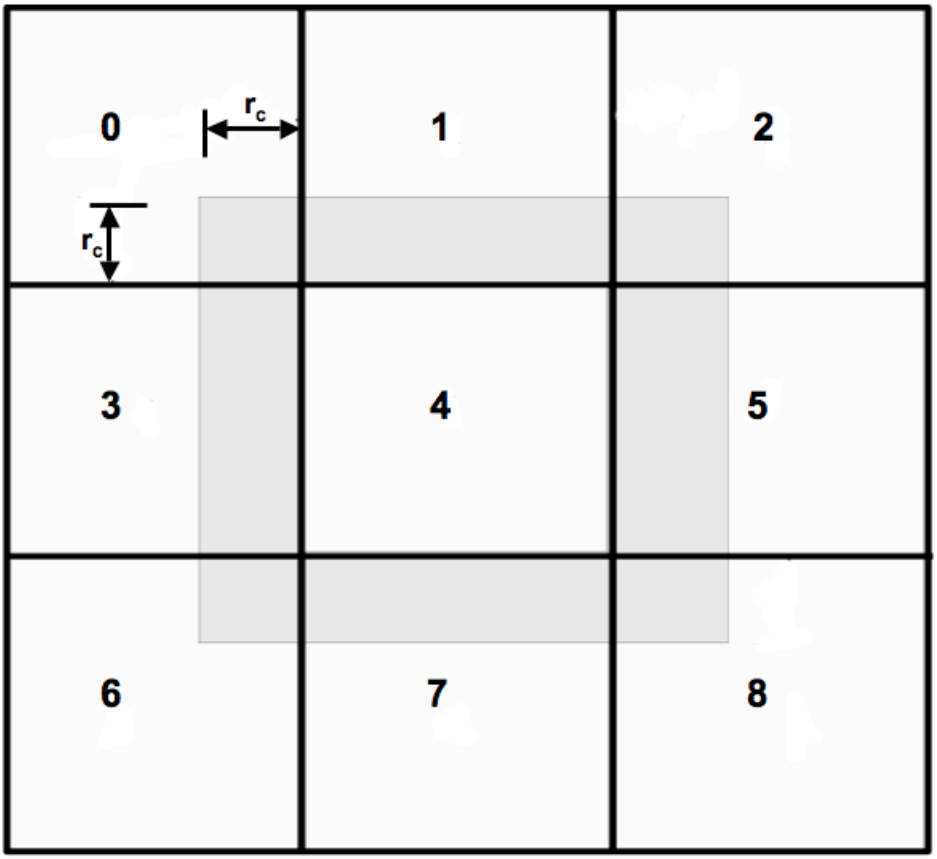

Figure 2.3: A cross-sectional view of the domain decomposition

Here, r_c is the cutoff distance for the neighbor list. For efficient communication to be efficient, two data arrays were used in each processor, one for the physically present ~N/P atoms in the simulation box belonging to the processor under consideration and one for atoms in nearby boxes. The communication scheme used to acquire the information from neighboring processors owning the nearby boxes, is shown is Figure 2.4.

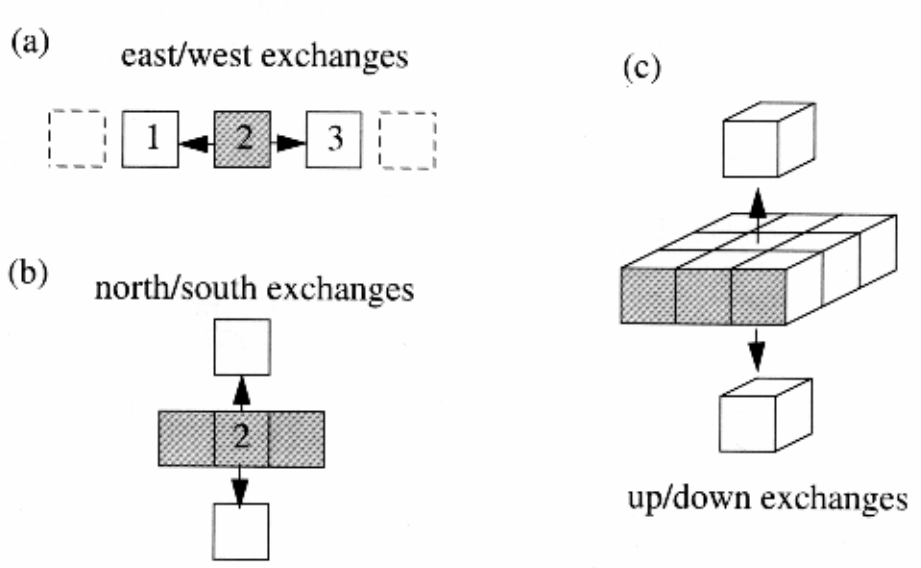

Figure 2.4: SD Algorithm Communication (Taken from Ref. 35).

The first step is for each processor to exchange information in the East/West direction. Processor 2 fills a message buffer with atom values it owns that are within the neighbor list cut off length r_c of processor 1's box. (To avoid extra communication, we make sure that $d_{ew} > r_c$, where d_{ew} is the length of the box in the east/west direction). Then each processor sends its message to the processor in the westward direction and receives a message from the eastward direction. Each processor puts the received information into its second data structure. Now the process is reversed with each processor sending to the east and receiving from the west. The same procedure is now repeated in the north/south direction, the difference being that the messages sent to the adjacent processor not only contains the atoms the processor owns (in its first data structure), but also the atoms in the second data structure that are needed by the adjacent processor. Finally the process is repeated in the up/down direction. Now atom positions from an entire plane of boxes (i.e. from 9 boxes) are being sent in each message. The main advantage of this algorithm is that the required atom values from

all 26 surrounding boxes are obtained in just six data exchanges. Moreover if the parallel machine is a cube, the processors can be mapped to the boxes in such a way that all six of these processors can be directly connected to the centre processor making the message passing very fast.

3 'Effective' Negative Surface Tension: A Property of Coated NanoAerosols Relevant to the Atmosphere

3.1 Introduction

This chapter describes the results of a Molecular Dynamics study on the unique properties of organic coated water droplets. In particular it has been found that for particles preferring an inverted micelle structure, the lower chain-chain interaction, with increasing radial distance from the water-organic interface, results in a negative internal radial pressure profile for the organic layer. As a result, a coated particle behaves as though the surface tension is 'negative' which implies that such a particle will inherently have an inverse Kelvin vapor pressure effect, resulting in increased water condensation.

As mentioned in Chapter 1, a conceptual model for organic aerosols has been suggested[14, 36] for the composition, structure and atmospheric processing of organic aerosols. The organic materials that coat the marine aerosol particles are surfactants of biological origin. It is believed the organic aerosol prefers an 'inverted micelle' structure consisting of an aqueous core encapsulated in an inert, hydrophobic organic monolayer. The surfactants lie with their polar heads inserted into the ionic aqueous core, with their hydrophobic hydrocarbon tails exposed to the atmosphere. Indeed, for surfactants with packing parameter ($v/a_0 l_c$, where v is hydrocarbon chain volume, l_c is the critical chain length and a_0 is the optimal surface area occupied by each head group), greater than 1, the inverted micelle structure is favored[15]. For such inverted micelle structures, with negative curvature modulus, the surface energy has an extra

term $\frac{1}{2}k_b R^2$, where k_b is the curvature modulus and R is the radius of the particle, making the surface energy negative[37]. Recently Wyslouzil et al.[16] have shown, using small angle neutron scattering, evidence for surface segregation of organic/water systems, and Wilemski[17] using Monte Carlo methods mapped out the stability regions of binary water/organic droplets.

Understanding the structure and properties of these coated aerosols is important as they may significantly affect the processing of water vapor in the atmosphere, cloud formation, and the radiation balance of the earth.

It is well known that the presence of surfactants on a planar water surface reduces the surface tension[36, 37]. In this chapter, we report the results of molecular dynamics (MD) calculations of the pressure profile, and the corresponding surface tension of the coated particles. The results indicate that the organic coating on a curved surface of such a droplet is under negative pressure. Using a simple ball-stick geometric model, we illustrate that this negative pressure is a manifestation of the curved surface. As a result, the particle seems to behave in a manner consistent with a 'negative surface tension'. We explain the physical significance of this result in the context of water vapor processing.

3.2 Computational Model

The structure of these particles are computed using a 'coarse graining' potential approach to simplify the representation of water and the organic coating. The coarse-grained methods have their shortcomings but their utility for surfactant systems have been demonstrated[32]. For surfactant systems, it has been suggested that coarse-

grained models can be made sufficiently accurate to mimic specific surfactants. For the inverted micelle model, we follow the coarse-grained model developed by Shelley et al.[32, 38, 39]. This model mimics the key physical or structural features known from experiment of atomistic simulations. The non-bonded interactions were modelled using the Lennard-Jones *m*-*n* potential, which has the form

$$V(r) = k\,\varepsilon\left[\left(\frac{\sigma}{r}\right)^{m} - \left(\frac{\sigma}{r}\right)^{n}\right]. \tag{3.1}$$

Here r is the distance between two different sites, ε is the potential well-depth and σ is the distance at which this potential is zero.

For water, a spherically symmetric site – referred to as a 'W'-site – was chosen to represent a "loose grouping of three water molecules". Interactions between W sites were described using a Lennard-Jones 6-4 potential. This potential function has a relatively wide potential minimum, permitting liquid-vapour existence for a wide range of temperatures. ε_{WW} was chosen such that the melting temperature of a slab of W sites arranged on an fcc lattice is 212.1K. σ_{WW} was chosen so as to produce the density of 1g/cc at 303.15K.

A fatty acid molecule (decanoic acid or capric acid) is shown in Figure (3.1).

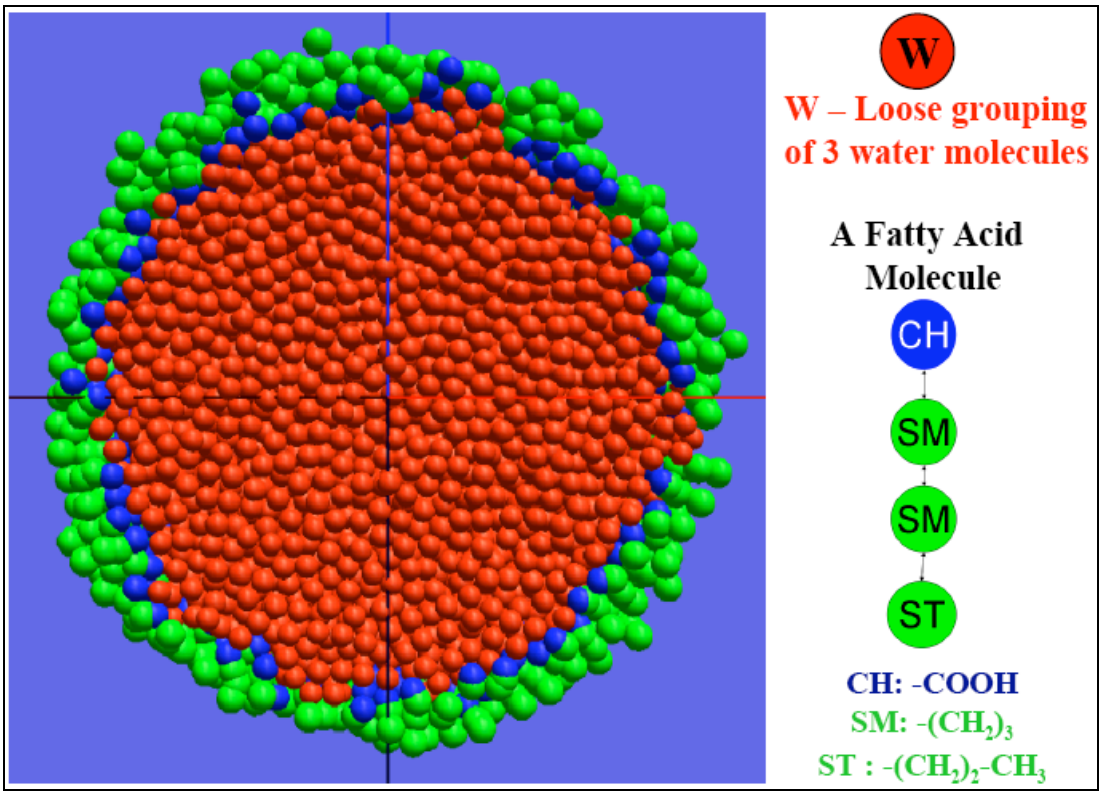

Figure 3.1: Coated particle (x-sectional view) of radius ~6.5 nm and (right) a single fatty acid molecule.

Harmonic bond length potentials of the form

$$V(r) = \frac{k_r}{2}(r - r_0)^2 \tag{3.2}$$

were used to link together the adjacent beads in a fatty acid molecule.

Bond angle potentials are needed to maintain proper chain stiffness and overall length and for this we used a cosine angle potential

$$V(\theta) = k_\theta[1 - \cos(\pi - \theta)]. \tag{3.3}$$

Non-bonded interactions between two beads from different fatty acid molecules were modeled by the Lennard-Jones 9-6 potential. The potential parameters are listed in Tables 3.1, 3.2 and 3.3.

Table 3.1: Non-bonded interaction potential parameters.

Site	Type	$\sigma\left(\text{Å}\right)$	$\frac{\varepsilon}{k_B}(K)$
W-W[1]	LJ 6-4	4.58	212.10
W-CH[2]	LJ 6-4	4.58	212.10
CH-CH[3]	LJ 12-6	4.22	110.7
W-SM[1]	LJ 9-6	4.49	130.57
CH-SM[2]	LJ 9-6	4.49	130.57
W-ST[1]	LJ 9-6	4.49	200.00
CH-ST[2]	LJ 9-6	4.49	200.00
SM-SM[1]	LJ 9-6	4.40	123.00
SM-ST[1]	LJ 9-6	4.40	188.40
ST-ST[1]	LJ 9-6	4.40	288.06

Table 3.2: Harmonic bonded interaction potential parameters.

Bond	$r_0\left(\text{Å}\right)$	$\frac{k_r}{k_B}(K)$
SM-SM[1]	3.67	6600
SM-ST[1]	4.53	6600

[1] Values obtained from Ref. 39
[2] Assumed W-CH = W-W; CH-SM = W-SM; CH-ST = W-ST
[3] Value obtained from Ref. 46

CH-SM[4]	3.67	6600

Table 3.3: Angle bending potential parameters.

Angle	θ_0(rad)	$\frac{k_\theta}{k_B}(K)$
CH-SM-SM[5]	π	1150
SM-SM-ST	π	1150

3.3 Simulation Procedure

The simulations were run on either a Linux cluster or on an IBM SP3 running up to 8 processors. The trajectories of all the atoms were determined by integrating the equations of motion[29] using the velocity form of Verlet algorithm. A time step of 2 fs was typically used to ensure energy conservation, and the Verlet neighbor list with parallel architecture[35] was employed in all the simulations. The simulations were conducted in a spherical cavity with "spherical boundary conditions"[42]. An external repulsive potential emitted from the wall of the cavity served to prevent molecules from the simulation domain. The radius of the cavity was taken to be 27.5nm (for particles of sizes 5-7nm) so as not to influence the particle properties. All simulations

[4] Assume CH-SM = SM-SM
[5] Assume CH-SM-SM = SM-SM-ST

were carried out in a constant energy environment. During the equilibration process, velocity rescaling was employed to control the temperature.

The first step in the equilibration procedure was to prepare an equilibrated pure water particle consisting of 8192 W sites at 254 K. An initial simple cubic configuration was taken and velocity was generated corresponding to a temperature of 100K. The temperature was then slowly raised till the structure melted. The radial distribution function at 254K confirmed a liquid state. At a higher temperature (about 275K), the droplet started evaporating. Unless otherwise noted, all simulations took place at the constant temperature of 254K.

The next step was to coat the spherical water droplet with fatty acid molecules. A fatty acid molecule was placed on each surface W site (CH site attaching to the surface W, and the rest of the surfactant molecule radially outwards). The coated particle was then equilibrated at 254K. For the last step in the preparation process, the simulation was switched to a constant energy calculation. If the average temperature of the particle deviated by more than 10K, the equilibration process was repeated till the particle temperature deviated by less than 10K. The fatty acid molecules did not leave the surface of the equilibrated particle at the simulation temperature, and the droplet was stable throughout the process of equilibration, and later when we computed the normal pressure. Figure (3.1) shows a cross-sectional view of the equilibrated coated particle. It has a core-shell structure as has been predicted for model aqueous organic droplets using density functional theory[17], and consistent with the experimental work of Wyslouzil et al.[16].

3.4 Density, Pressure and Surface Tension Calculations

3.4.1 Density and Pressure

Both density and pressure profiles were computed as a function of r[42], the distance from the centre of mass. To compute density, sub-spherical shells were introduced at a distance of $\delta r = 0.02\sigma_{W-W}$ from each other where $f(r_{ij})$ is the potential parameter for W-W interaction. For density calculations, we considered a spherical shell of thickness δr at a distance *r* from the centre of mass. Then the density at distance *r* was calculated as the ratio of the sum of the masses of all the sites in that shell and the volume of the shell. The density profile of the coated particles is as in Figure 3.2.

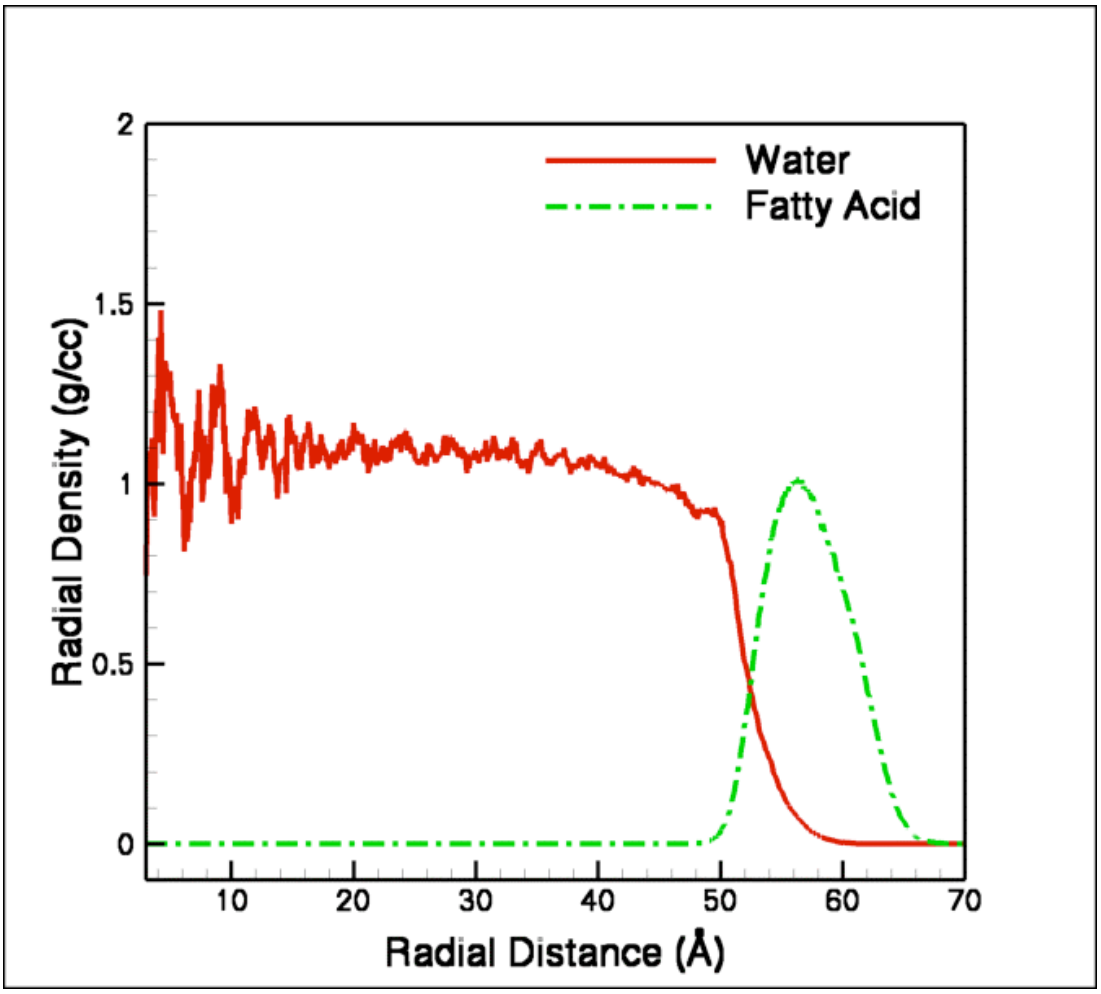

Figure 3.2: Density profile of the coated particle.

On grounds of symmetry, the pressure tensor can be written as[42, 43]

$$\mathbf{p}(\mathbf{r}) = p_N(r)[\mathbf{e_r}\mathbf{e_r}] + p_T(r)[\mathbf{e}_\theta\mathbf{e}_\theta + \mathbf{e}_\varphi\mathbf{e}_\varphi] \tag{3.4}$$

where $\mathbf{e_r}$, $\mathbf{e}_\theta$, $\mathbf{e}_\varphi$ are orthogonal unit vectors and r is the distance from the centre. The normal component of the Irving-Kirkwood pressure, $p_N(r)$, is given by $p_N(r) = p_K(r) + p_U(r)$, where $p_K(r)$ and $p_U(r)$ are the kinetic and configurational terms, respectively, and are given by

$$p_K(r) = k_B T \rho(r)$$
$$p_U(r) = S^{-1} \sum_k f_k \tag{3.5}$$

where k_B is the Boltzmann constant, T is the particle temperature, S is the area of the spherical surface of radius r and f_k is the normal component of the force between two sites acting across the surface S. For a single surface S, the relevant geometry is given in Figure 3.3.

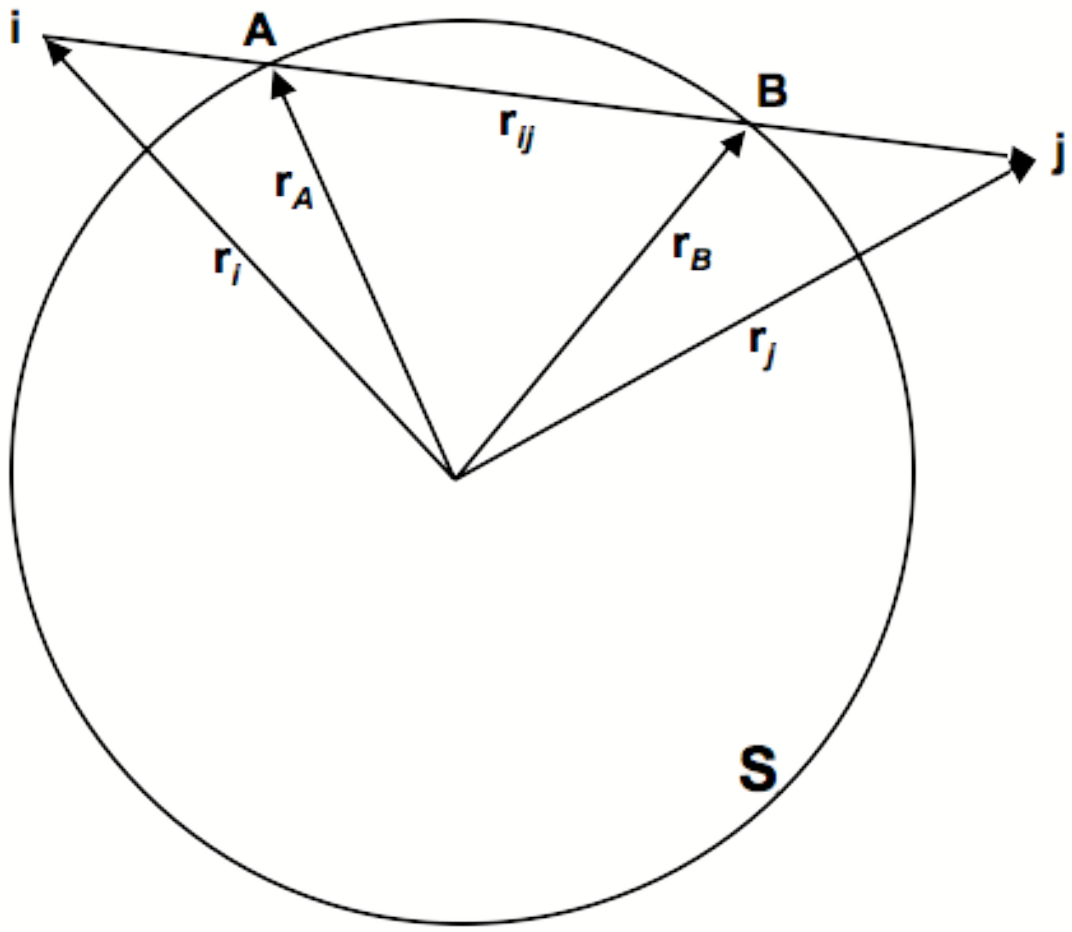

Figure 3.3: Pressure Computation Geometry (taken from Ref. 42)

The force vector, of magnitude $f(r_{ij})$ acts along $\mathbf{r}_{ij} = \mathbf{r}_j - \mathbf{r}_i$ and intersects *S* at two points (depending on the location of *i* and *j* there may be one intersection point or none at all). These points are *A* and *B* with corresponding radius vectors $\mathbf{r}_A$ and $\mathbf{r}_B$. We examine one of these points and call the relevant vector **r**. The force vector $\mathbf{f}(\mathbf{r}_{ij})$ is given by $\mathbf{f}(\mathbf{r}_{ij}) = \hat{\mathbf{r}}_{ij} f(r_{ij}) = -\hat{\mathbf{r}}_{ij} \frac{dV(r_{ij})}{dr_{ij}}$. So, the relevant f_k term is

$$f_k = \left|\hat{\mathbf{r}} \bullet \hat{\mathbf{r}}_{ij}\right| f(r_{ij}) = \left|\mathbf{r} \bullet \mathbf{r}_{ij}\right| \frac{f(r_{ij})}{r r_{ij}}.$$

Therefore, $p_U(r) = -(4\pi r^3)^{-1} \sum_k \left|\mathbf{r} \bullet \mathbf{r}_{ij}\right| \frac{1}{r_{ij}} \frac{dV(r_{ij})}{dr_{ij}}$.

More details for computing $\left|\mathbf{r} \bullet \mathbf{r}_{ij}\right|$ can be found in Ref. 42.

The radial pressure profiles of the bare and coated particles are given in Figure 3.4.

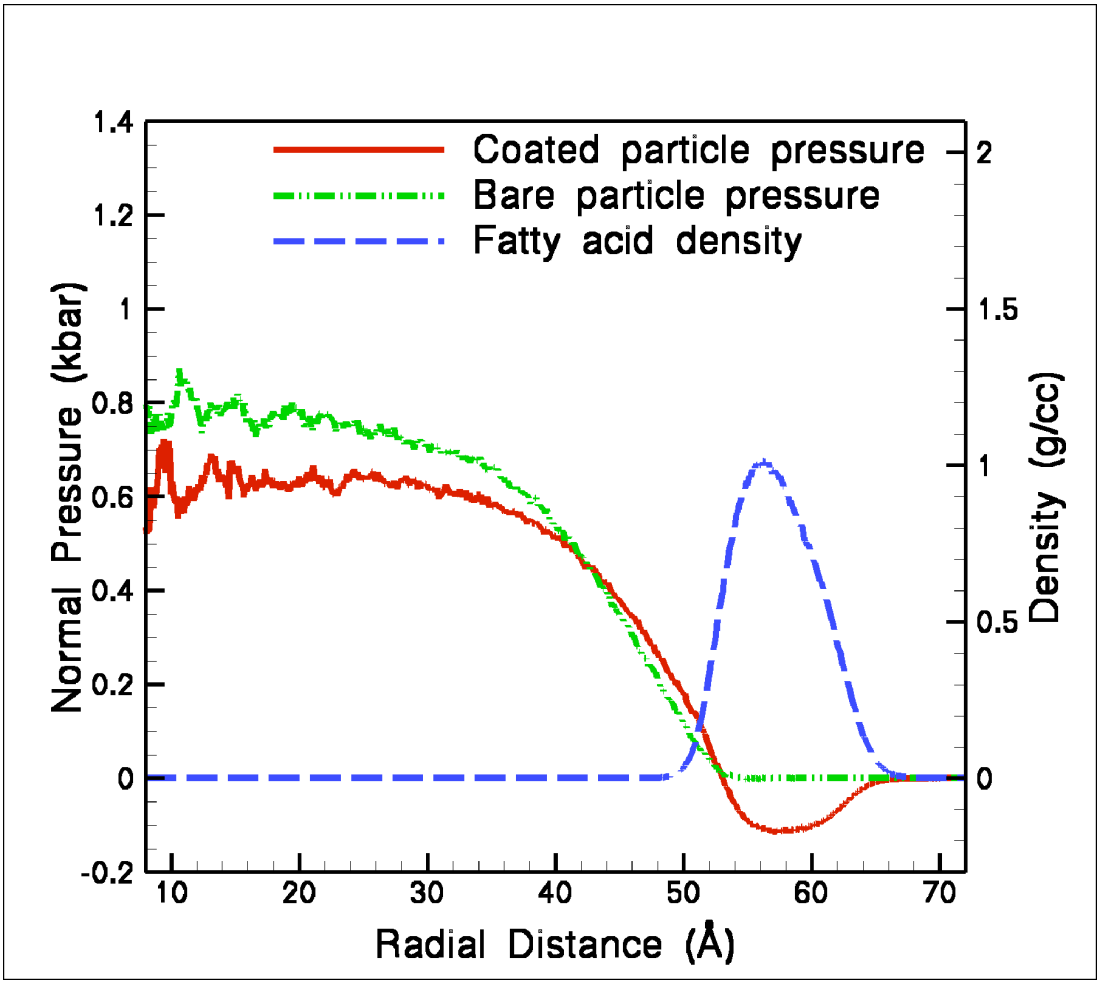

Figure 3.4: Radial pressure profiles of bare and coated particles

We used the same spherical shells as above to compute $p_N(r)$. The radial density and normal pressure were averaged over 500 snapshots collected over 100ps. The important point is that for the coated particle, the coating was found to be under negative pressure i.e. tension (compare the pressure profiles in Figure 3.4 with the fatty acid density). The implication of this to surface properties is discussed later.

3.4.2 Surface Tension

The surface and interfacial tensions were computed following Widom et al[43]. We consider a drop of phase α immersed in phase β, which in turn is immersed in phase γ [Figure 3.5].

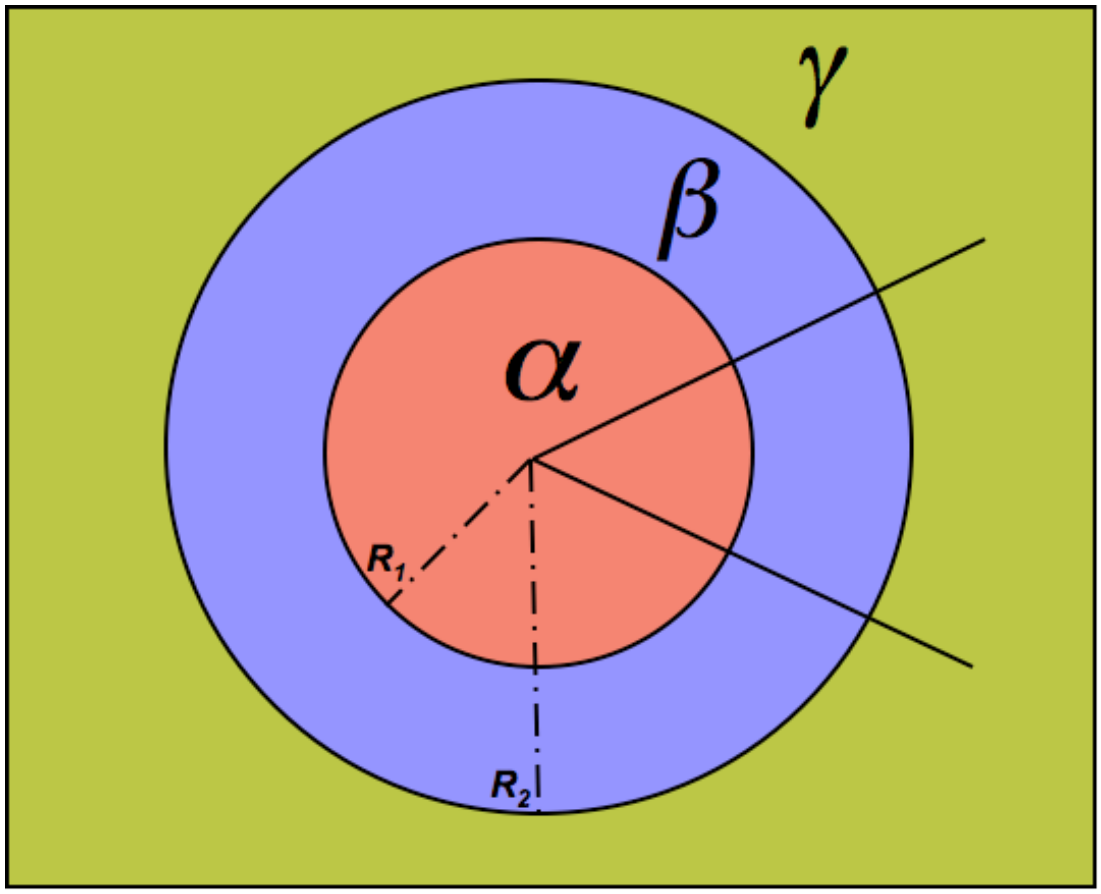

Figure 3.5: Schematic for surface tension calculation

The system is described by polar coordinates r, θ, ϕ. The system under discussion is bounded by two concentric spheres, of radii R^{α} (which lies in phase α) and R^{γ} (in phase γ) (and the sphere of radius R^{β} lies in phase β). Two arbitrary surfaces of radii R_1 and R_2 separate the three phases.

Following the arguments in Ref. 43, for the phase α to be in equilibrium with phase β, we get $\gamma_i = \int_{R^\alpha}^{R^\beta} \left(\frac{r}{R_1}\right)^2 dr \left[p_N(r) - p_T(r)\right]$.

The general condition of mechanical equilibrium is $\nabla \cdot \mathbf{p} = \mathbf{0}$. Evaluating we get,

$$\begin{bmatrix} \frac{\partial p_N}{\partial r} + 2\frac{p_N}{r} - 2\frac{p_T}{r} \\ \frac{1}{r}\frac{\partial p_T}{\partial \theta} \\ \frac{1}{r\sin\theta}\frac{\partial p_T}{\partial \varphi} \end{bmatrix} = 0.$$

The last two equations simply imply that the tangential component of the pressure tensor, p_T is independent of θ and φ. The first equation leads to a relation between the normal and the tangential components $p_T(r) = p_N(r) + \frac{r}{2}\frac{dp_N(r)}{dr}$. So, finally we get,

$$\gamma_i = \int_{R^\alpha}^{R^\beta} \left(\frac{r}{R_1}\right)^2 dr \left[-\frac{r}{2}\frac{d}{dr} p_N(r)\right] \tag{3.6}$$

The Laplace-Young equation gives $\gamma_i = \frac{1}{2} R_1 \left(p_\alpha - p_\beta\right)$, which leads to

$$\gamma_i^{\,3} = -\frac{1}{8}\left(p_\alpha - p_\beta\right)^2 \int_{R^\alpha}^{R^\beta} r^3 \frac{dp_N(r)}{dr} dr, \tag{3.7}$$

where p_α is the bulk pressure in phase α etc. Similarly, for phases β and γ to be in mechanical equilibrium with each other, we arrive at a relation similar to Equation (3.7) with appropriate integration limits.

Equation (3.7) gives the mechanical route for the calculation of surface tension. As has been pointed out[42], neither the thermodynamical approach nor the mechanical approach is without limitations. However, it has been shown by Thompson et. al.[42]

that the values of the surface tension computed via both these routes have the same trends and differ by less that 10%. So the current value of the surface tension can be taken as a good approximation to the thermodynamic surface tension.

3.5 Discussion

3.5.1 Pressure

The radial pressure profile of the coated particle, presented in Figure 3.4, shows that the interior of the particle is under compression as expected from the Laplace-Young equation. However the pressure profiles for the bare and the coated particles are noticeably different in that the coated particle has a significant negative pressure for the coating.

We probed the physical manifestation of this with a simple model. We consider a sphere of radius R (a droplet of water). We assume that the fatty acid molecules have one polar head (A_i) and two hydrocarbon beads (B_i and C_i). The length of each such molecule is $4L$ [Figure 3.6].

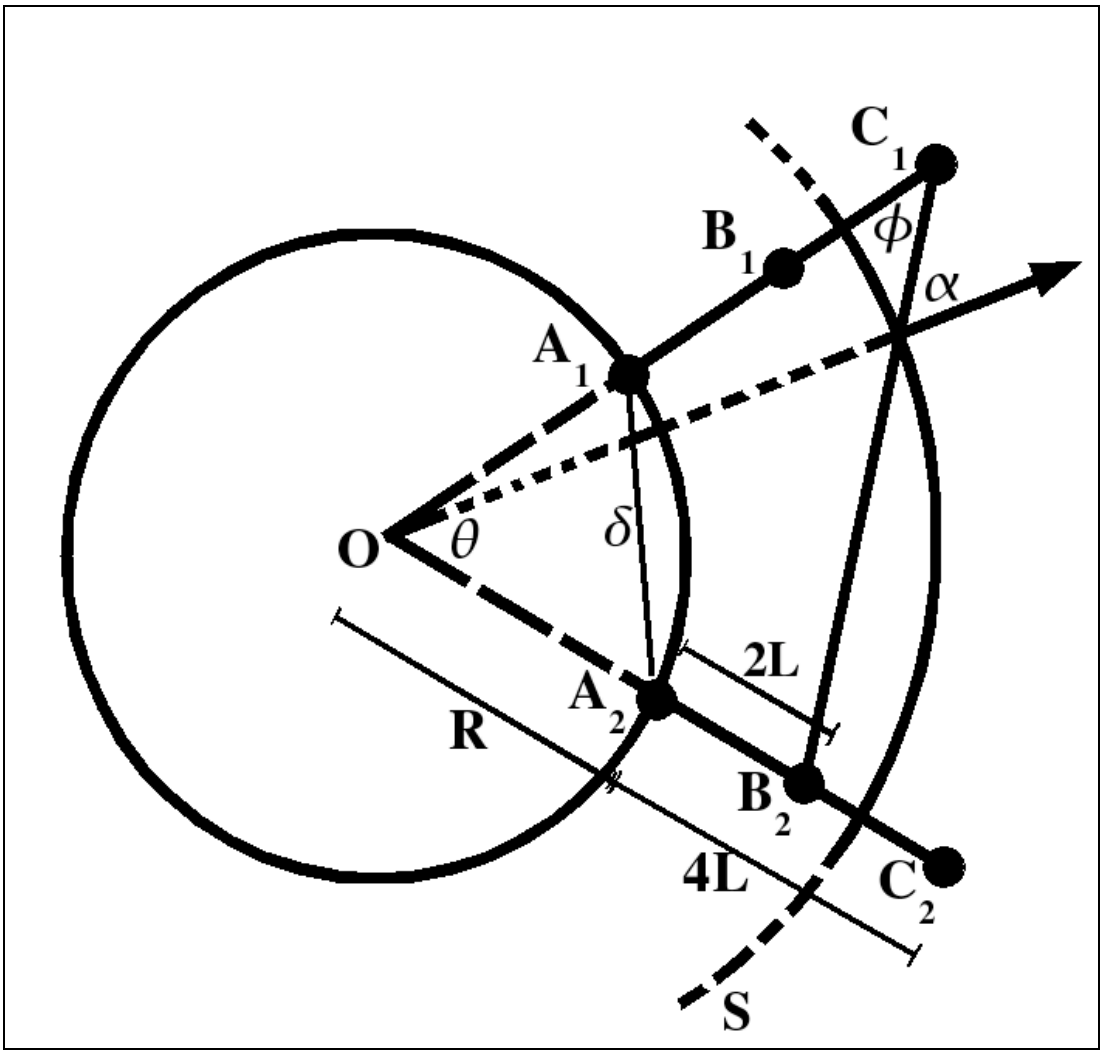

Figure 3.6: A simple model to illustrate the existence of negative pressure.

These molecules are considered to be rigid with the polar head binding to the water surface and the hydrocarbon beads radially outwards. We further assume that these molecules are distributed evenly on the water surface so that the distance between any two A_i's is always δ. The only force acting between sites is that between the beads B_i and C_j with $i \neq j$ and the force is between the nearest neighbors only. Let F_N be the normal component of the force across the surface S, which is of radius R+3L. Then,

$F_N = F_d \cos\alpha$, where F_d is the magnitude of the force acting between B_i and C_j. We want to compute the pressure across the surface S.

Next consider three adjacent fatty acid molecules on the surface of the sphere. We have an equilateral triangle with the vertices on the surface of the sphere. The area of this triangle is $A_T = \frac{\sqrt{3}}{4}\delta^2$. Total surface area of the sphere is $4\pi R^2$. So the number of such triangles is $N_T = \frac{4\pi R^2}{A_T} = \frac{16\pi R^2}{\sqrt{3}\delta^2}$. ($\delta$ being small compared to R, we can ignore the contribution from the spherical excess). The number of A_i's on the surface of the sphere $\approx N_T$ and the number of nearest neighbors of each fatty acid molecule is 6, such that the normal component of the pressure across S is

$$p_N(r = R + 3L) = \frac{6F_N \cdot N_T}{4\pi(R + 3L)^2}. \tag{3.8}$$

Taking $\delta = \frac{\sigma_0}{\sqrt{2}}$ (so that for large R, the force between B_i and C_j is zero) and keeping L fixed at $\frac{\delta}{2}$, we vary R from 10* δ to 1000* δ with an increment of 10* δ. From Figure 3.7, we see that the normal pressure is in fact negative initially and approaches zero for large R (i.e. a flat surface). In other words the effect is less pronounced for large particles and/or for smaller chains.

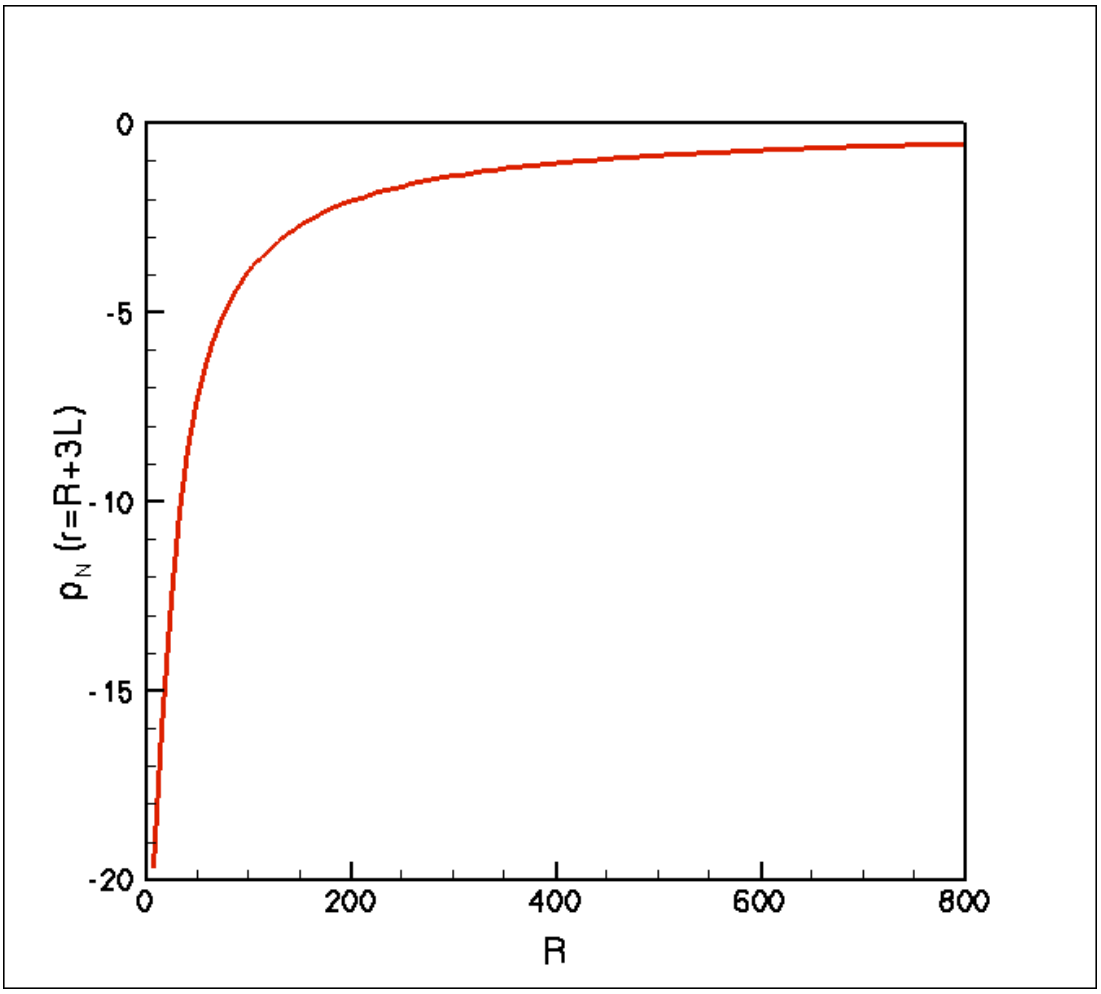

Figure 3.7: Normal pressure Vs the radius of the droplet

This result indicates that the radial pressure profile for a core-shell inverted micelle like structure, where the coating molecules are tethered to the core will result in, by simple geometric considerations, a decrease in density with increasing distance from the core. This decreasing density should always result in a coating under tension.

3.5.2 Surface Tension

From the MD computed pressure profiles we obtain, (using Equation 3.7 with $p_\alpha = 0.77$ kbar, $p_\beta = 0$ kbar and integrating from $r = 16$ Å to $r = 60$ Å) a surface tension of 166 mJ/m^2 for the bare particle.

For the coated particle, with $p_\beta = p_2 = -0.11667$ kbar, $p_\gamma = p_3 = 0$ kbar and integrating from $r = 57$ Å to $r = 70$ Å we get the surface tension $\gamma_s = -36.36$ mJ/m^2. i.e. "negative surface tension". The interfacial surface tension ($p_\alpha = p_1 = 0.652$ kbar, $p_\beta = p_2 = -0.11667$ kbar and integrating from $r = 20$ Å to $r = 57$ Å) is $\gamma_i = 176.233$ mJ/m^2.

There are two interfaces in our system, one between water and fatty acid, and the second between fatty acid and vacuum. A negative surface tension would imply that the particle would tend to increase its interface either by deformation (so that it is no longer spherical) or by mixing. Since the fatty acid is essentially insoluble (see the density plot of the coated particle and the cross-sectional view of the particle), the only way to increase the area of the surface would be by deformation. However, the water-fatty acid interfacial tension is positive implying that this interface always tries to reduce its energy by reducing its surface area through maintaining a spherical shape (see the cross-sectional view of the coated particle in Figure 3.1). So there is a competition between the two tensions in which the water-fatty acid interfacial tension is of higher magnitude. Hence the particle stays spherical and forces the coating to maintain a spherical shape. Thus we have a stable spherical particle with an "effective" negative surface tension.

We also computed the normal pressure profile for the coated particle in the presence of water vapour. For this 56 W sites were introduced in the spherical cavity, outside the coated particle, and the system was allowed to evolve for 500ps. At the end of the equilibration period the density and pressure was evaluated. Some of the W sites were absorbed into the particle, with the rest remaining outside in the vapour phase. None of the W sites were seen to stick to the surface, and so the pressure profile was not affected by water vapour absorption (the coating remains under tension). The computed pressure profile is identical (within statistical noise) to the pressure profile obtained earlier, Figure 3.4.

Next we turn to the potential implications of this result to the atmosphere where these structures are most likely to be found. To study the effect of the coating on condensation, 1352 vapor "W" sites were introduced into the spherical cavity, outside the particle, with random velocity (sampled from the Boltzmann distribution, corresponding to the temperature of 254K). As observed in Figure 3.8, vapor phase water sites are absorbed into the particle indicating the propensity of the particle to process water even though it has a hydrophobic surface.

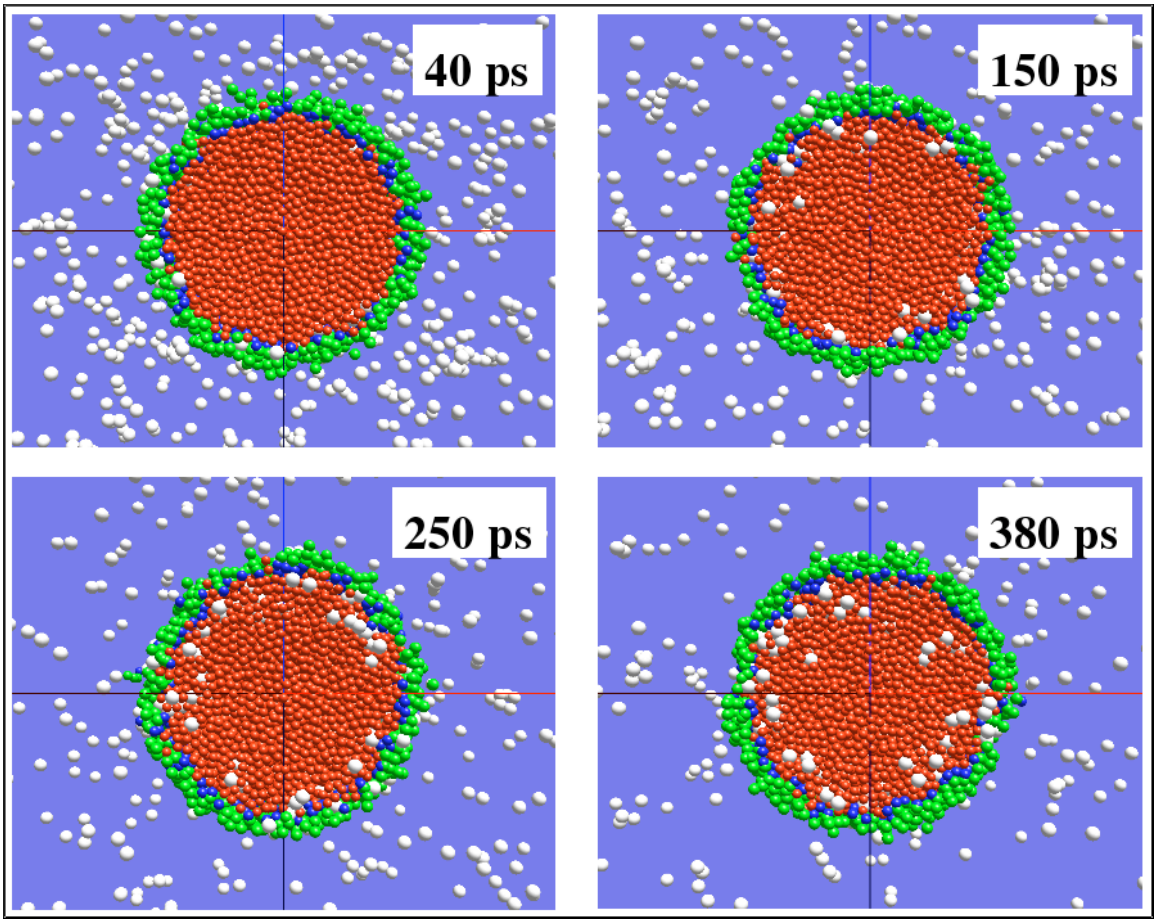

Figure 3.8: Snapshots of the coated particle processing water.

We believe that this condensation observed is due to the effective negative surface tension of the particle. The equilibrium vapor pressure over a small particle is higher than that over a flat surface and is given by the Kelvin equation[1]

$$\ln \frac{p}{p_S} = \frac{2\gamma \bar{v}}{r_p RT} \tag{3.9}$$

where p is the actual pressure of the vapour, p_S is the equilibrium vapour pressure for planar surface, r_p is the droplet radius, γ is the surface tension, $\bar{v}$ is the molar volume of the liquid, R is the gas constant and T is the temperature. Here we use the Kelvin equation for qualitative explanation since there is no other formalism that is suitable

for a graded structure of the type being considered here. There is of course a body of understanding for the vapour pressure of a drop containing a non-volatile solute[44, 45]. Li et al.[45], studied the effect of soluble surfactants on the activation of aerosol particles. They developed a model that partitions the surfactant between the droplet's gas-liquid interface and bulk volume, and computed Kohler curves with surfactant partitioning affecting the surface tension but not the Raoult effect. Sorjamaa et al.[44] extended this study to include effects of surfactant partitioning affecting both the surface tension, and the Raoult effect. However in both these works, the surface tension was assumed to follow the Szyskowski equation of state for large particles, the radius being of the order of 100nm. In our case, we've computed the surface tension of a much smaller particle (radius ~ 6-7nm). But the far more important and fundamental difference is that in contrast to the studies discussed above, the surfactant in our case is insoluble, and is on the surface of the droplet to form an inverted micelle (as is evident from the density profile of the coated particle), rather than being dispersed within the droplet. As a result, the water vapor sees only a hydrophobic surface, and not the presence of water inside. For the water vapor, the particle might very well be a pure droplet. And so an expression containing positive and negative terms resulting in the Kohler curves is not really appropriate. It is in that context the Kelvin equation for pure droplet comes in.

Normally, for a small particle, $p > p_S$. However if γ (surface tension) were in fact negative, we would have $p < p_S$, *i.e., the vapor pressure of the particle is reduced due to the organic coating, and thus a coated particle would act as an enhanced con-*

densation surface. This obviously poses many interesting questions as to how a oil surface can process water and its importance in the atmosphere.

When a sufficiently large amount of water vapor has assimilated into the water nucleus of the particle, the inverted micelle surface structure would be degraded. The surface would now consist of both water and fatty acid. For such partially coated particles, the surface tension needs to be recomputed, and the Raoult term added to the Kelvin equation.

The implication of this result is that organic coated water may be a very efficient substrate to process water vapor, and as such act as a surprisingly efficient water/cloud condensation nucleus. This result suggests that an experimental effort be undertaken to assess the nature of this effect, and the propensity of these structures to process water and other molecules.

4 Sticking Coefficient and Processing of Water Vapor on Organic Coated Nano Aerosols

4.1 Introduction

In the previous chapter, using coarse-grained molecular dynamics simulation, we showed that the organic coated nano aerosols favor an inverted micelle like structure (Figures 3.1 and 3.2). This structure results in a radial pressure profile (Figure 3.4) such that the coating is under negative pressure i.e. tension. Using a simple geometric model and force balance, we showed that this negative pressure is a manifestation of the curved surface. *This negative normal pressure corresponded to a 'negative' surface tension.* Now, the equilibrium vapor pressure over a small particle is higher than that over a flat surface and is given by the Kelvin equation $\ln\frac{p}{p_s}=\frac{2\gamma\bar{v}}{r_pRT}$, where p is the actual pressure of the vapor, p_S the equilibrium vapor pressure for planar surface, r_p is the droplet radius, γ is the surface tension, $\bar{v}$ is the molar volume of the liquid, R is the gas constant and T is the temperature. Normally, for a small particle, $p>p_S$. However, if γ were indeed negative, we will get $p<p_S$ i.e. the vapor pressure of the particle is reduced due to the coating and such a coated particle would act as an enhanced condensation surface. Indeed, we observed that water vapor introduced in the simulation cavity containing the coated particle was absorbed. Thus, despite the hydrophobic coating, such organic coated aerosols can possibly act

as a very efficient substrate to process water vapor. The implication of course is that such a structure may be important as a cloud condensation nucleus.

This chapter discusses the results of a systematic study, of water processing by the coated particles, done by computing the sticking coefficient of water vapor on such organic coated aerosols and show that these structures indeed will enhance water nucleation.

4.2 Computational Model and Simulation Details

All the molecular dynamics simulations in this work were performed using the GROMACS[33, 47] simulation software package implemented on a parallel architecture. For this work, we used the SPC/E water model[48, 49] that consists of a tetrahedral water model with an OH distance of 0.1 nm, with point charges on the oxygen and hydrogen positions of equal to –0.8476 and +0.4328e (electronic charge units), respectively, and a Lennard-Jones interaction on the oxygen positions, given by

$$V_{LJ}\left(r_{ij}\right) = 4\varepsilon\left[\left(\frac{\sigma}{r}\right)^{12} - \left(\frac{\sigma}{r}\right)^{6}\right] \tag{4.1}$$

where r is the distance between two non-bonded oxygen atoms. For these short-ranged force calculations the switched Lennard-Jones potential (normal up to 1.0 nm, after which it is switched to zero at a distance of 1.2 nm) was used. However, due to the lack of periodicity in the system, Coulombic interactions were computed between all the charges of the system. An analytical version of the SHAKE algorithm[50] was used to maintain the rigidity of the water molecules. Dodecanoic (Lauric) acid $[CH_3-(CH_2)_{10}\text{-}COOH]$ was chosen as our model fatty acid. These Fatty Acid molecules were modeled using both, 'united atom' setup (each CH_2 group was repre-

sented by a single site with interactions defined between these sites) and 'fully atomistic' setup (to represent the –COOH group). The bond stretching between adjacent atoms was modelled using the harmonic potential. The bond angle vibrations between a triplet of atoms was also represented by a harmonic potential on the angle made by the triplet. For the proper dihedral interaction, the periodic function $V_d\left(\phi_{ijkl}\right) = k_\varphi\left[1+\cos(n\varphi-\varphi_0)\right]$, where φ is the angle between *ijk* and *jkl* planes, with zero corresponding to the *cis* configuration. The harmonic improper potential was used to keep a planar group planar. And finally the O-H bond in the polar group was kept rigid using SHAKE. The GROMACS force field was used for all the bonded and non-bonded interactions. The equations of motion were integrated using leaf-frog algorithm with a time step of 2 fs. The simulations were typically conducted on 2-4 processors running in parallel, with a neighbor list cut-off distance of 1.4 nm. During the equilibration process, temperature was controlled by coupling the system to an external bath at the desired temperature using "berendsen" coupling with a coupling constant of 2 fs (equal to the time step). All the simulations were conducted in a constant energy environment.

4.3 Structure

The first step towards building an equilibrated coated particle was to build a pure water droplet. We first generated a simple cubic structure (with the Oxygen atom at the vertex of each cube) and then considered only the water molecules inside a sphere of a certain radius, thereby generating a spherical initial configuration consisting of 2440 water molecules. Generating velocities corresponding to 200 K, an equilibration simulation was run for 50 ps. The particle was then slowly heated to 260

K over a period of 120 ps. Finally a constant temperature simulation is run for 100 ps keeping the temperature constant at 260 K. The radial distribution function, confirms the liquid water state (the peak occurs at the expected distance of $2.8\,\mathring{A}$). Fatty acid molecules were then attached to the surface water molecules to coat the water droplet. The polar part of the fatty acid molecule was attached to a surface water molecule with the hydrocarbon tail placed radially outwards. Following a brief energy minimization step, using Steepest Descent, to untangle some possible overlaps, velocities were initialized for these fatty acid molecules corresponding to a temperature of 260 K, and the coated particle was allowed to equilibrate. Figure 4.1 shows a cross-sectional view of the equilibrated coated particle consisting of 2440 water molecules and 505 fatty acid molecules. The coated particle was next heated to 300 K and equilibrated at that temperature.

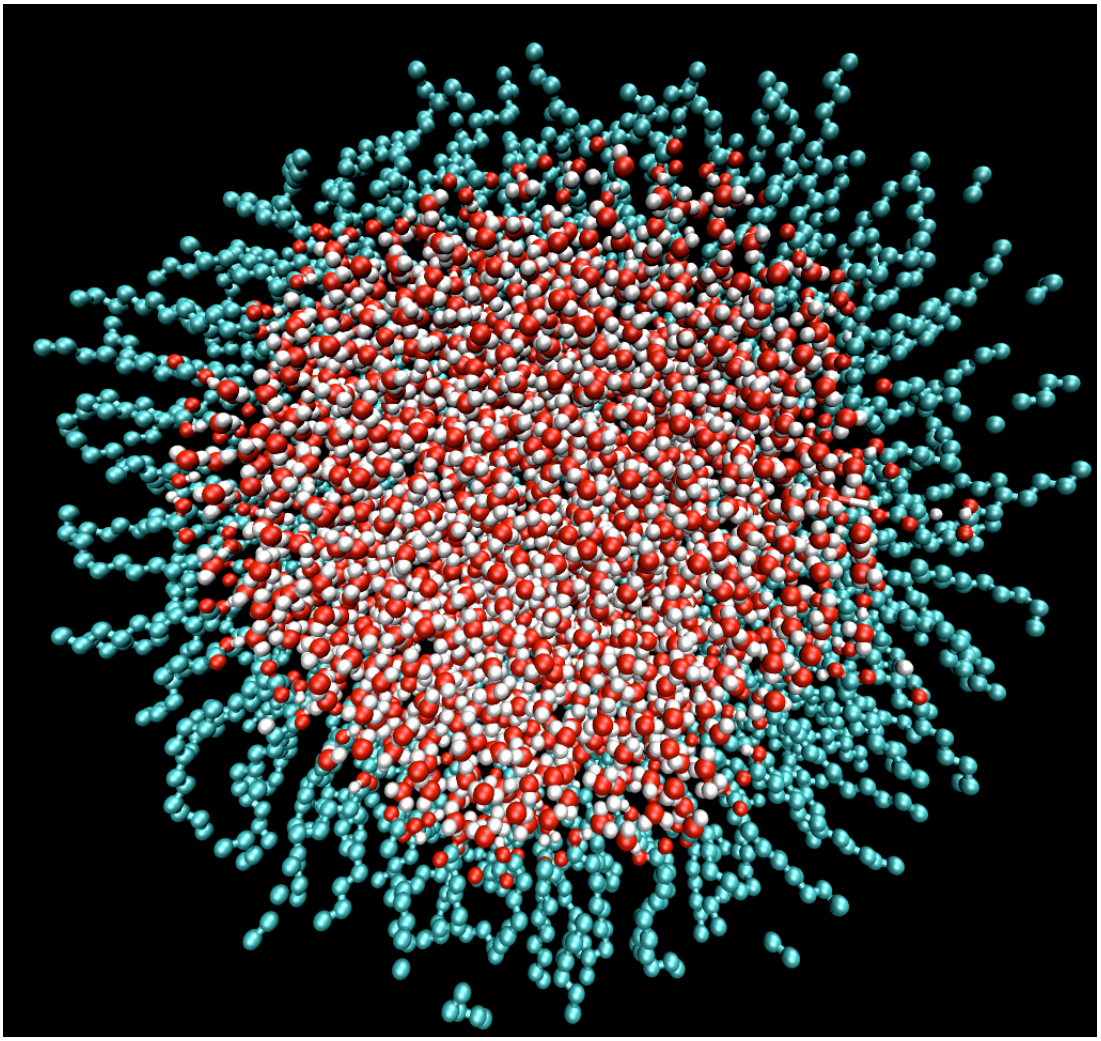

Figure 4.1: Cross sectional view of an equilibrated, coated particle at 260 K (consisting of 2440 water molecules and 505 fatty acid molecules).

4.3.1 Density

The radial density profile was computed[42] as a function of *r*, the distance from the center of mass of the particle. To compute density, we introduced sub-spherical shells (centered at the center of mass of the coated particle) at a distance of $\delta r = 0.05$ nm from each other. The density at a distance *r* from the center of mass was com-

puted as the mass of all the atoms in the shell between radii r and $r + \delta r$ divided by the volume of the shell. Figure 4.2 shows the density plot for the coated droplet.

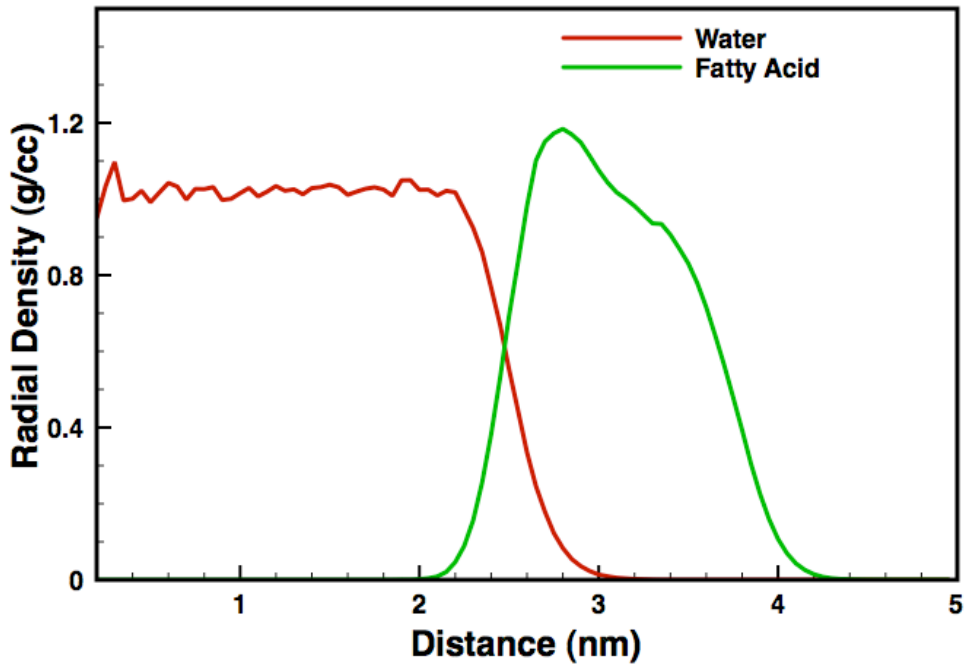

Figure 4.2: Radial density profiles of the coated particle. Distance is measured radially outwards from the center of mass of the particle.

As we had seen in our earlier work, using CG models – documented in the previous chapter, the particle exhibits a core-shell like structure with an aqueous core encapsulated in an inert hydrophobic organic monolayer. The fatty acid molecules stay on the surface of the water droplet forming a hydrophobic coating. As we had pointed out this structure is mechanically stable.

4.4 Effect of Heating on Stability:

We tested the stability of both the bare and the coated particles by heating them slowly from 260 K to 400 K (the temperature ramp for both the pure and the coated particles over time is shown is Figure 4.3). To quantify stability we computed the RMSD (Root Mean Square Deviation),

$$\mathrm{RMSD}(t) = \left[\frac{1}{N^2} \sum_{i=1}^{N} \sum_{j=1}^{N} \left\| \mathbf{r}_{ij}(t) - \mathbf{r}_{ij}(0) \right\|^2 \right]^{1/2} \tag{4.2}$$

where the distance $\mathbf{r}_{ij}$ between N atoms at time t is compared with the distance between the same atoms at time 0. The RMSD of water molecules as a function of time for both the pure and the coated particles was computed and is plotted in Figure 4.3.

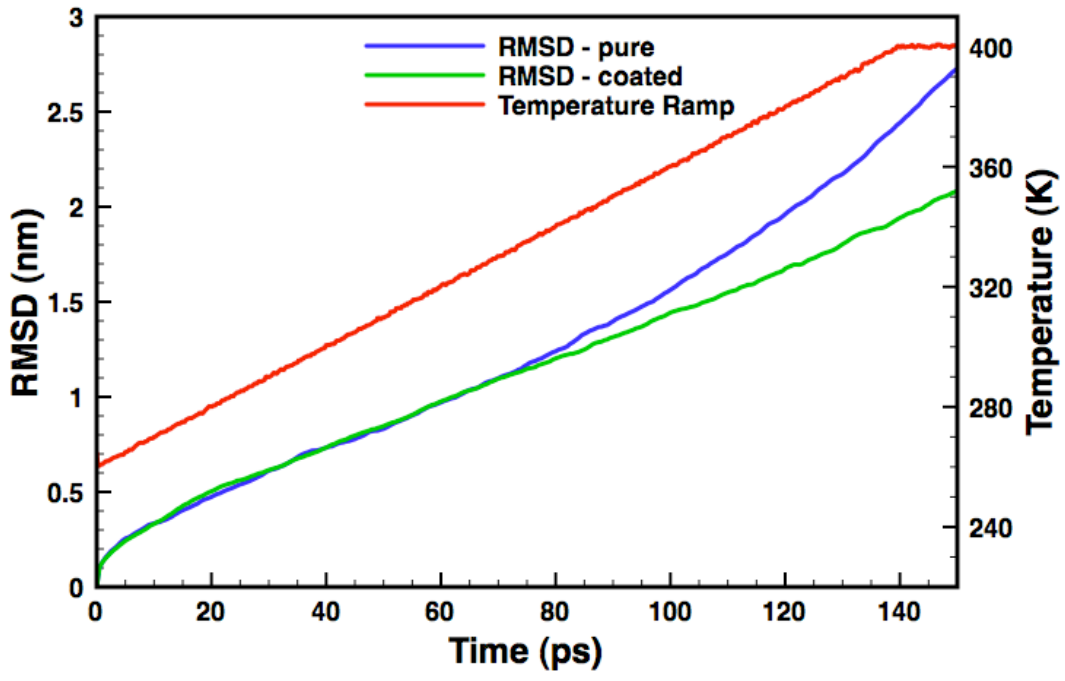

Figure 4.3: Root Mean Square Deviations of water molcules in the pure and coated particles during a heating ramp (red line).

Evidently, and as expected, the fatty acid coating increased the stability of the water droplet. While the RMSD for both materials increased with temperature there is a clear bifurcation at about 300 K where the water droplet RMSD exceeds that of the coated drop. The RMSF (Root Mean Square Fluctuations), defined as the standard deviation (from the original equilibrated structure) of atomic positions of each of the atoms in the particles, were also computed for both the particles. Figures 4.4 (a, b) plot the RMS fluctuations for both types of particles. The x-axis of the plots lists the atom indexes (2440 water molecules implying 7320 atoms) and the y-axis is the measure of the fluctuation in nm. The median of the deviations is 0.84nm.

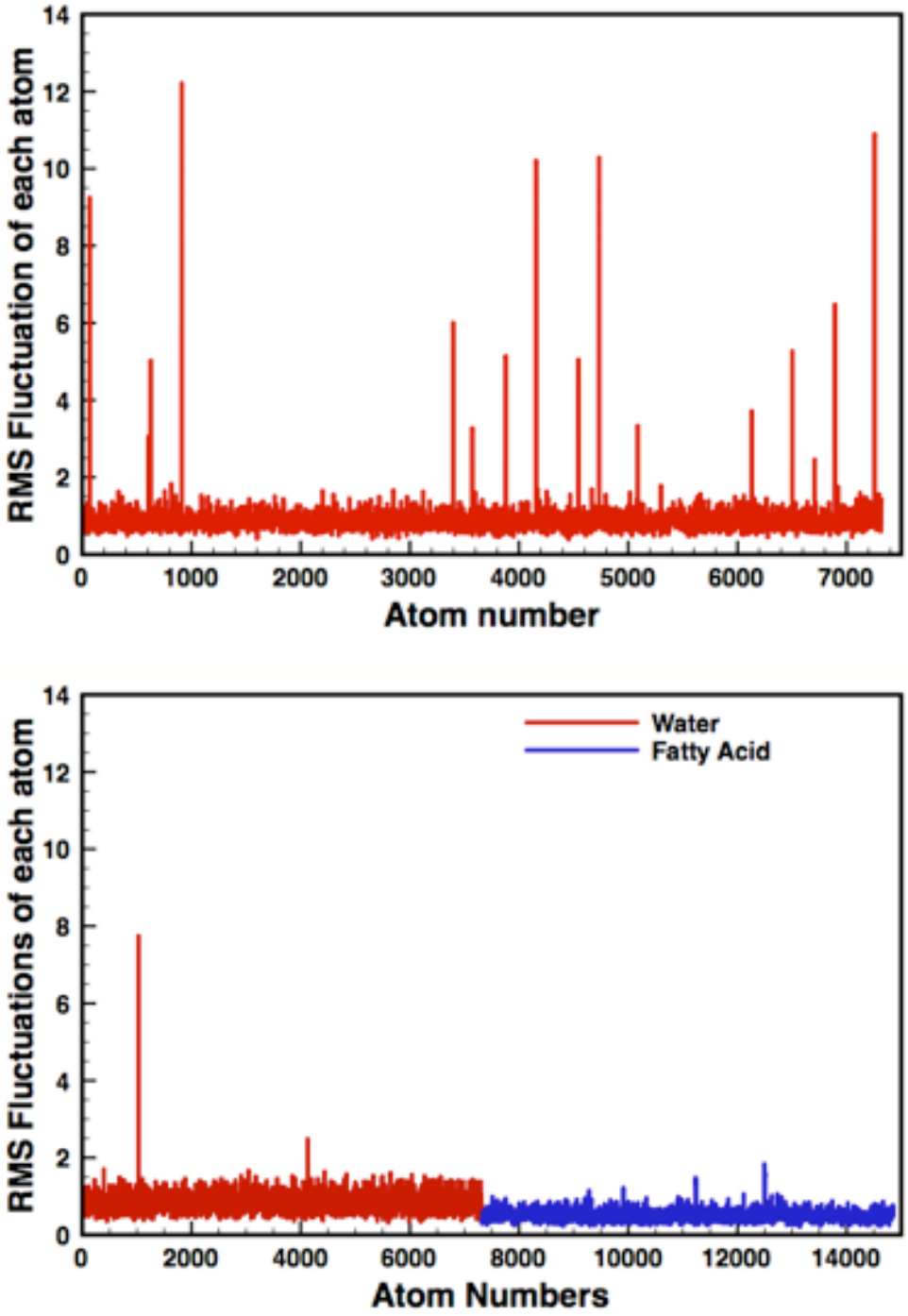

Figure 4.4: (a) Root Mean Square Fluctuations (RMSF) of each atom in the pure water droplet resulting from heating. (b) RMSF of each atom in the coated droplet resulting from heating,

In the case of the pure water droplet 16 water molecules were seen to evaporate as a result of the heating, as compared with just 2 water molecules evaporating in the case of the coated particle for the same temperature ramp confirming the fact that the water molecules in the coated droplet are far more stable than their counterparts in the pure droplet. Heating the pure water droplet to 300 K results in some evaporation from the surface. However, the coated particle is stable at 300 K (no evaporation takes place over a period of 100 ps) and we have used the coated particle at this temperature for the subsequent computation of the sticking coefficient and average energy transferred per collision. The sticking coefficient and energy transfer calculations were carried out in a constant energy environment using the coated particle equilibrated at 300 K.

4.5 Water Vapor Sticking Coefficient

The Sticking (Mass Accommodation) Coefficient or Sticking Probability, α, describes the probability of the gas molecule being incorporated into the liquid[51]

$$\alpha = \frac{\text{Number of molecules absorbed into liquid}}{\text{Number of molecules iminging the liquid surface}} \tag{4.3}$$

An accurate determination of the sticking probability is important since it is directly relevant to the nucleation and growth kinetics of cloud droplets, and subsequently climate change[52, 53]. Vieceli et. al.[51] computed the sticking coefficient of a gas phase water molecule, approaching the surface of liquid water (flat surface) with a thermal impact velocity, and obtained a value of effectively unity (0.99 at 300 K). Morita et. al.[54] computed the mass accommodation coefficient of water vapor into liquid water (flat surface) and found the value of α to be > 0.99 at 273 K. The sticking probability

of water vapor onto an organic coated spherical water droplet has not been computed to the best of our knowledge.

To address this point we carried out a water processing simulation in which we placed water vapor outside the particle with a random velocity (sampled from the Maxwell-Boltzmann distribution) corresponding to the desired temperature. A water monomer (single water molecule) was placed at a distance of 6nm from the center of the coated particle, outside the potential cut-off distance so that initially there is no force acting between the monomer and the coated particle. The molecule was then given a speed towards the center of mass of the coated particle. For each incident speed, sampled at random from the Maxwell-Boltzmann speed distribution at 300 K, Figure 4.5, 102 separate trajectories were considered by placing the water monomer along the sphere of radius 6 nm. The sticking coefficient was computed as the ratio of the number of monomers trapped on the coated particle to the number of monomers impinging on the surface (102 in the present case). The trajectory of each monomer was monitored for 60 ps and this process was repeated for all collision events. The incident water molecule was considered ‘trapped’ on the particle if the distance of the center of mass of the monomer from the center of mass of the particle was less than 5nm, else it was considered an unreactive event.

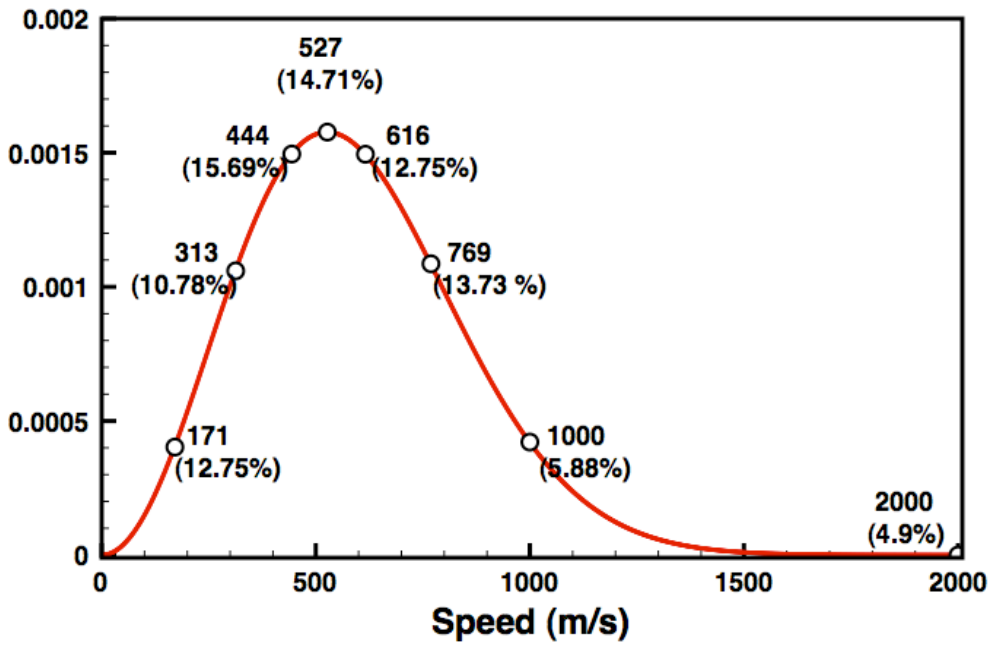

Figure 4.5: Sticking Coefficients of water monomer for various values of incident speeds on a Maxwell-Boltzmann speed distribution at 300K. %age values in parenthesis are the fraction of sticking collisions at the given speed.

Figure 4.5 shows the percentage of monomers (i.e. sticking coefficient, presented as percentages within parentheses) that get trapped on the particle for each of the incident energies considered. The sticking coefficient is essentially a constant (within 5%) for incident speeds around the most probable speed and reduces significantly at higher incident speeds (>1000 m/s). In general, the results indicate that approximately one in every 6-7 encounters results in water condensation. Next, we carried out the same trajectory calculations with the equilibrated pure water particle and placing the incident water monomer at a distance of 5nm from the center of the particle (this time the trajectories were calculated at a temperature 260 K with speeds sampled from the corresponding Boltzmann distribution). For the pure water droplet,

all the incident monomers were absorbed into the water droplet implying that the pure water droplet has a sticking coefficient of 1.

Finally, we considered a sequence of water-Nmers of different sizes (N=1 for monomers, N=2 for dimers etc) each shot towards the center of the particle with its corresponding most probable speed (as determined from the Maxwell-Boltzmann distribution). Figure 4.6 plots the sticking coefficients (at the most probable speed) as a function of the water-Nmer size (N).

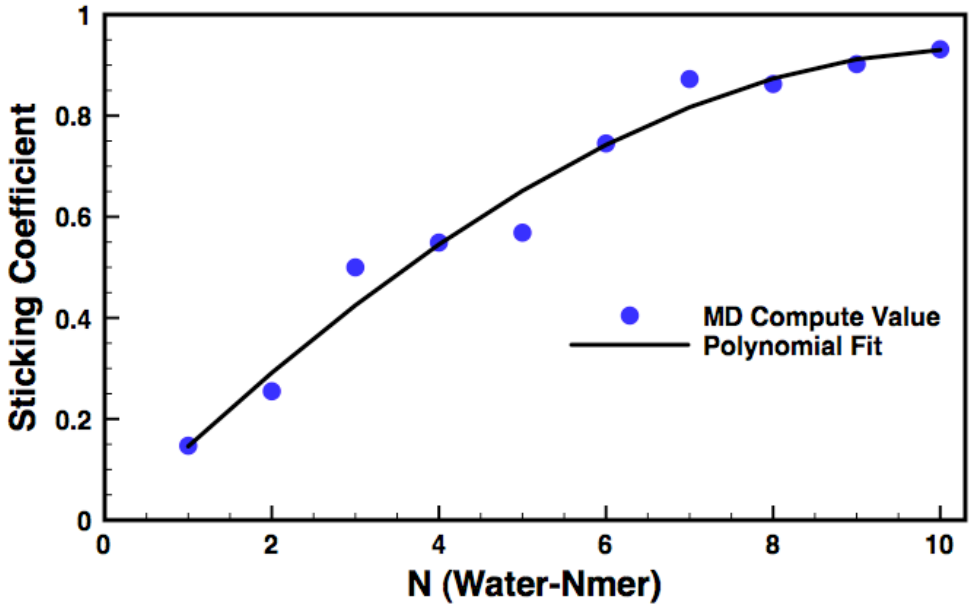

Figure 4.6: Sticking Coefficients for water-Nmers of different sizes for different values of N.

We find that the sticking coefficient increases smoothly with increasing water-mer size and approaches 1 for N >10.

4.6 Energy Transferred Due to Collision

For a monomer colliding with the coated particle, we noticed three types of collisions[55]. The incident water monomer either underwent (a) Immediate (almost specular) reflection upon contact, or (b) underwent surface diffusion and eventually gained enough energy to desorb from the surface (diffused reflection), or (c) penetrated through the fatty acid coating and was absorbed into the water core of the particle. These three cases are illustrated in Figure 4.7, which plots the time evolution of the distance of the center of mass of the monomer from the center of mass of the particle (the curves shown are typical examples of each case).

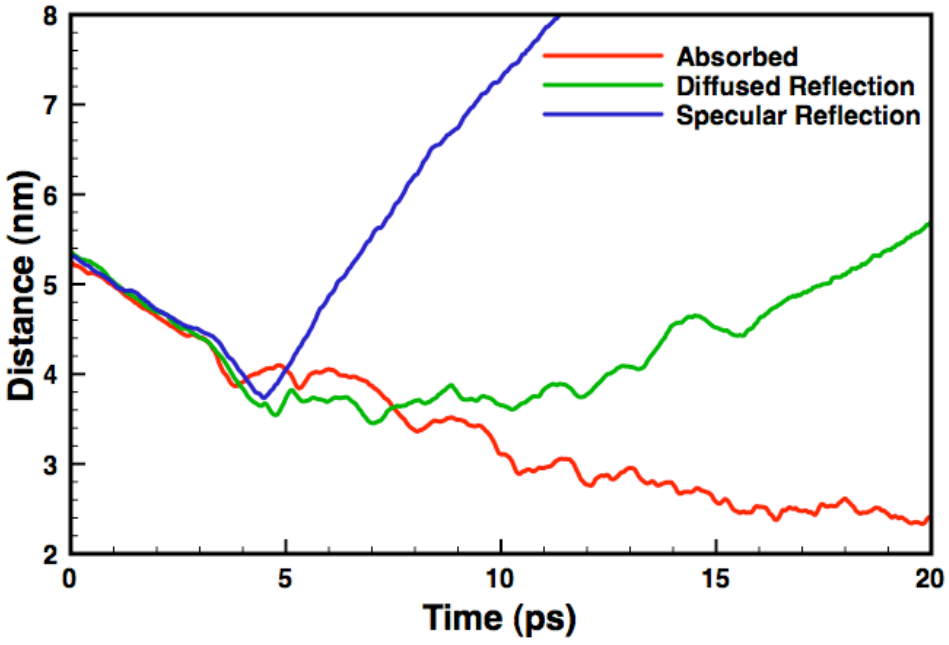

Figure 4.7: Distance of the center of mass of the incident monomer from the center of mass of the coated particle plotted as a function of time for the three types of interactions.

Subsequently, for each incident speed case, the average distance of the monomer from the particle was computed (the average being taken over all the reflected trajectories, including both the specular and diffuse reflection cases). The result is summarized in Figure 4.8.

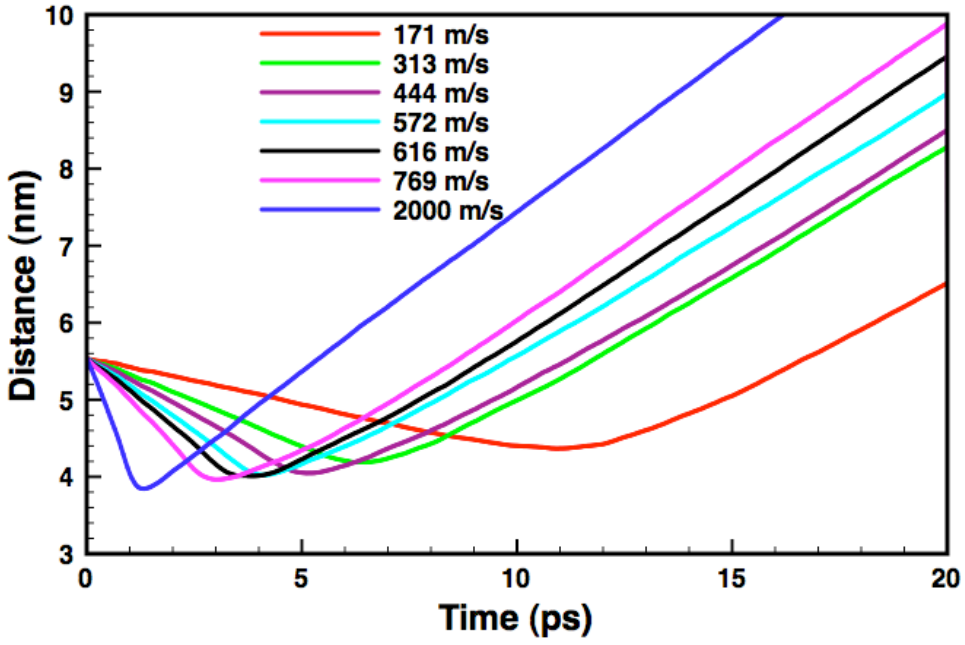

Figure 4.8: Plot of the distance of the center of mass of the monomer from the center of mass of the coated particle Vs time. Each trajectory obtained has been averaged over all the reflected trajectories for a given incident speed.

It is evident that the monomers with higher incident energies spend less time on the surface of the particle, and undergo a more specular reflection and less energy accommodation. It is interesting to note that the higher energy monomers penetrate the surface of the coated particle more than their lower energy counterparts. On an average the monomers with incident speed of 2000m/s travel a distance of 0.5nm deeper into the coating than those with an incident speed of 171m/s.

Next, for each incident speed case, we computed the change in the total kinetic energy (KE) due to collision. Towards that end, we tracked the KE for all the trajectories and took an average of the KE over all the reflected trajectories. Figure 4.9 plots the (averaged) time evolution of KE for each incident speed case.

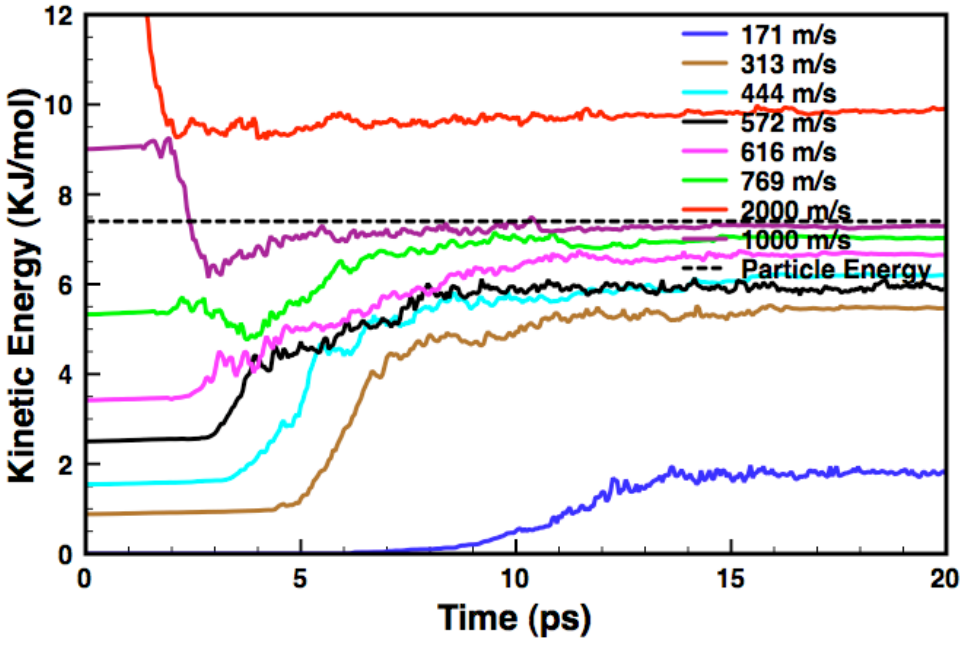

Figure 4.9: Plot of the change in Kinetic Energy of a monomer Vs time. Each trajectory has been averaged over all the reflected trajectories for a given incident speed. The 'dashed' line represents the thermal energy of the coated particle.

As expected, monomers with incident energy lower than the thermal energy of the particle gain energy from the particle resulting in a positive change in KE whereas for the monomers impinging the particle with a higher energy, the change in energy is negative. The absolute value of this change in Kinetic Energy (ΔE = Final KE – Initial KE) is plotted in Figure 4.10 (black circles).

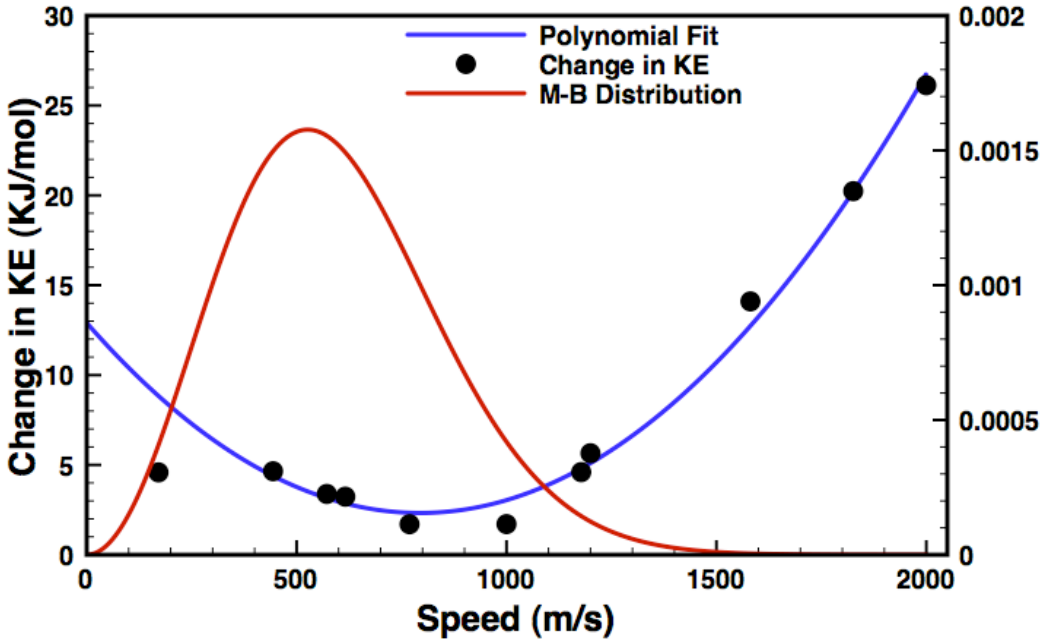

Figure 4.10: The change in KE is plotted for each incident speed case. The blue line is a polynomial (degree 2) fit to the change in KE data and is used to compute the average energy transferred per collision. Also plotted is the Maxwell-Boltzmann distribution for a water monomer at 300K.

To obtain a functional form for $|\Delta E|$, we fitted a polynomial of degree 2 to this MD computed data (represented by the blue line in Figure 4.10). Using this fitted functional form of $|\Delta E|$, we computed the average energy transferred per collision as

$$\left\langle \Delta E^2 \right\rangle^{1/2} = \left(\int_0^\infty \left(\Delta E^2 \right) f(v) dv \right)^{1/2} \tag{4.4}$$

where *f(v)* is the Maxwell-Boltzmann distribution of speed (Figure 4.10). The computed value of the average energy transferred per collision is 4.4581 KJ/mol, i.e. 372.67 cm^{-1}. This value is consistent with the value obtained[56] for a highly excited polyatomic colliding with a monoatomic bath gas.

4.7 Negative Surface Tension and Reduction in Vapor Pressure

As mentioned earlier, coated particles with core-shell structure would act as if the surface tension is negative and is a direct consequence of the fatty acid molecules being under tension, which gives rise to a negative normal pressure profile in that region. Mechanically this effect occurs because the effective density of fatty acid chains decrease as one moves radially out from the anchor point of the chains at the water interface. This latter point was demonstrated using a simple geometrical argument and force balance. A negative surface tension implies that a particle would tend to increase its surface area, possibly by deformation so that a majority of the fatty acid molecules line up parallel to each other (thereby reducing the tension in the coating). This phenomenon is however never seen with fully coated particles because of the high concentration of fatty acid molecules on the surface of the particle resulting in a large interfacial tension, which maintains the spherical shape of the particle. As an example we removed 80% of the fatty acid molecules from the surface of the fully coated particle (the resulting particle consisted of 2440 water molecules and 101 fatty acid molecules) and let the system equilibrate for 20 ns. Figure 4.11 (a-e) shows snapshots of this simulation.

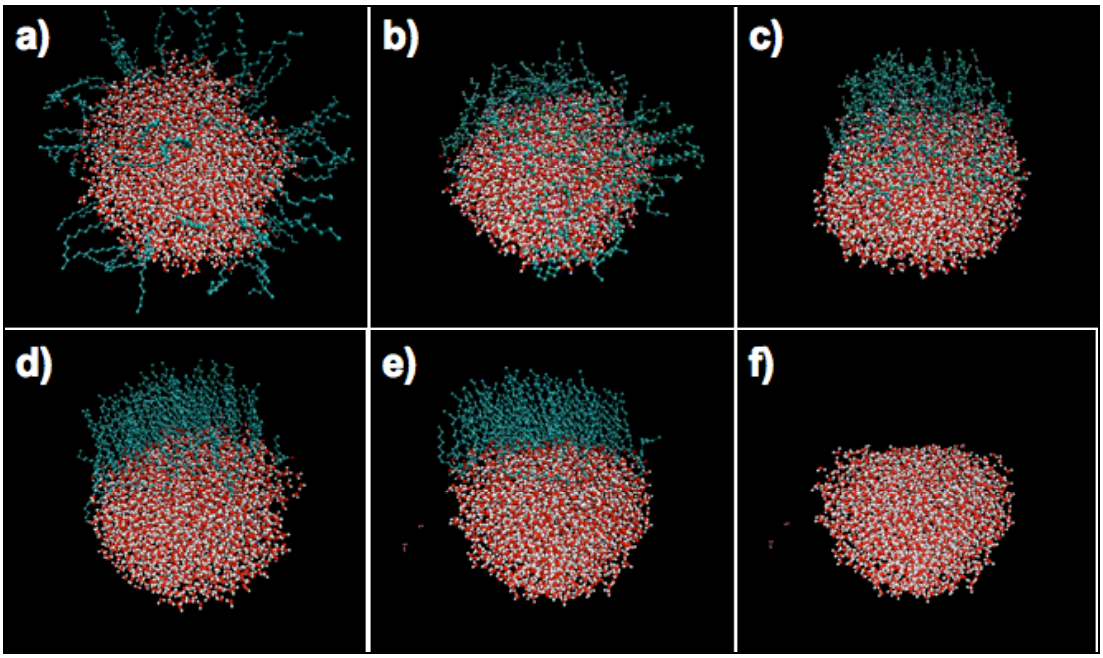

Figure 4.11: (a-e) Snapshots of the equilibrium process of a particle consisting of 2440 water and 101 fatty acid molecules. (f) is the snapshot of the final equilibrated structure without the fatty acid molecules (emphasizing the flat interface).

Panel (a) shows the initial particle. The fatty acid molecules that were initially spread out on the surface of the particle diffuse and nucleate to form a monolayer on a part of the droplet. Panel (e) shows the equilibrated structure where the fatty acid molecules line up parallel to each other on a locally flat surface (panel f). From (f) it is evident that although the rest of the water surface maintains a roughly spherical shape, the part of the surface in contact with fatty acid becomes flat enabling the fatty acid molecules to line up.

One direct implication of the 'negative' surface tension is that it reduces the equilibrium water vapor pressure. As a result a coated particle would act as an effective substrate for water condensation despite its hydrophobic surface. To test this, a pure water droplet, equilibrated at 260 K, was placed in the center of a cubic box of

edge 15 nm with periodic boundary conditions, and heated slowly to 300 K (over a period of 120 ps), and maintained for another 5 ns. The water droplet reaches equilibrium by evaporating some of the water so that at steady state on average 14 water molecules exist in the vapor phase. A water molecule was considered to be in the vapor phase if its distance from the centre of particle exceeded 6nm. This corresponds to an equilibrium vapor pressure of 0.15 atm. Next, the water droplet was replaced with the coated droplet (at 300 K) keeping the water vapor in place. The system was then allowed to evolve for a total of 20 ns. Figure 4.12 shows snapshots of this simulation. In the figure, water molecules in the vapor phase have been represented by larger spheres for easy identification.

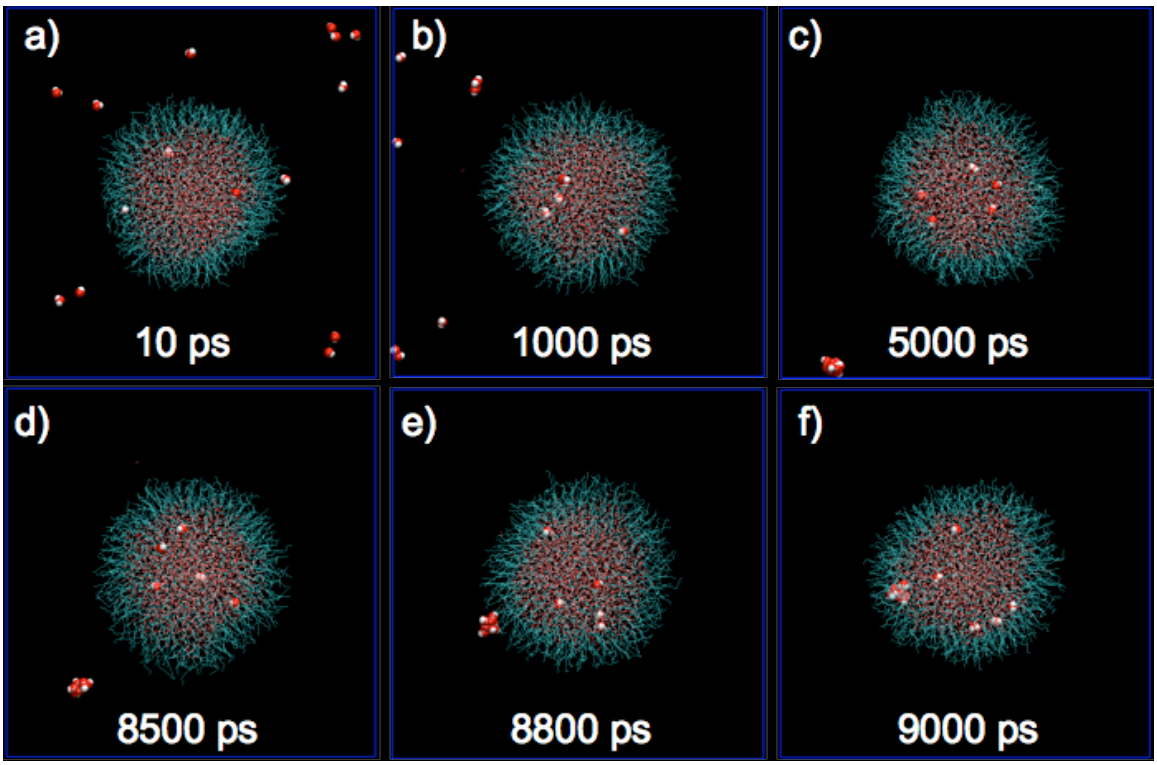

Figure 4.12: Orthographic snapshots of various stages of the 20ns simulation to test the reduction in vapor pressure because of the coating. Larger spheres are used to represent the water molecules in the vapor phase.

Panel (a) is a snapshot taken soon after the start of the simulation. In the first 20ps two vapor molecules penetrate the coating of the particle and get absorbed into the water core of the particle. The rest of the vapor molecules were seen to be reflected off the surface of the particle. Over a period of next 8 ns, the 12 vapor molecules came together to form a water-12mer. This water cluster, upon striking the surface of the particle (panels (d), (e)), was completely absorbed (panel (f)) into the water core of the particle (sticking coefficient is ~ 1 for water Nmers with N>10, Figure 4.5). Figure 4.13 plots the number of water molecules in the vapor phase as a function of time.

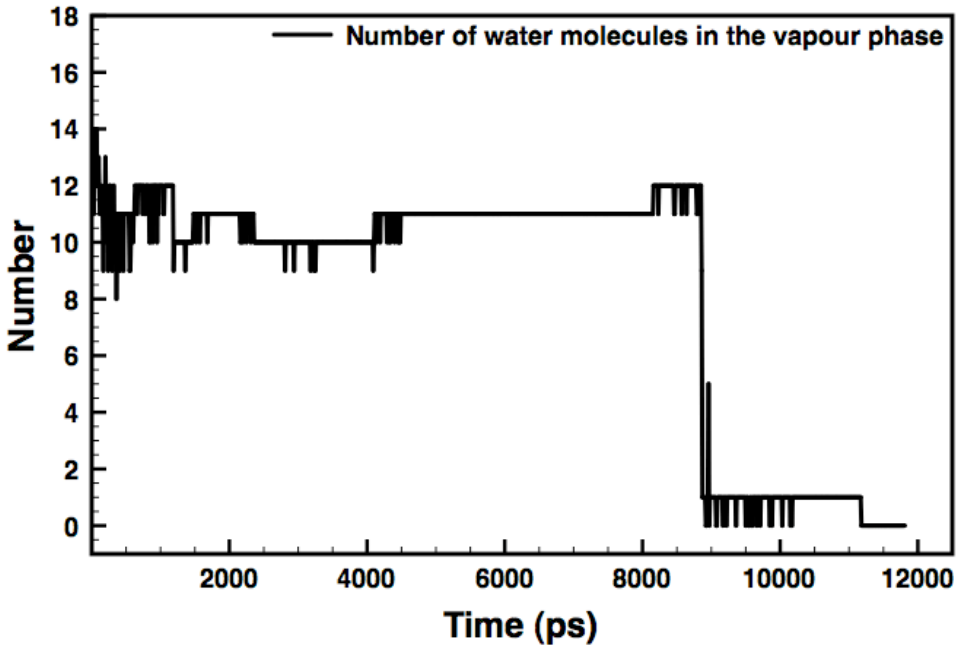

Figure 4.13: Plot of the number of water molecules in the vapor phase as a function of time.

The implications of this computer experiment are clear:

- *the equilibrium vapor pressure of water is considerably lower in the presence of the coated particles*. Indeed it was sufficiently low that it induced homogeneous nucleation to occur in the simulation box.
- Determining the actual equilibrium vapor pressure is not feasible using a traditional molecular dynamics approach at ambient temperatures, because it would require an exceedingly large simulation box to obtain the low water vapor density, so that the evaporation and condensation rates match. Indeed over the simulation times investigated in this paper we never observed a water molecule to evaporate from a coated particle at 300 K.

This latter point is interesting in that the vapor pressure of these inverted micelles structures are very low despite the fact that the sticking coefficient is about one sixth that of a pure water-water drop encounter.

5 On the structure of organic coated nanodroplets

5.1 Introduction

In our previous work (Chapter 3), using CG models, we observed that fatty acid coated water droplets indeed favored an inverted micelle like structure. The resulting profile of the normal component of the Irving-Kirkwood pressure tensor indicated that for such structures the coating would be under negative pressure, i.e. tension. Using a simple ball-stick model and force balance arguments, we showed that the negative pressure was a result of the curved water-fatty acid interface, which resulted in lower chain-chain interaction with increasing radial distance. Because of the tension in the organic coating, it was argued that such particles would behave in a manner consistent with a *negative surface tension*, and consequently would have an inverse Kelvin vapor pressure effect resulting in increased water condensation. A simulation was carried out in which water vapor was placed in the simulation cavity along with the coated drop and the system was allowed to evolve. The vapor phase water was seen to be absorbed into the particle indicating the propensity of such particles to process water despite their hydrophobic surface. It was thus concluded that organic coated water might be a very efficient substrate to process water vapor.

Following that work, we undertook an effort to quantify water processing (Chapter 4). It was found that the rate of water uptake (sticking coefficient of water vapor on coated drops) was essentially a constant with one in six-seven collisions resulting in a stick, as compared to 100% for pure water droplets. We also observed that

the equilibrium vapor pressure of the coated drop was too small to measure, and thus considerably smaller than a bare water drop. The implication was that these apparently oily droplets are in fact *net water attractors* even though the sticking coefficient was a factor of 6 smaller.

In this chapter, we have extended our earlier studies to look at the effect of fatty acid chain length, chain branching, and terminal group on the morphology, internal pressure profile, surface tension and water processing properties. The computational model used has been described in section 4.3. The software LAMMPS[57] was used since it provided greater flexibility to modify the source code. A sample LAMMPS input script file containing the potential parameters is listed in the appendix. The GROMACS[33, 47] force field was used for bonded and non-bonded interactions as before.

5.2 Water droplet coated with fatty acid – structure and properties

5.2.1 Water droplet – structure and properties

Radial density and the normal component of Irving-Kirkwood pressure tensor: For the spherical water droplet, both density and pressure profiles were computed as a function of r [42], (i.e. the distance from the center of mass of the droplet). Radial density and pressure computations were carried out as before. For these calculations, concentric sub-spherical shells, centered at the center of mass, were introduced at a distance of 1 $\mathring{A}$ from each other. The density and pressure were averaged over 500 snapshots collected over a period of 250 ps. Figure 5.1 plots the density and pressure of the water droplet equilibrated at 260 K. The computed density is consistent with

bulk water and as expected, the interior of the particle is under compression, and for this droplet has an interior pressure ~ 560 bar.

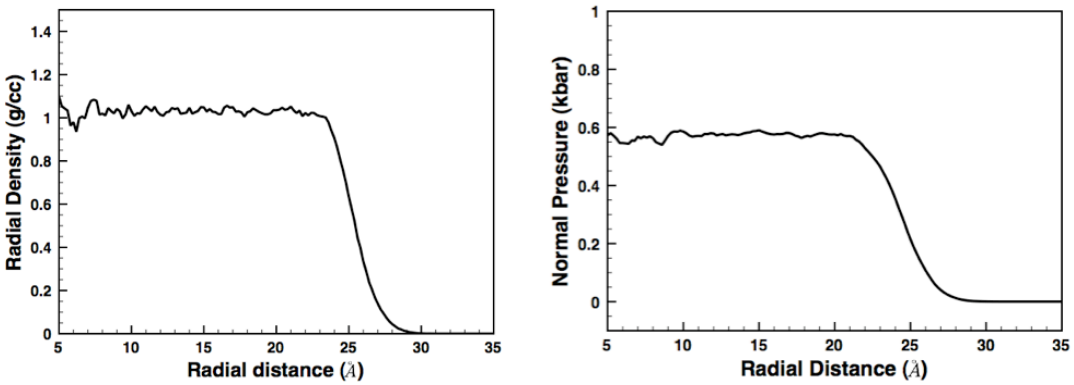

Figure 5.1: Density and normal pressure profiles of a pure water droplet consisting of 2440 water molecules

Surface Tension: The internal pressure profile enables us to compute the surface tension using the mechanical route as described in Chapters 2 and 3. Using the relation

$$\gamma_s^3 = -\frac{1}{8}(p_l - p_g)^2 \int_0^\infty r^3 \frac{dp_N}{dr}\, dr \tag{5.3}$$

(p_l and p_g are the bulk pressures in the liquid and gaseous phases respectively and γ_s is the surface tension) with p_l = 0.56 kbar, p_g = 0.0 kbar and integrating from 0 to 50 $\mathring{A}$, we get a surface tension of γ_s = 69.8 mJ/m^2. Zakharov et. al.[58], using small water clusters (64-512 water molecules) and the TIP4P model, had computed the surface tension of water droplets to be 54 mJ/m^2. Using coarse-grained models, we had earlier found the surface tension to be 166 mJ/m^2, which was off by a factor of two. Using SPC/E water model and a cluster size of 2440 water molecules our 69.8 mJ/m^2 is very close to the accepted value of 72 mJ/m^2.

5.2.2 C12 and C20 fatty acid chains

To study the structures of water droplets coated with fatty acid, a total of three particles were constructed. The first of these particles (C12 - the '12' refers to the number of carbon atoms in the fatty acid molecule) consisted of 2440 water molecules and 505 dodecanoic acid molecules made using the process described in section 4.3. Figure 5.2 shows a snapshot of the equilibrated C12 particle along with the underlying water substrate. The particle clearly exhibits an inverted micelle structure with the polar head of surfactant molecules binding to the polar water surface with the hydrophobic hydrocarbon chain oriented radially outwards. Following the equilibration of the C12 particle, the terminal CH_3 group of each fatty acid molecule was identified and replaced with a CH_2 group. Eight more hydrocarbon beads were added to each of the fatty acid molecules to form the C20 particle. This newly formed particle's energy was minimized and the particle was allowed to equilibrate. The C20 particle was found to have a structure very similar to the C12 particle.

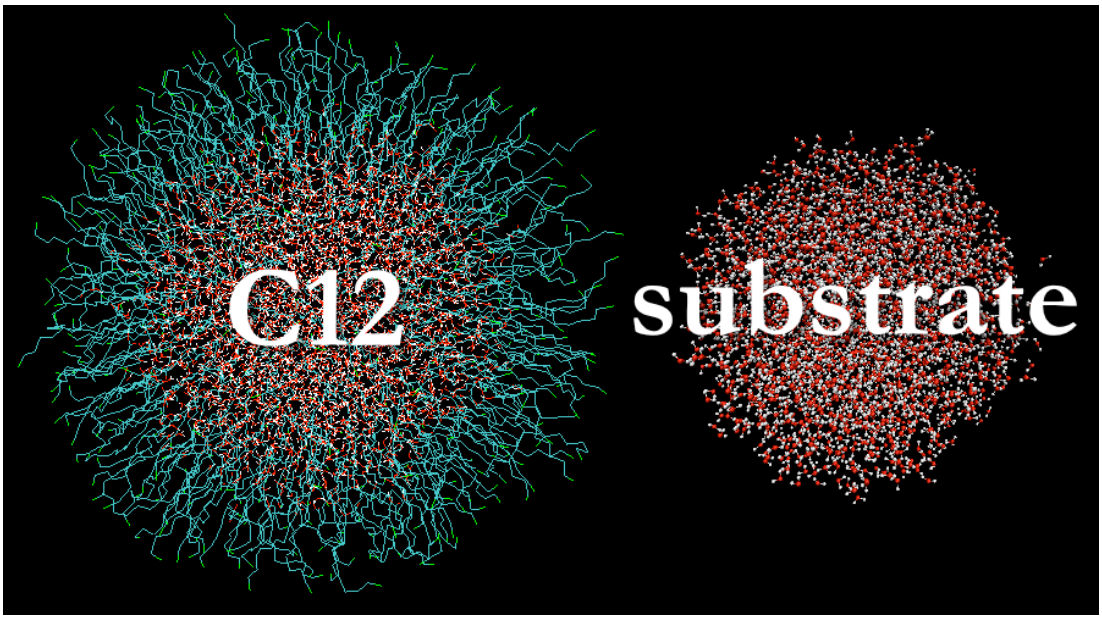

Figure 5.2: Equilibrated C12 particle along with the underlying water substrate

Density, Pressure and Surface Tension Calculations

The density and pressure profiles for the C12 and C20 particles were computed. Figure 5.3 plots the density profile of the C12 particle. As is evident from Figure 5.3 (also the first panel of Figure 5.2), this coated particle, as expected, prefers an inverted micelle structure with the fatty acid staying on the surface of the particle and no dissolution within the droplet.

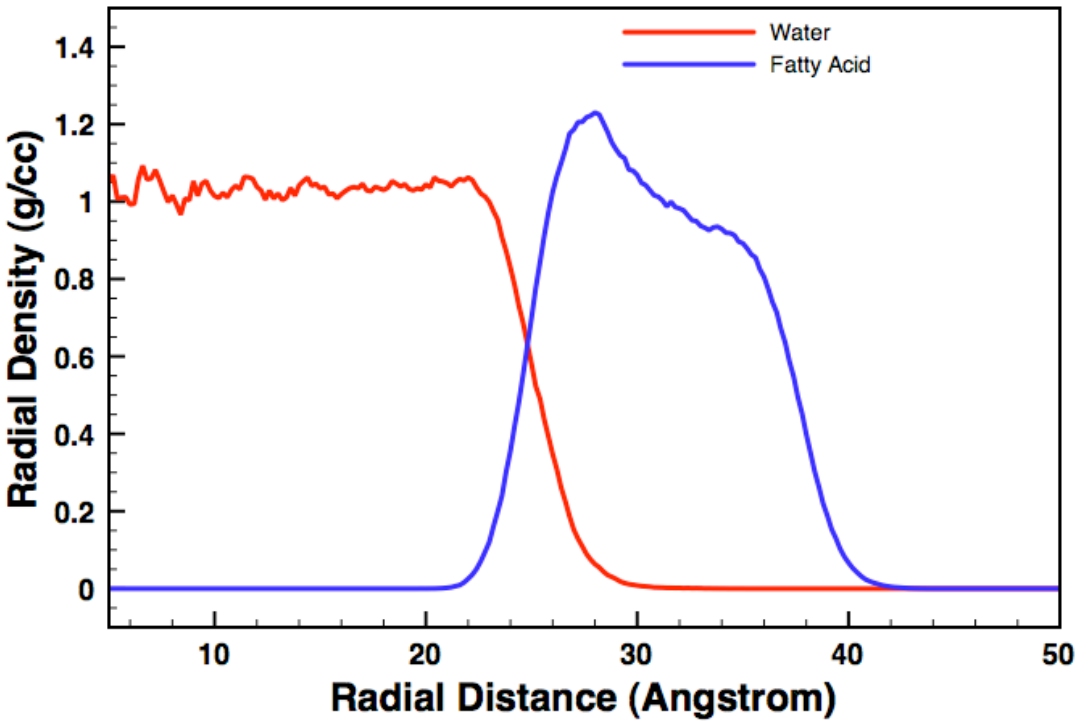

Figure 5.3: Radial density profile of the C12 particle

Following the density calculations, the normal pressure profile was computed. Figure 5.4 plots the pressure profiles of the C12 particle. Also included in the figure is the density profile of the coating. Consistent with our earlier work with coarse-grained models, the interior of the particle is under compression. However, the coating is under negative pressure, i.e. tension.

In our work to show negative surface tension[26], we had extended the Widom[43] method of calculating surface tension to 3 phases. The interfacial tension (at the water-fatty acid interface) is given by

$$\gamma_i^{3} = -\frac{1}{8}\left(p_\alpha - p_\beta\right)^2 \int_{R^\alpha}^{R^\beta} r^3 \frac{dp_N(r)}{dr}\, dr \qquad (5.4)$$

where p_α, p_β are the bulk pressure in the phases α and β respectively. Using p_α = 0.573 kbar, p_β=-0.042 kbar and integrating from $R^\alpha = 0$ Å to $R^\beta = 30.8$ Å, we obtain an interfacial tension (at the water-fatty acid interface) of $\gamma_i = 81.2$ mJ/m^2.

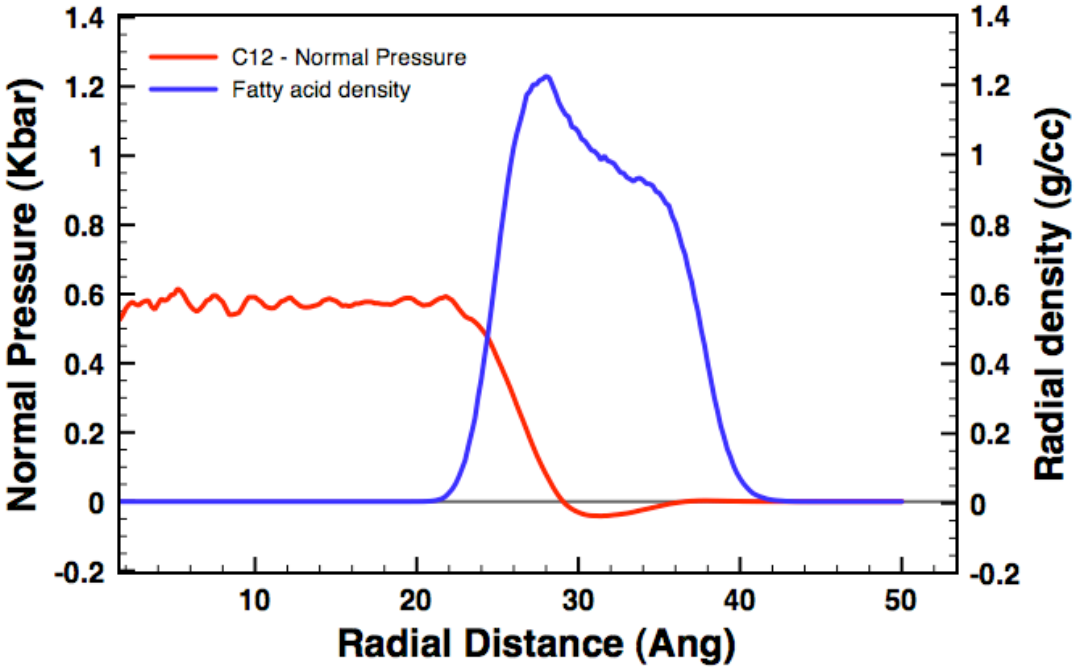

Figure 5.4: Normal pressure profile of the C121 particle. The blue curve represents the coating density

Using a relation similar to Equation 5.4 with p_α = -0.042 kbar, p_β = 0.0 kbar and integrating from R^α = 30.9 to R^β = 50.0 Å we obtain a surface tension (at the fatty acid-air interface) of γ_S = -7.1 mJ/m^2. Figure 5.5 plots the normal pressure profile of the C20 particle. Also included, for reference, the pressure profile for the C12 particle.

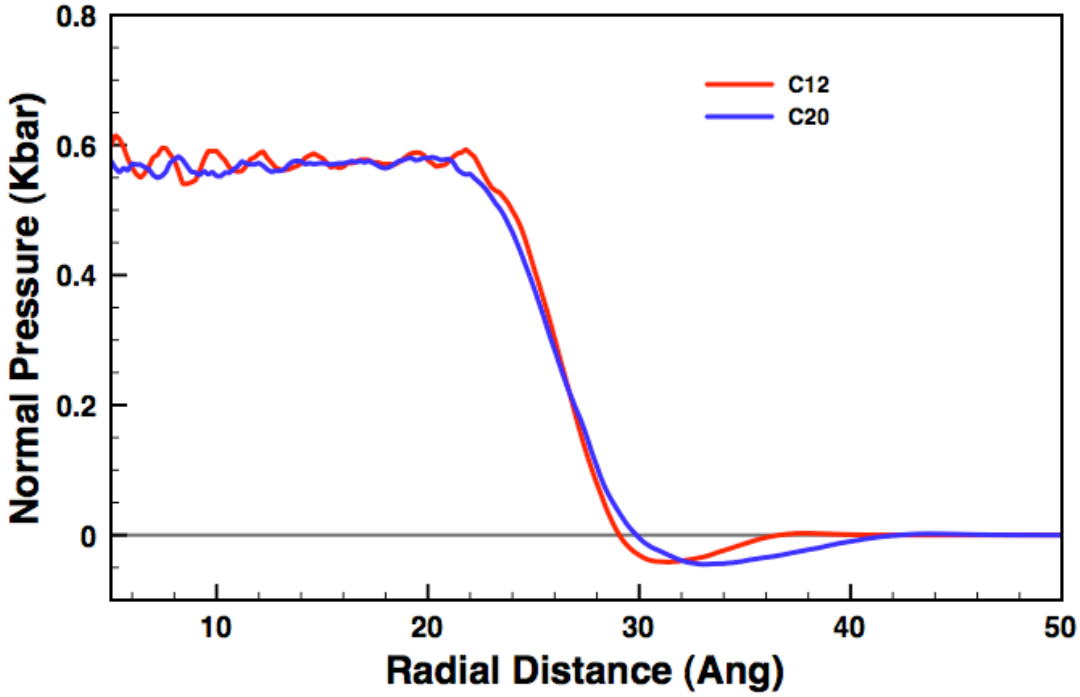

Figure 5.5: Normal pressure profiles of the C12 and C20 particles

The computed surface tension for the C20 particle is γ_i= 81.6 mJ/m^2 and the surface tension is γ_S=-8.5 mJ/m^2.

As discussed in Chapters 3 and 4, the effect of the negative surface tension is to reduce the equilibrium vapor pressure of the coated particle. The organic coated particle can process water despite its hydrophobic surface. The sticking coefficient calculations showed that for water monomers hitting the surface of the coated particle, one in every six collisions led to a stick, with the sticking water molecule penetrating the coating to get absorbed in the water core. The evaporation rate of water from the coated particle was also greatly reduced resulting in a net lowering of the equilibrium vapor pressure, although the magnitude of the lowering could not be computed because it was too low.

These organic coated particles are secondary aerosols formed as a result of sea sprays, where the surfactants coating the surface of the ocean originate from the decomposition of marine organisms, e.g. phytoplanktons. However, it is quite possible that subsequent to the initial droplet formation the particle that do not get fully coated can either evaporate water from the exposed water surface, or could alternatively process additional organic material from the atmosphere. To study this latter possibility, we placed a single surfactant molecule a distance of 6 nm from the center of the particle, and directed towards the particle with a speed corresponding to the most probable fatty acid molecule at the given temperature. To obtain reasonable statistics, 102 such cases were considered, and it was found that all such collisions resulted in the impinging surfactant molecule sticking to the surface of the particle. Figure 5.6 shows snapshots of a typical collision simulation. After hitting the surface of the particle, the fatty acid molecule is seen to penetrate the coating, and goes through a process of rearrangement till its polar head finally tethers to the polar water surface. It should be noted here that the C12 particle was not likely to be 100% coated to begin with. In summary then, our simulations show that partially coated organic aerosols can acquire a greater organic coverage through atmospheric surfactant molecules attaching to the surface.

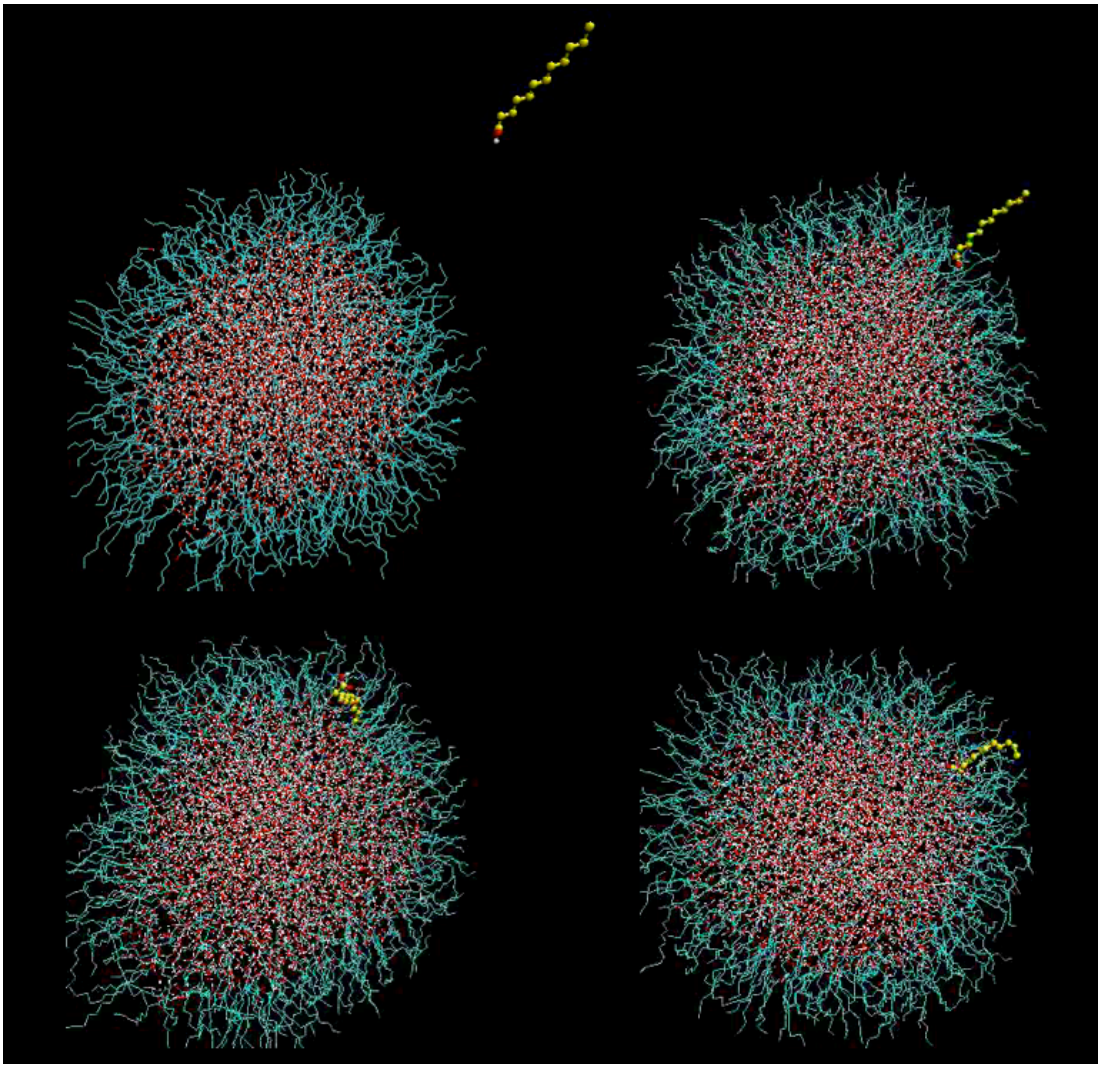

Figure 5.6: Snapshots of a surfactant molecule impinging on the C12 particle and attaching to the water substrate to become part of the inverse micelle

5.2.3 C28 fatty acid chains

To assess the role of chain length, eight hydrocarbon beads was added to each of the terminal beads of the surfactant molecules of the C20 particle to form the C28 particle. The first panel of Figure 5.7 shows a snapshot of the equilibrated C28 particle. Interestingly, whereas the C12 and C20 particles maintain their overall spherical shape, with the hydrocarbon chains directed radially outwards from the water surface, the C28 particle has an asymmetric structure where the hydrocarbon chains line up

parallel to each other in some regions forcing local flattening of the underlying water substrate (second panel of Figure 5.7).

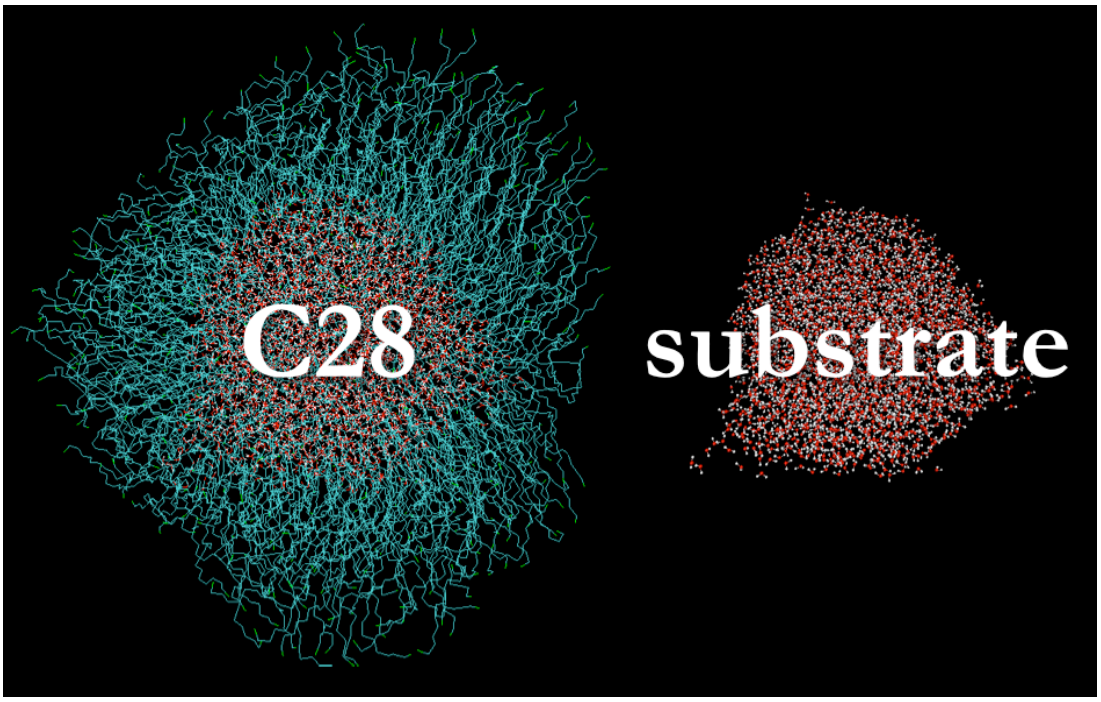

Figure 5.7: Equilibrated C28 particle along with the underlying water substrate

Figure 5.8 shows the radial distribution function (rdf) for the terminal bead of both the C12 and C28 particles. The peak for the C12 particle (where the chains are arranged radially outwards) occurs at a distance of around 4.75 $\mathring{A}$. If the chains of the C28 particle were similarly arranged (i.e. radially outwards), one would expect the peak for the C28 particle to shift further to the right (peak occurring at a greater distance). If we represent the C12 particle by a ball-stick model, as developed in our earlier work[1] (please see Figure 3.6), with the water droplet represented by a sphere of radius 25 $\mathring{A}$, and fatty acid molecules represented by a straight lines of length 12 $\mathring{A}$, polar head tethered to the surface of the sphere and the hydrocarbon chains radially

outwards, we see that the nearest neighbors of the terminal methyl group is at a distance of 1.5 δ, where δ is the equilibrium separation of the polar head groups on the surface of the particle. For δ=3.17 $\mathring{A}$ (to match with the peak of the C12 particle), the nearest neighbors of the terminal methyl group are at a distance of 4.75 $\mathring{A}$ (solid vertical line in Figure 5.8). Extending the model to represent the C28 particle (ball radius = 25 $\mathring{A}$, stick length = 28 $\mathring{A}$), the nearest neighbors would be expected at a distance of approximately 6.7 $\mathring{A}$ (dashed vertical line). However, the peak for the terminal methyl group of the C28 particle is found at around 4.25 $\mathring{A}$, indicating that some of the chains are closer to each other for the C28 particle. This is consistent with the earlier observation that the chains line up parallel to each other, and is a result of much stronger chain-chain interaction of the longer chains.

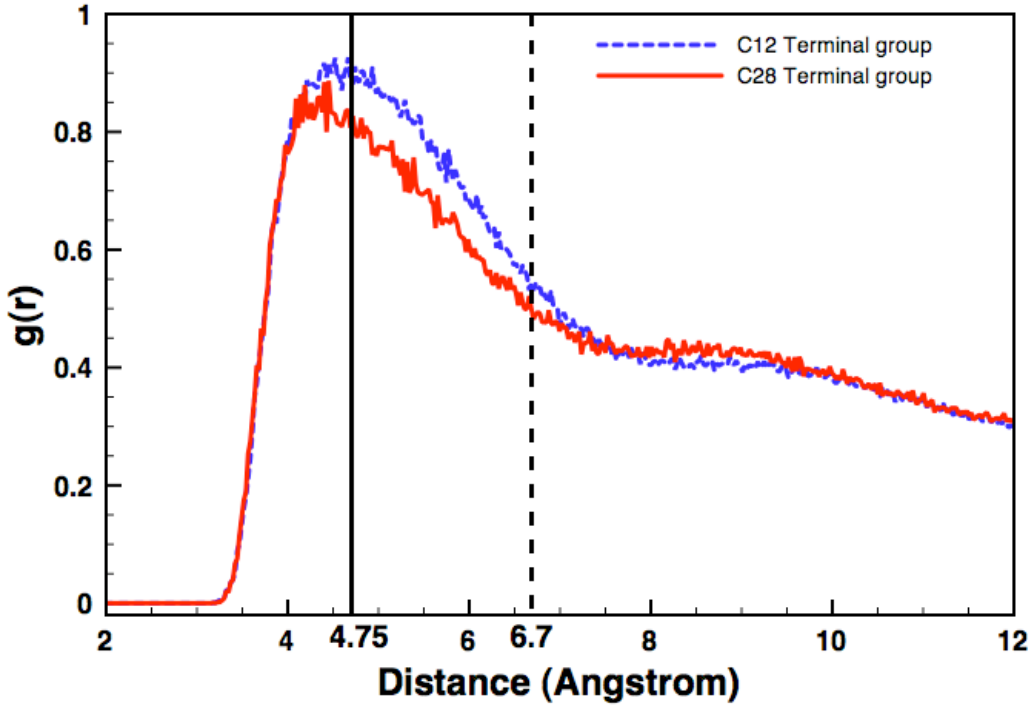

Figure 5.8: Radial distribution functions of the terminal methyl group of both the C12 and C28 chains

As has been widely reported in the literature, the natural tendency of surfactant molecules on a flat-water substrate is to orient themselves parallel to each other, separated by an equilibrium distance. However, for small particles, as in the case of the C12 particle, we get a minimum energy spherical water – surfactant interface, and the surfactant molecules arrange themselves radially outwards with the distance between the surfactant molecules increasing with increasing distance from the center of the particle. Even though the resulting energy of the coating is higher, the total energy of the particle is lower compared to a structure where chains are parallel with a locally flat interface. The interface, deformed from its minimum energy spherical shape, would result in an overall higher energy for the particle. For the C28 particle, however, there is a significant increase in chain-chain interaction. This increased attraction causes the surfactant molecules to orient themselves parallel to each other thereby lowering the energy of the coating. Even though the interfacial energy increases in the process, as evidenced by the expanded interface area, the resultant energy of the particle is lower than the case for the corresponding spherical structure.

5.3 Acid terminal group

Ellison et. al.[9] argued that the atmosphere would react with the organic coated inverted micelle and transform it. Atmospheric hydroxyl radicals trigger organic free radical reactions leading to the oxidation of the marine aerosol particles so that they get coated with, among others, acid functional groups. It is reasonable to expect that over time the hydrocarbon terminal groups would encounter oxidation reactions in the atmosphere. To study the effect of a hydrophilic terminal group on the structure of the

particle, and its water processing capability the terminal methyl group of the C12 particle was replaced with an acid group (-COOH) to form the C12-oxidized particle. Figure 5.9 shows a snapshot of the equilibrated C12-oxidized particle. The oxidized surfactant molecules seem to fold over at the surface (compare Figure 5.9 with Figure 5.2).

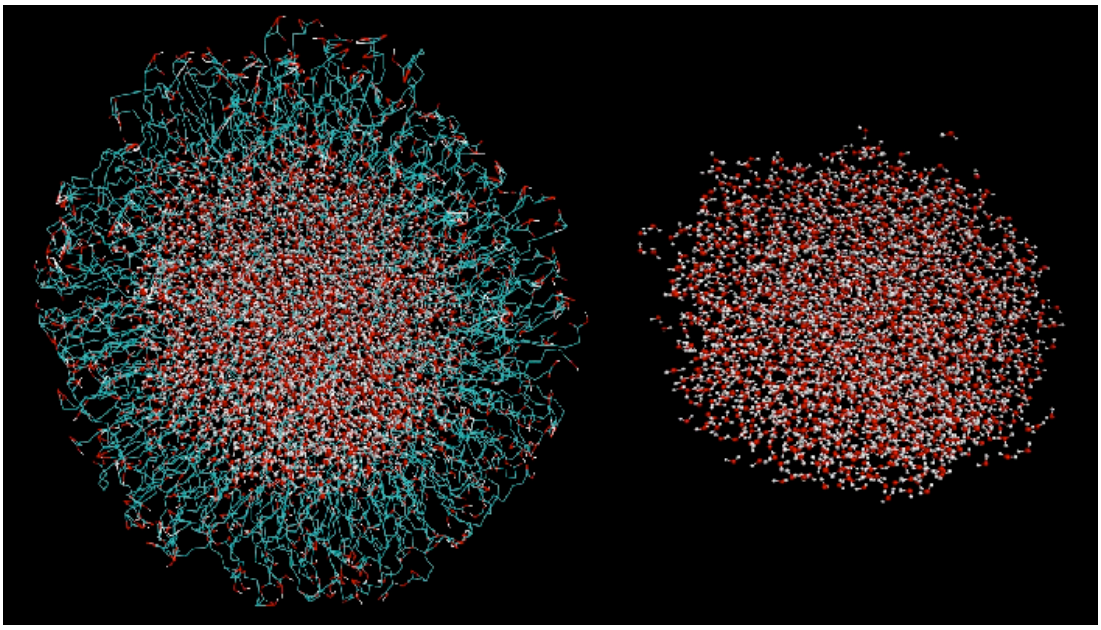

Figure 5.9: Snapshot of an equilibrated oxidized particle and the underlying substrate

5.3.1 Density and Pressure

Following equilibration, the density and normal pressure profiles of this oxidized particle was computed. Figure 5.10 plots the pressure profile.

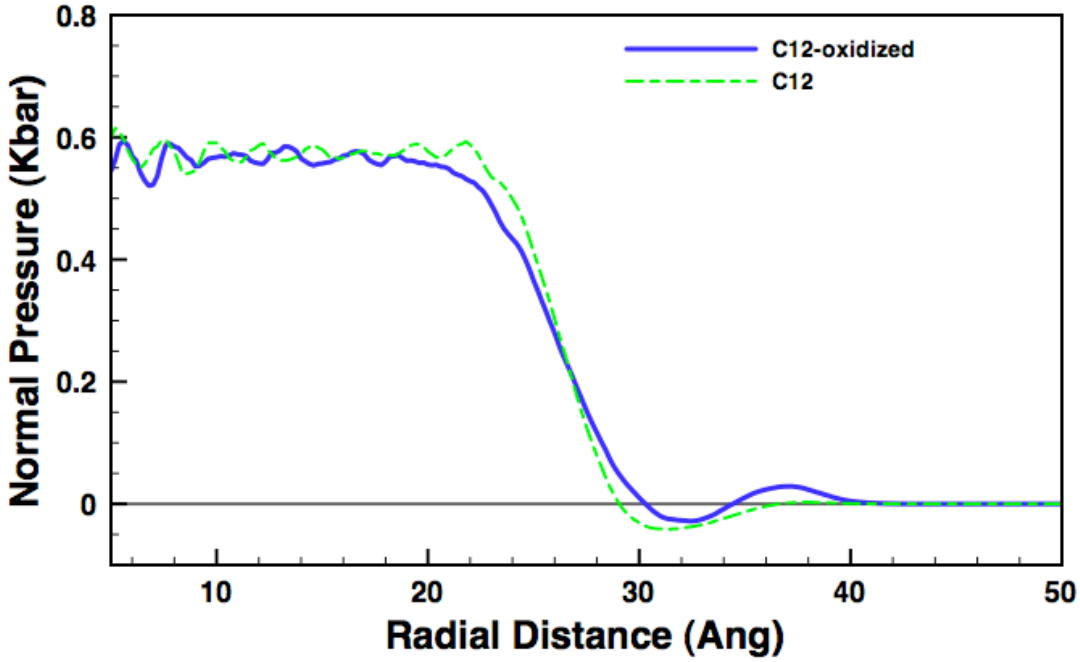

Figure 5.10: Normal pressure profile of the C12-oxidized particle. Also included is the pressure profile of the C12 particle

At and near the water-FA interface the differences between the oxidized and the C12 are negligible, and the coating in this region is under tension. However at the FA-gas interface, and in contrast to the C12, the pressure goes positive. This is the immediate effect of the acid terminal group. The polar terminal group at the surface of the particle folds resulting in an increase in density at the surface (and a compressive stress) as is evident from Figure 5.11, which plots the density profiles of the organic coating of both the C12 and the C12-oxidized particles. The increase in the density at the surface results in the positive normal pressure.

This increased density effect is most dramatically seen in the rdf of the carbon atom in the terminal acid group as compared with that of the C12 particle, shown in Figure 5.12. Clearly, the terminal group of the oxidized particle has more neighbors implying that the surfactant molecules do indeed fold over at the surface as argued.

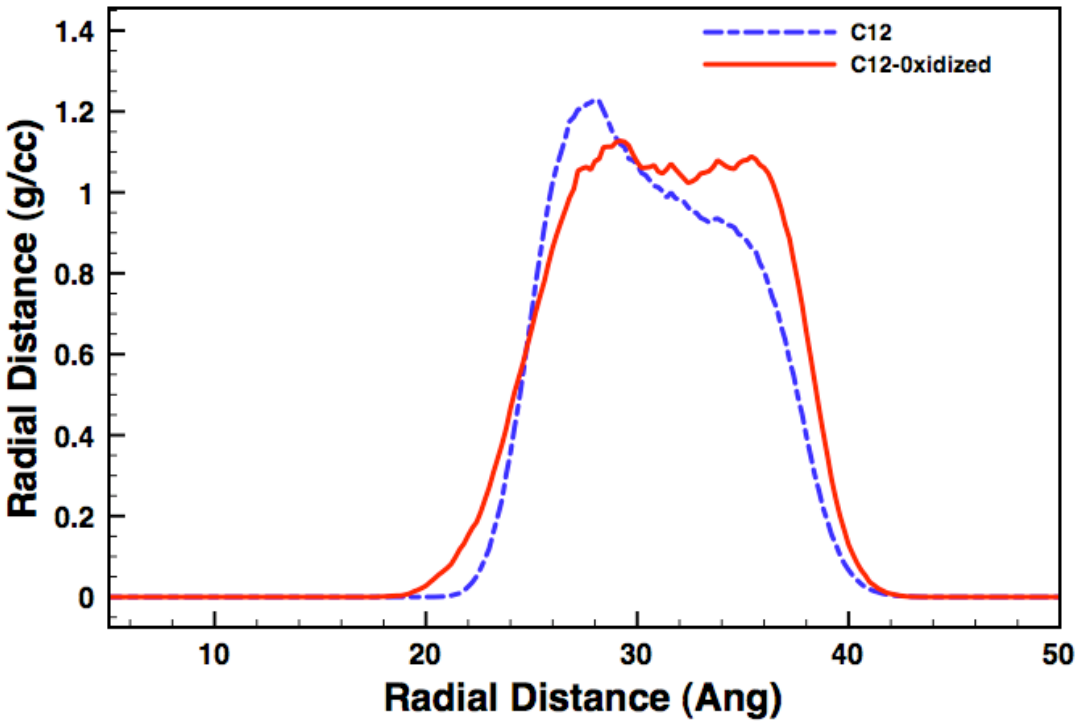

Figure 5.11: Density profiles of the organic coating of the C12 and C12-oxidized particles

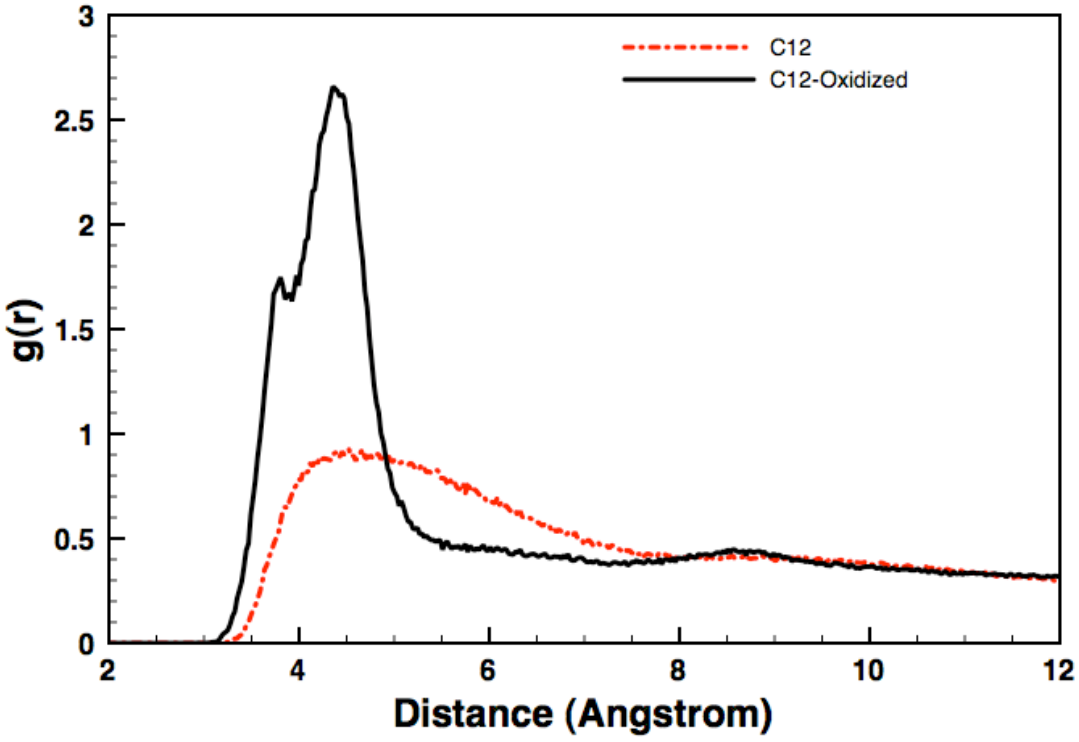

Figure 5.12: Comparison of the rdf's for the terminal group of the C12 and C12-oxidized particles

5.3.2 Sticking Coefficient of water vapor

To quantify water processing of these structures, we computed the sticking coefficient. The sticking (mass accommodation) coefficient or sticking probability, α, describes the probability of a gas molecule being incorporated into the liquid

$$\alpha = \frac{\text{number of molecules absorbed into liquid}}{\text{number of molecules impinging the liquid surface}} \tag{5.6}$$

The sticking coefficient calculations of water vapor on the C12-oxidized particle ware carried out as described earlier. For a given incident speed, 102 separate trajectories were considered by randomly placing the water monomer along the sphere of radius 6 nm. All the trajectories were monitored for 50 ps at the end of which an incident monomer was considered to be trapped on the particle if its distance from the center

of the particle was less than 5 nm. Otherwise it was considered to be an unreactive event. The sticking coefficient was then computed as the ratio of the number of monomers trapped on the oxidized particle to the number impinging on the surface (102 in the present case). Since, we had found in our prior work that the sticking coefficient to be essentially a constant (within 5%) for incident speeds around the most probable speed[2], the sticking coefficient calculations were carried out for just the most probable speed case. The result was that the sticking coefficient, α, was found to be 0.50 for the oxidized particle i.e. one in every two collisions led to a stick. This increase in sticking probability (from one in six-seven collision for the C12 particle) can be attributed to the more water-like polar surface of the oxidized particle as opposed to the hydrophobic surface of the C12 particle. For the trapped cases, the average distance of the monomer (average taken over all the trapped cases) from the center of the particle was computed as a function of time, and is plotted in Figure 5.13. The trapped monomers do not penetrate the coating in sharp contrast to the trapped case for the C12 particle (see Figure 4.7). Instead they stick to the largely polar surface since they do not feel the presence of the polar core beyond the coating. An important point here is that in the context of the prior observation that "oily" surfaces (with negative surface tension) are water processors, which enable the water to penetrate to the core (underlying water droplet), these structures would simply have the usual vapor pressure relationships which may mimic the more traditional two component mixed organic-water systems usually addressed by a Kohler analysis more typically found for a water droplet.

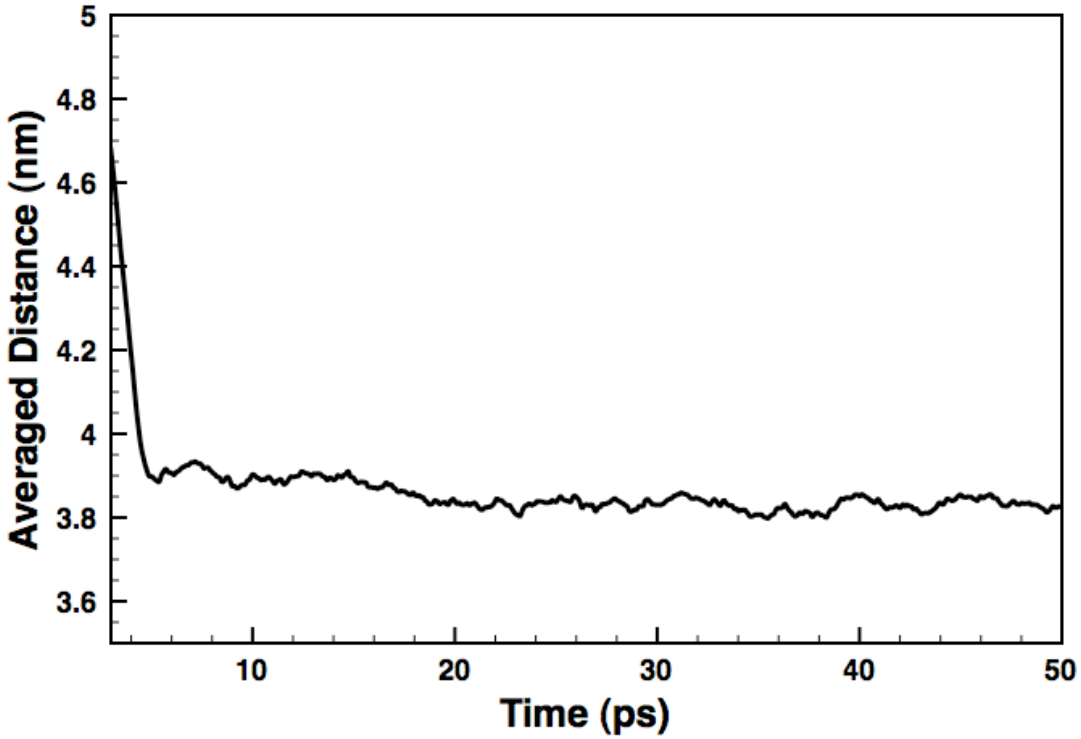

Figure 5.13: Plot of the average distance of the incident monomer (averaged over all the 'Trapped' trajectories) from the center of the particle as a function of time (ADD C12)

5.4 Branched surfactant coating

Next, to study the effect of branched surfactant coating, the water droplet was coated with Phytanic acid. As before, 505 Phytanic acid molecules were attached to the surface water molecules. After a short energy minimization step, the particle was allowed to equilibrate. During the process of equilibration, three phytanic acid molecules were released from the water surface. Such surfactant molecules were removed from the system and the particle was equilibrated for 100 ps. Figure 5.14 gives a snapshot of the equilibrated particle and its water substrate.

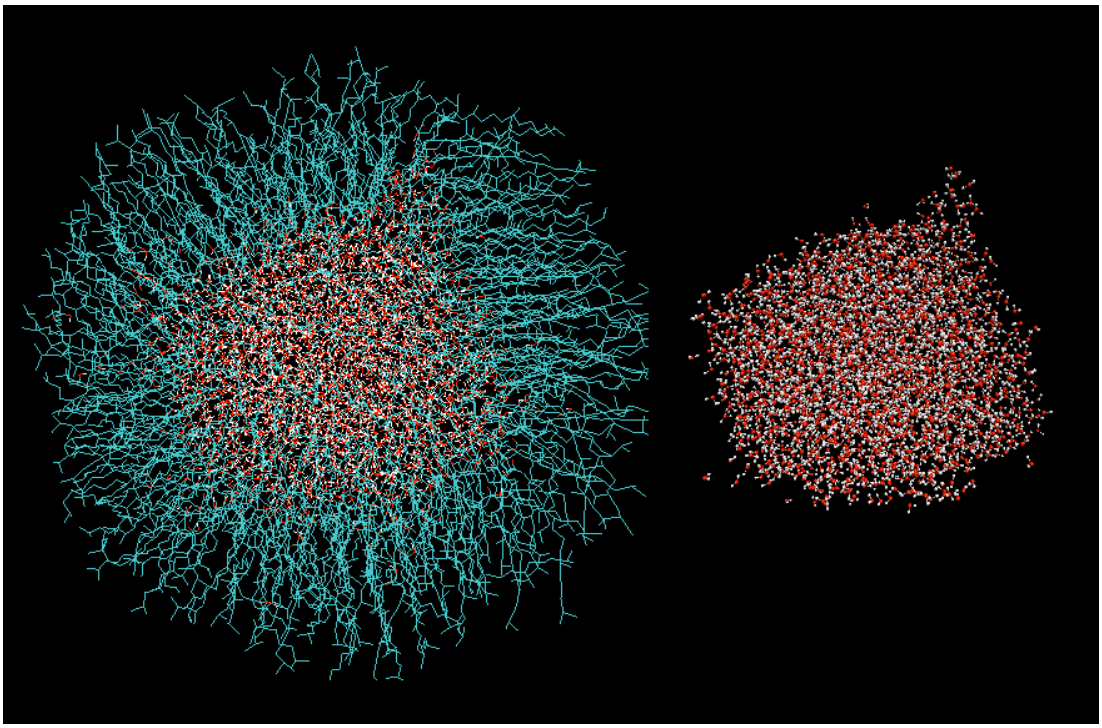

Figure 5.14: Snapshot of an equilibrated water droplet coated with Phytanic Acid and the underlying water substrate

In this case, due to the increased chain-chain interaction, significant regions were found where the surfactant molecules lined up parallel to each other, thus forcing the deformation (flattening) of the water-interface. In the upper right hand corner of the water core, we see that the water interface is significantly distorted in order to accommodate the change in orientation of the chains. Due to the lack of symmetry, pressure and surface tension calculations were not possible. Sticking coefficient trajectories for water vapor on this particle indicated that only 3 out of 102 collisions resulted in a stick. In fact, for the case of the three 'trapped' monomers, it was seen that they stay on the surface of the particle, instead of diffusing through the chains and getting absorbed into the water core as was seen for water monomers hitting the C12 particle. These three simulations were restarted and continued for another 100 ps. The incident monomers continued to stay on the surface and did not penetrate the

coating. *This is in sharp contrast to the case of the C12 particle where trapped monomers penetrated the coating and were absorbed into the water core*. For the C12 particle, the chains remained arranged radially outwards (distance between the chains increase with increasing distance from the water – organic interface). Most of the chains in the present case being parallel to each other, there was no gap for the water monomer to penetrate the coating. *Thus, the particles with parallel chains (the case of longer chains and branched surfactants) would behave as if the surface is "oily" as opposed to the ones with shorter chains that can process water despite their apparent hydrophobic surface*.

6 Stokes Drag on Functionalized Nanoparticles

6.1 Introduction

The current work is motivated by a recent experimental study[25], which characterized the thickness of monolayers functionalized on nanoparticles using ion-mobility spectrometry. The measurement relied on the determination the size of a charged particle through knowledge of the drag force. In that work functionalized Au-NPs were studied using electrospray-differential mobility analysis (ES-DMA). Commercially available monodisperse Au colloids (10nm, 20nm, 30nm and 60nm) were functionalized with11-mercaptoundecanoic acid (99+ %, MUA). It was observed that for the MUA coated Au-NPs, the size distribution indeed shifted to larger sizes. The presence of SAM conjugation on the Au-NPs was thus detected based on the difference in the electrical mobility between conjugated and bare Au-NPs. The change in particle size was defined as $\Delta L = d_p - d_{p0}$, where d_p and d_{p0} represented the coated and uncoated particle mobility diameters, respectively. A simple core-shell model for the change in particle size gives $\Delta L_1 = 2l\cos(\theta_{SAM})$[6], where l is the length of the alkanethiol molecule, and θ_{SAM} is the typical average tilt angle, ~30^0. This model predicts a length of ΔL_1=2.72nm for the MUA whereas from the experiment ΔL_1 was found to be ~2.0nm for a 30nm MUA coated Au-NP (Figure 6.1a).

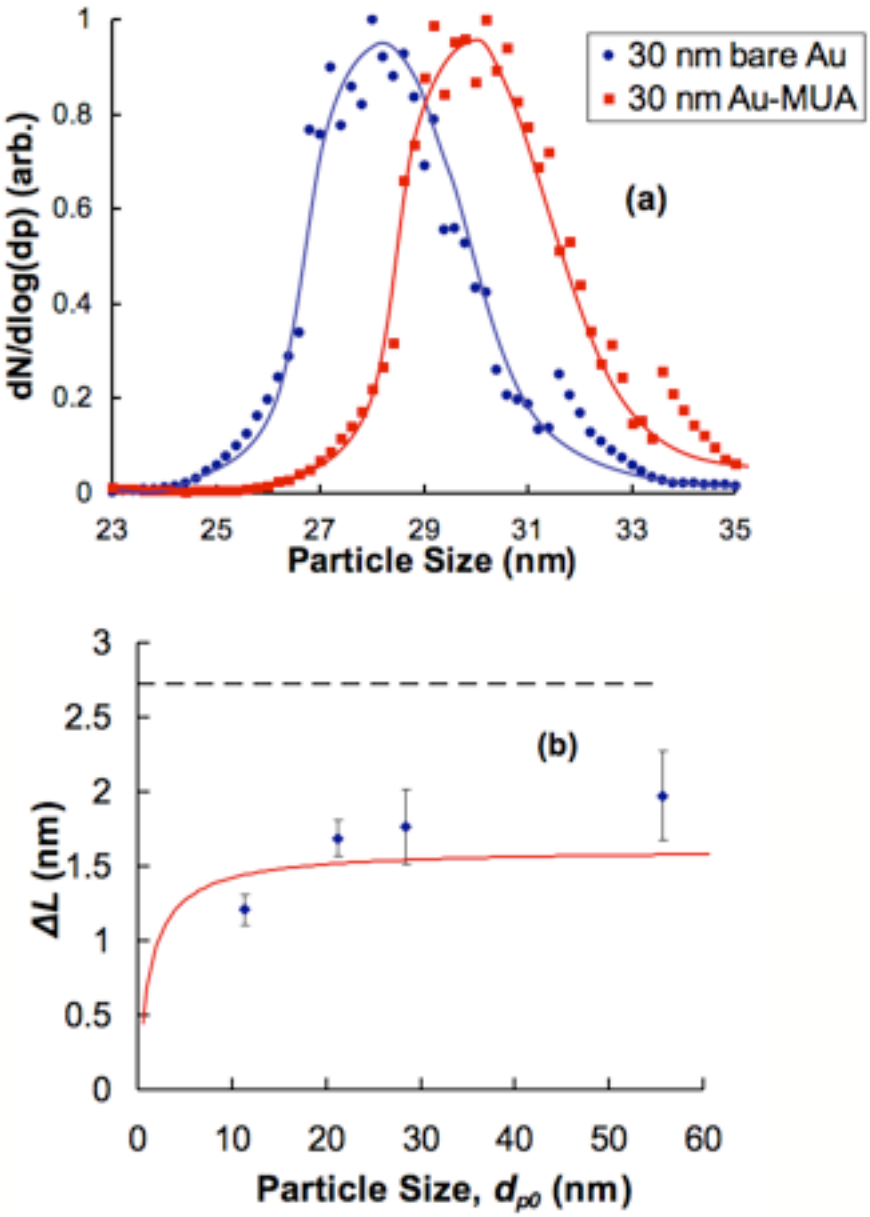

Figure 6.1: (a) Particle size distributions of bare Vs MUA-coated Au-NP for 60nm particles. (b) Comparison of ΔL predicted from experiment (diamonds) with theory - ΔL_1 as dashed line, ΔL_2 as solid line. (Both the figures have been taken from Ref. 6)

The experimental value was thus ~35% lower than the predicted value, indicating that a SAM-coated Au-NP has a **lower drag** than other rigid (e.g. metal or metal oxides) core-shell particles. The most obvious reason would be that the SAM

coating is not really a dense material. As such the surface can be thought of as somewhat porous. To account for this, an adjustable parameter α was introduced to incorporate the effect of SAM spacing in the calculation. The modified mobility diameter then becomes $\Delta L_2 = \alpha \Delta L_1$, where $\alpha = A_2 / A_1$ with A_1 being the projected area of a rigid solid shell and A_2 being the effective projected area of SAM. Figure 6.1b compares ΔL from experiment (diamonds) with theory (ΔL_1 as dashed line and ΔL_2 as solid line). Figure 6.1 has been reproduced here from Ref. 1.

In this chapter, we report the result of the study to determine the effect of SAM coating on the Stokes drag of a particle, through a fundamental molecular dynamics simulation of the gas-particle interactions and show that indeed the drag on a coated particle is less than the drag on the corresponding pure particle, consistent with the previously mentioned experimental observation.

6.2 Methodology

The starting point for any phenomenological description of drag on a sphere comes from Stokes law[59]. Stokes had, in 1851, found that the force F acting on a sphere of radius b moving slowly with constant velocity U through an unbounded fluid of viscosity μ is given by

$$F = 6\pi\mu b U . \tag{6.1}$$

For a sphere moving through a semi-infinite fluid, bounded on one side by a solid surface was derived by Brenner[60] who showed that for a sphere moving perpendicular to a solid surface

$$F = 6\pi\mu b U \lambda , \tag{6.2}$$

where

$$\lambda = \frac{4}{3}\sinh\alpha \sum_{n=1}^{\infty} \frac{n(n+1)}{(2n-1)(2n+3)} \times \left[\frac{2\sinh(2n+1)\alpha + (2n+1)\sinh 2\alpha}{4\sinh^2(n+1/2)\alpha - (2n+1)^2 \sinh^2 \alpha} - 1 \right],$$

$$\alpha = \cosh^{-1}\varepsilon = \ln\left(\varepsilon + \left[\varepsilon^2 - 1\right]^{1/2}\right),\ \varepsilon = \frac{h}{b} + 1$$

with h being the minimal distance between the ball and the solid surface. In the limit $\frac{h}{b} \to 0$ this expression reduces to $F = 6\pi\mu U b^2 / h$

i.e., the force diverges when the sphere gets close to the solid surface. This result, which is obviously inconsistent with our everyday experience, arises from several assumptions made in the analysis:

- no-slip boundary conditions are valid
- the fluid density remains constant even as the ball approaches the solid wall and
- both solid surfaces (of the ball and the wall) are assumed to be perfectly smooth.

While Stokes law has been know for more than one and a half century, only recently Alder et. al.[61] demonstrated the validity of Stokes law from a molecular perspective for a bulk system of hard spheres.

Vergeles et. al.[62, 63] studied the translational motion of a sphere (with and without inner molecular structure) through a viscous Lennard-Jones liquid using Molecular Dynamics (MD) simulations. Good agreement between the computed and actual radii was found for different velocities and sphere sizes. The sphere was translated through a stationary fluid and the drag on the sphere was computed by summing up the forces

on the sphere atoms along the direction of motion. Given the drag force, the effective radius of the sphere was calculated using Eqn 6.1. Subsequent to computing the drag on the pure particle, the pure particle was replaced by a coated particle of the same total size (i.e. smaller core). A series of simulations were carried out with varying particle radii and it was found that indeed the drag on a coated particle is less than the drag on the corresponding pure particle, consistent with the experimental observation.

6.3 Molecular Dynamics Simulation

The MD model, simulation details, drag and 'effective radius' computations are explained for the case of a spherical particle of radius 6σ. The interaction between the fluid atoms was defined via a pairwise Lennard-Jones potential

$$V(r) = 4\varepsilon\left[\left(\frac{\sigma}{r}\right)^{12} - \left(\frac{\sigma}{r}\right)^{6}\right] \tag{6.2}$$

Most of the parameters used in Ref 62, 63 have been used in this work except the simulation box size when necessary. As in Ref 62 non-dimensional LJ units were used throughout. Length, temperature and mass were non-dimensionalised with $\sigma = 3.4\,\text{Å}$, $\varepsilon/k_B = 120\ \text{K}$, and molecular mass $m = 40$ a.m.u. The natural time unit was then given by $\tau = \sigma\sqrt{(m/\varepsilon)} = 2.16\times10^{-12}\text{sec}$.

A simulation box of dimensions $72\sigma \times 36\sigma \times 36\sigma$ was considered. This was found to the optimal dimension to correctly reproduce the drag data on a pure particle of radius 6σ. Fixed boundaries with reflecting walls were imposed on the system in the *y* and *z* directions whereas periodic boundary condition was imposed in the *x*-direction. Approximately 72,000 fluid atoms were then assigned as points of an FCC

lattice that completely filled the box. The non-dimensional density of 0.8 m/σ^3 is identical to Ref. 5. The Lennard-Jones potential parameters, $\varepsilon = 1$ and $\sigma = 1$, were used to define the fluid-fluid interaction with the potential cut-off at 2.5σ with the potential shifted at the cut-off to 0. A cavity was created for the placement of the sphere by deleting fluid atoms inside of a radius of 6.5σ centered at (10,18,18). The pure ball was formed from a separate FCC lattice with a density of 1.8 m/σ^3 and extracting the atoms inside a radius of 6σ (the surface atoms are at a distance of 6σ from the center of the spherical ball) consisting of 1631 atoms. Figure 5.2 shows an initial setup.

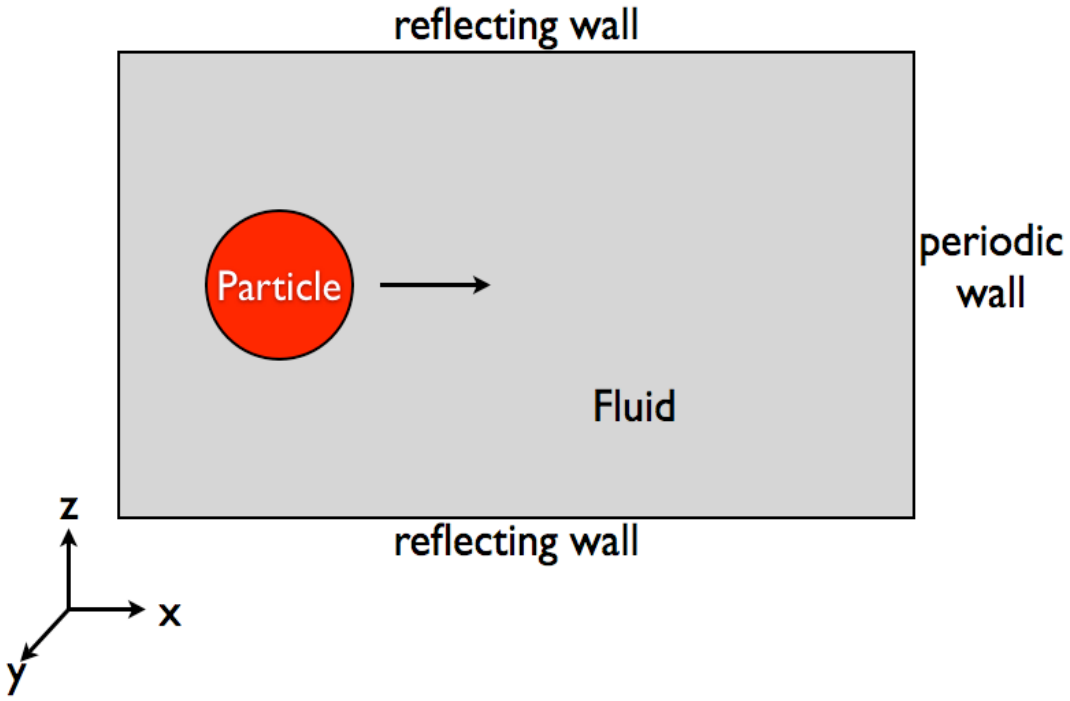

Figure 6.2: Schematic of the simulation setup.

Atoms of the ball were not allowed to interact with each other but interacted with the fluid atoms via the LJ 12-6 potential using the same potential parameters as those of the fluid – fluid interaction. These atoms were given a very high mass of 1.8×10^{6}m to maintain the rigidity of the ball.

The system was then equilibrated maintaining a temperature of $T=1.2\ \varepsilon/k_B$. This temperature gave the fluid atoms sufficient kinetic energy to break the attractive bonds of the LJ potential. The system was equilibrated for a total time of 50τ. At the end of the equilibration period the system reaches an equilibrium state.

For the drag evaluation the sphere was then translated through a stationary fluid and the drag on the sphere was computed. Given the drag force, the effective radius of the sphere was calculated using Eqn 6.1. The spherical pure particle was given an initial velocity of $2.0\ \sigma/\tau$ and allowed to move across the simulation box for a total time of 35τ. During this time, the sphere traveled a distance of 70σ, and hence the *x*-dimension of the simulation box. Because of the particle's large mass, the velocity (and hence the momentum) of the sphere was nearly constant throughout the simulation despite the drag force acting against its motion. Nonetheless, some momentum was still deposited into the fluid by the sphere. A velocity-rescaling thermostat adjusted the kinetic energy of the fluid so that a constant temperature was maintained.

In an MD simulation, computing the instantaneous drag on a particle is straightforward, since the forces on each atom is known at every time step. The net instantaneous drag force is the component of the force, parallel to the direction of mo-

tion of the particle, summed over all atoms of the particle. Using a time step of 0.0005τ, forces on each of the atoms of the particle were obtained at every time step. Averaging over 500 data points, the mean drag force was sampled every 0.25τ. Figure 6.3 is a plot of the mean drag force as a function of time.

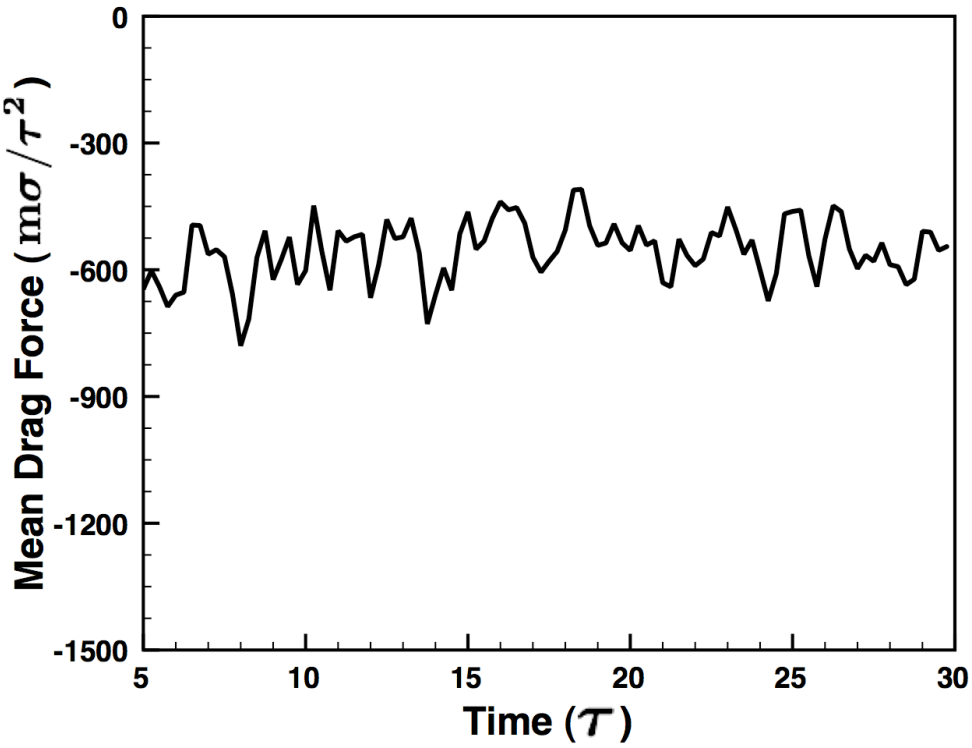

Figure 6.3: Mean drag force acting on a pure spherical particle of radius 6σ plotted as a function of time.

Averaging between the times 15τ and 25τ, a drag force of 542 $m\sigma/\tau^2$ was obtained. The viscosity of the Lennard-Jones fluid under our conditions ($T=1.2, \rho=0.8$) has previously been determined[64] to be $\mu=1.94\pm0.16$ and is used in this work. Then applying Stokes law, and using the values $F=542$ and $U=2.0$ we obtained $b=7.4\sigma$. This agrees well with the definition of b as r_0+1 (where r_0=4σ,

the actual radius of the ball). This definition comes from the observation that the effective radius of a particle in a solvent is the radius of the sphere inaccessible to the solvent particles. Since the effective radius of the Lennard-Jones interaction is approximately one, the effective radius of the pure particle should be r_0+1.

With the Stokes law being reproduced for the case of a spherical particle, we next computed the effective radius of organic coated particle. The organic coated particle consists of a pure core with polymer chains attached. Figure 6.4 shows a typical polymer chain. It consists of a head group (that binds to the pure ball – substrate) and one or more hydrocarbon beads.

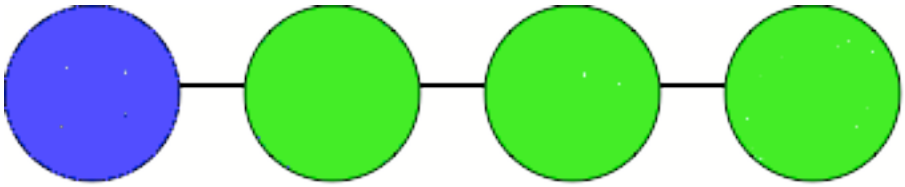

Figure 6.4: A typical polymer chain. The blue bead represents the head group (binds to the surface of the pure ball) and the green beads represent the hydrocarbon tail.

A fixed distance of 0.75σ separates the adjacent beads. The chains do not interact with each other, nor do they interact with the pure core. The only interaction is between chains and the fluid atoms. They are given a very large mass (equal to that of the pure ball molecules) so that the coated structure is rigid. The head group – fluid interaction is the same as fluid – fluid interaction. The tail group – fluid interaction is modelled using the repulsive part of the Lennard-Jones potential with the very same

parameters. The coated particle was constructed as follows: a pure spherical particle of radius 3.3σ was taken and its surface molecules were identified. To this surface molecule the head group of a polymer chain (1 Head group and 2 Tail groups) was attached (at the equilibrium distance of 1.12σ) with the green beads placed radially outwards resulting in a coated particle of radius $\sim 6\sigma$. This coated particle was then placed in the spherical cavity and the system equilibrated for 50τ at the end of which the system reaches a stable equilibrium state.

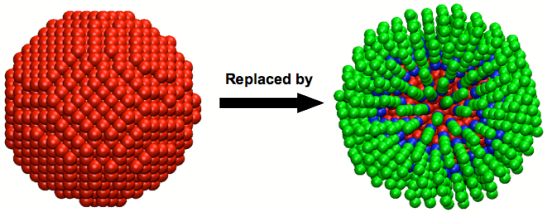

Figure 6.5: Pure particle is replaced by a coated particle of the same size (i.e. smaller core).

Next, as with the pure particle, the coated particle was given a velocity of 2.0 σ/τ in the x-direction and the drag force was sampled.

6.4 Results: Comparison of the 'effective radii' of pure and coated particles

Three different particle sizes, 3.37σ, 6σ and 8σ were considered. For each particle size, first a bare particle of that radius was constructed. For the coated particle, we maintained the overall radius of the particle such that

1. the total actual radius of the coated particle is the same as that of the corresponding pure particle and
2. the radius of the core is roughly double the length of the surfactant molecule.

The effective radii (through drag computation) of both the pure and the coated particles were computed. Table 6.1 details the results of the simulations and Figure 6.6 plots the effective radii of the particles versus their actual radii.

Table 6.1: Drag simulation results. For a coated particle, the number within parentheses represents the radius of the pure core.

Particle Radius (σ)	Pure/Coated	Drag Force ($m\sigma/\tau^2$)	Effective Radius (σ)
3.4	Pure Coated (1.5σ)	326 220	4.4 3
6	Pure Coated (3.3σ)	542 428	7.4 5.9
8	Pure Coated (4.4σ)	679 582	9.3 8

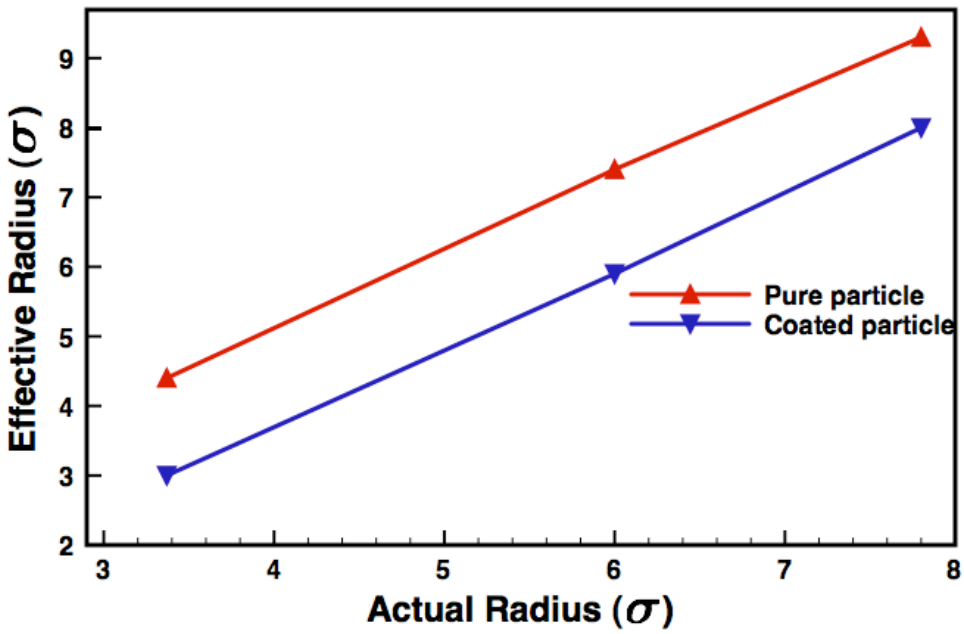

Figure 6.6: Effective Radii Vs Actual Radii of the three particles. The Red triangles represent the effective radii of the pure particles whereas the Blue triangles

represent the effective radii of the coated particles. Clearly, the coating reduces the drag on the particles.

It is evident from the plot that the coating reduces the effective radii of the particles i.e. the drag on the particles is reduced due to the coating. A possible reason for this might be that the fluid molecules can actually pass through the chains without colliding with either the chains or the core. To test the validity of this reasoning, we took the 6σ particle and reduced the size of the fluid molecules to 10% of the original value with the hope that if our reasoning is indeed correct, the drag on the coated particle is going to be reduced further. The potential parameter σ of the polymer – fluid interaction was reduced from to 10% keeping all other interaction parameters fixed. Not surprisingly, the effective radius of the particle reduced to 3.9σ from 5.9σ substantiating the claim that the drag on the coated particles is reduced because the fluid molecules can actually pass through the chains without colliding with either the chains or the core.

7 Conclusion and Future Work

7.1 Conclusion

The goal of this research was to study the structure and properties of organic coated nano aerosols; a good understanding of which is important as they may significantly affect the processing of water vapor in the atmosphere and the radiation balance to the earth. Molecular Dynamics simulation method was used for the study.

In the first part of this work, chapter 3, a coarse-grained model was used. It was found that these coated structures do indeed prefer an inverted micelle structure. The water – fatty acid interface maintains its minimum energy spherical shape with the hydrocarbon chains directed radially outwards from this interface. The coating was found to be under tension as evident from the negative normal pressure profile. Using a simple geometric ball-stick model, we showed that this negative pressure was a manifestation of the curved interface. Consequently the particle behaves as if its surface tension is negative resulting in an inverse Kelvin vapor pressure effect. As a result, such a particle can process water vapor despite its apparent hydrophobic surface and are *net water attractors*. If such structures are made in sufficient concentration, they might be important contributors in the cloud condensation process.

Next, an effort was undertaken to quantify water vapor processing by these particles (chapter 4). An atomistic/united atom setup was used for all subsequent works. It was found that the rate of water uptake (sticking coefficient) by the coated droplets is about a sixth of that by pure water droplets. This reduction of sticking coefficient

might seem to imply that the equilibrium vapor pressure on such particles is higher, but we also need to take into account rate of evaporation of water from the coated drops. Both the pure and coated drops were heated using an identical temperature ramp and the root mean square deviation (RMSD) of water molecules was computed as a function of time. While the RMSD for both particles increased over time, there was a clear bifurcation where the water droplet RMSD exceeded that of the coated droplet implying that the evaporation rate was also significantly reduced. An attempt was made to compute the equilibrium vapor pressure of water. It was observed that the equilibrium vapor pressure was too small to measure and thus considerably lower than that of a small bare water droplet.

Following this, we studied the effect of fatty acid chain length, chain branching and terminal group oxidation on the morphology and water processing properties (Chapter 5). It was found that droplets coated with fatty acids with smaller chains (12 Carbon atoms) maintained their overall spherical shape and the fatty acid chains were arranged radially outwards from the spherical interface. The interfacial energy was the dominant force in this case. For the case of longer chains (28 Carbon atoms) and branched molecules (phytanic acid), however, the particles underwent significant deformation. The much stronger chain – chain interaction was able to overcome the high interfacial energy resulting in parallel chains and locally flattened interface. With the chains parallel to each other, the particle should behave like an oily surface instead of a water attractor as seen earlier. The sticking coefficient calculations asserted this conclusion. Only 3 out of 102 incident water monomers were seen to ‘stick’ to the surface of the particle. In fact, the three trapped monomers stayed on the

surface instead of diffusing through the coating and getting absorbed into the water core of the particle, as was the case with smaller chains.

Thus, if the interface energy dominates, the structure of the inverted micelle would be spherical leading to a negative pressure and surface tension and result in a significant increase in water processing capabilities. On the other hand, if the chain-chain interactions are strong the chains will align parallel to each other and the particle as such would act as an oily droplet.

Finally, in Chapter 6, the effect of organic coating on the Stokes drag of nanoparticles was studied. This work was motivated by a recent experimental study, which reported that the drag on gold nanoparticles coated with self-assembled monolayers (SAM) is considerably lower than the drag on a corresponding pure gold nanoparticle. To study the effect on drag, a pure particle was translated through a viscous stationary Lennard-Jones liquid and the drag on the sphere was computed by summing the forces on the ball atoms in the direction of motion. The simulation box dimensions were selected such that there was good agreement between the actual and effective radii. The pure ball was then replaced by a coated particle of the same overall size. We carried out a series of simulations with varying particle radii and found that the drag on the coated particle was indeed less than that on the corresponding pure particle since the liquid molecules can pass through the coating without colliding with either the chains or the particle core.

7.2 Future Work

It is clear that the organic coating on water droplets would have a significant effect on their CCN properties and their role in atmospheric chemistry. The work sum-

marized in this thesis can be extended to better understand organic aerosols and functionalized nanoparticles. For example, one can study the role of salt inside the coated droplet on the structure and properties of these organic aerosols. The effect of the sulfuric acid on the structure of the coated particles poses another interesting problem. One can also study particles coated with multiple organic species. In our work, we investigated the rate of water uptake by the organic aerosols. There has been considerable interest in the rate of uptake of bigger molecules, e.g. N_2O_5. In some recent works[65, 66], a significant suppression of N_2O_5 uptake by a monolayer of oleic acid was found despite the fact that it long chain length (C18) is bent and hence does not pack tightly on the surface and therefore should behave more like lauric acid (C12) coating. These are some very interesting and open problems.

As mentioned in Chapter 6, the work on computing the Stokes drag on SAM coated nanoparticles was motivated by a recent experimental work. While the experiment deals with the drag of gas on the particle, we chose to compute the drag of a liquid on the particle since it was more feasible to do so. While conducting the simulations, we were faced with two major problems. The first problem relates to the particle size. For the experimental study, the nanoparticles used ranged from 10 nm to 60 nm in diameter. The largest particle used for the computer experiment was 5.5 nm in diameter and required a large simulation box with approximately half a million fluid atoms to correctly reproduce Stokes drag for a pure particle. An 8 nm particle would require ~ 4 million fluid atoms. As figure 6.1 suggests, one would need a particle size greater than 20 nm for accurate comparison with experimental data. This was not possible with the computer resources available. The second issue was that we computed

the drag of a liquid on the particle as opposed to a gas as is done in the experiment. For the simulation, however, the use of gas was not feasible, since due to such low density, most of the gas molecules would never collide with the particle producing drag data. One possible workaround can be to devise a systematic way, to shoot gas molecules at the particle and compute the drag on the particle from the change in momentum of the gas molecules. But that would require monitoring a really large number of trajectories, much more than that were required for the sticking coefficient calculations. A feasible method to compute the drag of gas on the particle needs to be formulated.

8 Appendix

Sample Lammps input file to equilibrate a water droplet coated with fatty acid.

```
# Equilibrating a water droplet consisting of 2440 H2O molecules and 505
#  Dodecanoic Acid molecules
units                   real
dimension               3
newton                  on
processors              2 2 2
boundary                s s s
neighbor                2.0 bin
neigh_modify            page 20000000
atom_style              full

pair_style              lj/cut/coul/cut 56.0
pair_modify             mix arithmetic
bond_style              harmonic
angle_style             harmonic
dihedral_style          charmm
improper_style          harmonic

read_data               water2440fac12_505.data

## ATOM TYPES
# Water
# 1     OW
# 2     HW1
# 3     HW2
# FA-C12
# 4     HO
# 5     OA
# 6     C
# 7     O
# 8     CH2
# 9     CH2
# 10    CH2
# 11    CH2
# 12    CH2
# 13    CH2
# 14    CH2
# 15    CH2
# 16    CH2
# 17    CH2
# 18    CH3
```

```
# Masses
mass    1       15.9994
mass    2        1.0080
mass    3        1.0080
mass    4        1.0080
mass    5       15.9994
mass    6       12.0110
mass    7       15.9994
mass    8       14.0270
mass    9       14.0270
mass   10       14.0270
mass   11       14.0270
mass   12       14.0270
mass   13       14.0270
mass   14       14.0270
mass   15       14.0270
mass   16       14.0270
mass   17       14.0270
mass   18       15.0350

# Pairwise potential parameters
pair_coeff      1       1       0.1553          3.166
pair_coeff      2       2       0.0             0.0
pair_coeff      3       3       0.0             0.0
pair_coeff      4       4       0.0             0.0
pair_coeff      5       5       0.2029          2.955
pair_coeff      6       6       0.0970          3.361
pair_coeff      7       7       0.4122          2.6260
pair_coeff      8       8       0.1400          3.9647
pair_coeff      9       9       0.1400          3.9647
pair_coeff      10      10      0.1400          3.9647
pair_coeff      11      11      0.1400          3.9647
pair_coeff      12      12      0.1400          3.9647
pair_coeff      13      13      0.1400          3.9647
pair_coeff      14      14      0.1400          3.9647
pair_coeff      15      15      0.1400          3.9647
pair_coeff      16      16      0.1400          3.9647
pair_coeff      17      17      0.1400          3.9647
pair_coeff      18      18      0.1800          3.7862


## BONDS (bond_type         description     parameters)
# 1      OW-HW1; OW-HW2 (1A, kept fixed using SHAKE)
# 2      HO-OA (1 A;    375 KCal/mol/A^2)
# 3      OA-C  (1.36 A; 450 KCal/mol/A^2)
# 4      C=O   (1.23 A; 600 KCal/mol/A^2)
```

```
# 5      C-CH2; CH2-CH2; CH2-CH3
#              (1.53 A; 400 KCal/mol/A^2)
#
# Bond potential parameters
bond_coeff     1            0.0   1.0
bond_coeff     2          375.0   1.0
bond_coeff     3          450.0   1.36
bond_coeff     4          600.0   1.23
bond_coeff     5          400.0   1.53


## ANGLES (angle_type       description      parameters)
# 1      HW1-OW-HW2 (109.47, kept fixed using SHAKE)
# 2      HO-OA-C          (109.5, 47.5 KCal/mol/rad^2)
# 3      OA-C=O           (124.0, 60.0 KCal/mol/rad^2)
# 4      OA-C-CH2   (115.0, 60.0 KCal/mol/rad^2)
# 5      O=C-CH2          (121.0, 60.0 KCal/mol/rad^2)
# 6      C-CH2-CH2; CH2-CH2-CH2; CH2-CH2-CH3
#                  (111.0, 55.0 KCal/mol/rad^2)
#
# Angle potential parameters
angle_coeff    1          0.0     109.47
angle_coeff    2         47.5     109.5
angle_coeff    3         60.0     124.0
angle_coeff    4         60.0     115.0
angle_coeff    5         60.0     121.0
angle_coeff    6         55.0     111.0


## DIHEDRALS (dihedral_type       description      parameters)
# 1      HO-OA-C-CH2; HO-OA-C=O
#                  (180 deg, 4.0 KCal/mol, n=2, wt_factor=0.0)
# 2    OA-C-CH2-CH2; O=C-CH2-CH2
#                  (  0 deg, 0.1 KCal/mol,   6,    0.0)
# 3      C-CH2-CH2-CH2; CH2-CH2-CH2-CH2; CH2-CH2-CH2-CH3
#                  (  0 deg, 1.4 KCal/mol,   3,    0.0)
dihedral_coeff 1          4.0     2         180      0.0
dihedral_coeff 2          0.1     6           0      0.0
dihedral_coeff 3          1.4     3           0      0.0


## IMPROPERS (improper_type       description      parameters)
# 1      C OA CH2 O  (40 KCal/mol/rad^2, 0.0 deg)
improper_coeff         1        40       0.0

## SPECIAL BONDS (define the 1-4 interactions)
```

```
special_bonds       charmm

# Groups
group               all   type >= 1
group               water type <= 3
group               FA    type >= 4
group               OW    type 1

# Computes
compute             SystemTemp all temp
#compute            RadDensity all radDensity

# Fixes
fix                 1 all   nve
fix                 2 all    momentum 1 linear 1 1 1 angular
fix                 3 all    shake 0.0001 100 0 b 1 a 1
fix                 4 all    temp/rescale 1 260.0 260.0 1.0 1.0
fix                 5 all    recenter 0.0 0.0 0.0 units box
#fix                6 OW   rdf 100 water2440.rdf 100 1 1

# Generate initial velocity
velocity            all create 260.0 123456 mom yes rot yes

thermo_style        custom step temp pe ke etotal
thermo              1000
dump                1 all atom 5000 water2440fac12_505.dump
restart             25000 water2440fac12_505.*.restart

timestep            2.0
run_style           verlet
run                 50000
```

9 References

1. Friedlander, S. K. *Smoke, Dust and Haze. Fundamentals of Aerosol Dynamics*. Second Edition, Oxford University Press. 2000.
2. Seinfeld, J. H.; Pandis, S. N. *Atmospheric Chemistry and Physics: From Air Pollution to Climate Change*. Second Edition, John Wiley & Sons. 2006.
3. Buseck, P. R.; Pofsai, M. *Airborne minerals and related aerosol particles: Effects on climate and the environment*. Proc. Natl. Acad. Sci. USA 1999, 96, 3372.
4. Solomon, S.; Qin, D.; Manning, M.; Chen, Z.; Marquis, M.; Averyt, K. B.; Tignor, M.; Miller, H. L. (eds). *IPCC, 2007:Climate Change 2007: The Physical Science Basis. Contribution of Working Group I to the Fourth Assessment Report of the Intergovernmental Panel on Climate Change*. Cambridge University Press, Cambridge, United Kingdom and New York, NY, USA, 996 pp. 2007.
5. Fitzgerald, J. *Marine aerosols: A review*. Atmos. Environ, 25, 533-545, 1991.
6. Blanchard, D. C. *Sea-to-air transport of surface active material*. Science, 146, 396-397, 1964
7. Gill, P. S.; Graedel, T. E.; Weschler, C. J. *Organic films on atmospheric aerosol particles, fog droplets, cloud droplets, raindrops and snowflakes*. Rev. Geophys. Space Phys., 21, 903-920, 1983.
8. Middlebrook, A. M.; Murphy, D. M.; Thomson, D. S. *Observations of organic material in individual marine particles at Cape Grim during the First Aerosol Characterization Experiment (ACE 1)*. J. Geophys. Res., 103, 16475-16483, 1998.

9. Ellison, G. B.; Tuck, A. F.; Vaida, V. *Atmospheric Processing of Organic Aerosols*. J. Geophys. Res. Vol. 104, D9, p 11633, 1999.

10. Langmuir, I. *The constitution and fundamental properties of solids and liquids, II, Liquids.* 1917. J. Am. Chem. Soc., 39, 1848-1906, 1917.

11. Blodgett, K. B. *Films built by depositing successive monomolecular layers on a solid surface*. J. Am. Chem. Soc., 57, 1007-1022, 1935.

12. Tervahattu, H.; Hartonen, K.; Kerminen, V.-M.; Kupiainen, K.; Aarnio, P.; Koskentalo, T.; Tuck, A. F.; Vaida, V. *New evidence of an organic layer on marine aerosols*. J. Geophys. Res. (Atmos.) 2002, 107, D7

13. Tervahattu, H.; Juhanoja, J.; Kupiainen, K. *Identification of an organic coating on marine aerosol particles by TOF-SIMS.* J. Geophys. Res. (Atmos.) 2002, 107, D16.

14. Ellison, G. B.; Tuck, A. F.; Vaida, V. *Atmospheric Processing of Organic Aerosols*. J. Geophys. Res. Vol. 104, D9, p 11633, 1999.

15. Israelachvili, J. *Intermolecular & Surface Forces*, 2nd ed.; Academic Press: London, 1991.

16. Wyslouzil, B. E.; Wilemski, G.; Strey, R.; Heath, C. H.; Dieregsweiler, U. *Experimental evidence for internal structure in aqueous-organic nanodroplets.* Phys. Chem. Chem. Phys. 2006, 8, 54-57.

17. Li, J. S; Wilemski, G. *A structural phase diagram for model aqueous organic nanodroplets.* Phys. Chem. Chem. Phys. 2006, 8, 1266.

18. Henz, B.; Hawa, T.; Zachariah, M. R. *Mechano-Chemical Stability of Gold Nanoparticles Coated with Alkanethiolate SAM's*. Langmuir. In press.

19. Manna, A.; Imae, T.; Aoi, K.; Okazaki, M. *Gold Nanoparticles Surface-confined by Hybrid Self-Assembled Monolayers of Dendrimer and Dodecanethiol*. Mol. Sim. 2003, 29(10–11), 661–665.

20. Magnusson, M. H.; Duppert, K.; Malm, J.–O.; Bovin, J.–O.; Samuelson, L. *Size-Selected Gold Nanoparticles by Aerosol Technology*. NanoStructured Materials 1999, 12, 45–48.

21. Chiang, C.–L. *Controlled growth of Gold Nanoparticles in Aerosol-OT/Sorbitan Monooleate/Isooctane Mixed Reverse Micelles.* J. of Colloid and Interface Science 2000, 230, 60–66

22. Kim, J.–U.; Cha, S.–H.; Shin, K.; Jho, J. Y.; Lee, J.–C. *Synthesis of Gold Nanoparticles from Gold(I)-Alkanethiolate Complexes with Supramolecular Structures through Electron Beam Irradiation in TEM.* J. Am. Chem. Soc. Communications 2005, 127, 9962–9963.

23. Landman, U.; Luedtke, W. D. *Small is different: energetic, structural, thermal and mechanical properties of passivated nanocluster assemblies.* Faraday Discussions 2004, 125,1–22.

24. Shevade, A. V.; Zhou, J.; Zin, M. T.; Jiang, S. *Phase behavior of mixed self-assembled monolayers of alkanethiols on Au(111): A configurational-bias Monte Carlo simulation study*. Langmuir 2001, 17, 7566–7572.

25. Tsai, D.-H; Zangmeister, R. A.; Pease, L. F.; Tarlov, M. J.; Zachariah, M. R. *Gas-Phase Ion-Mobility Characterization of SAM Functionalized Au Nanaparticles*. Langmuir – in press.

26. Chakraborty, P.; Zachariah, M. R. *'Effective' Negative Surface Tension: A Property of Coated Nanoaerosols Relevant to the Atmosphere*. J. Phys. Chem. A, 2007, 111, 5459-5464.

27. Chakraborty, P; Zachariah, M. R. *Sticking Coefficient and Processing of Water Vapor on Organic Coated Nanoaerosols.* J. Phys. Chem. A, 2008, 112, 966-972.

28. Chandler, D. *Introduction to Modern Statistical Mechanics*. Oxford University Press, New York, 1987.

29. Allen, M. P.; Tildesely, D. J. *Computer Simulation of Liquids*. Oxford Science Publications. 2004.

30. Frenkel, D.; Smit, B. *Understanding Molecular Simulations: From Algorithms to Applications*. Second Edition, *Academic Press*. 2002.

31. Skeel, R. D.; Zhang, G.; Schlick, T. *A Family of Symplectic Integrators: Stability, Accuracy and Molecular Dynamics Application*. *Siam J. Sci. Comp*. Vol. 18, No. 1, pp. 203-222, January 1997.

32. Shelley, J. C; Shelley, M. Y; Reeder, R. C; Bandyopadhyay, S; Klein, M. L. *A coarse grained model for phospholipid simulations*. J. Phys. Chem. B, 2001, 105, 4464-4470.

33. Berendsen, van der Spoel, van Drunen. *GROMACS: A message-passing parallel molecular dynamics implementation*. Comp. Phys. Comm. 91:43–56, 1995.

34. Zhou, Y.; Cook, M.; Karplus, M. *Protein Motions at Zero-Total Angular Momentum: The Importance of Long-Range Correlations.* Biophys. J., Vol. 79, 2000, 2902.

35. Plimpton, S. J. *Fast Parallel Algorithms for Short-Range Molecular Dynamics.* J. of Comp. Phys. 117, 1-19 (1995).

36. Dobson, C. M; Ellison, G. B; Tuck, A. F; Vaida, V. *Atmospheric aerosols as prebiotic chemical reactors.* Proceedings of the National Academy of Sciences, Vol. 97, No 22, p 11864, 2000.

37. Safran, S. *Statistical Thermodynamics of Surfaces, Interfaces and Membranes*. Addison-Wesley, 1994.

38. Facchini, M. C; Decesari, S; Mircea, M; Fuzzi, S; Loglio, G. *Surface Tension of Atmospheric Wet Aerosol and cloud/fog droplets in relation to their organic carbon content and chemical composition.* Atmospheric Enviroment, 34 (2000), 4853-4857.

39. Shelley, J. C; Shelley, M. Y; Reeder, R. C; Bandyopadhyay, S; Klein, M. L. *A coarse grained model for phospholipid simulations*. J. Phys. Chem. B, 2001, 105, 4464-4470.

40. Shelley, J, C; Shelley, M. Y; Reeder, R. C; Bandyopadhyay, S; Moore, P. B; Klein, M. L. *Simulations of phospholipids using a coarse grain model*. J. Phys. Chem. B, 2001, 105, 9785-9792.

41. Lopez, C. F; Moore, P. B; Shelley, J. C; Shelley, M. Y; Klein, M. L. *Computer simulation studies of biomembranes using a coarse grain model*. Comput. Phys. Comm. 2002, 147, 1, 1-6.

42. Thompson, S. M; Gubbins, K. E; Walton, J. P. R. B; Chantry, R. A. R; Rowlinson J. S. *A Molecular Dynamics study of liquid drops*. J. Chem. Phys. 81, 530, 1984.

43. Rowlinson, J. S; Widom, B. *Molecular Theory of Capillarity*. Clarendon, Oxford. 1982.

44. Sorjamaa, R; Svenningsson, B; Raatikainen, T; Henning, S; Bilde, M; Laakonsen, A. *The role of surfactants in Kohler theory reconsidered.* Atmos. Chem. Phys., 4, 2107-2117, 2004.

45. Li, Z; Williams, A. L; Rood, M. J. *Influence of soluble surfactants properties on the activation of aerosol particles containing inorganic solute.* Journal of the Atmospheric Sciences. Vol. 55, p 1859, 1998.

46. Moller, M. A; Tildesley, D. J; Kim, K. S; Quirke, N. *Molecular Dynamics Simulations of a Langmuir-Blodgett Film*. J. Chem. Phys. 94, 1991, 8390.

47. Lindahl, Hess, van der Spoel. *Gromacs 3.0: A package for molecular simulation and trajectory analysis*. J. Mol. Mod. 7:306–317, 2001.

48. Berendsen, Postma, Gunsteren, Hermans. *Interaction models for water in relation to protein hydration*. B. Pullman (ed), "Intermolecular Forces", 331, 1981.

49. Berendsen, Grigera, Straatsma. *The missing term in effective pair potentials*. J. Phys. Chem., 1987, 91, pp 6269.

50. Miyamoto, Kollman. *Settle: An analytical version of the Shake and Rattle algorithms for rigid water models*. J. Comp. Chem., 13, 1992, pp 952.

51. Vieceli, J; Roeselova, M; Tobias. D. J. *Accommodation coefficients for water vapor at the air/water interface*. Chem. Phys. Let. 393 (2004) 249-255.

52. Chuang, P.Y.; Charlson, R. J.; Seinfeld, J. H. *Kinetic limitations on droplet formation in clouds.* Nature 390 (1997) 594.

53. Nenes A.; Ghan S.; Abdul-Razzak H.; Chuang, P. Y.; Seinfeld, J. H. *Kinetic limitations on cloud droplet formations and impact on cloud albedo.* Tellus 53B (2001) 133.

54. Morita, A.; Sugiyama, M.; Kameda, H.; Koda, S.; Hanson, D. R. *Mass Accommodation Coefficient of Water: Molecular Dynamics Simulation and Revised Analysis of Droplet Train/Flow Reactor Experiment*. J. Phys. Chem. B, 108 (26), 9111-9120, 2004.

55. Li, Z.; Wang, H. *Gas-Nanoparticle Scattering: A Molecular View of Momentum Accommodation Function*. Phys. Rev. Let. 95, 014502 (2005).

56. Gilbert, R. G.; Smith, S. C. *Theory of Unimolecular and Recombination Reactions*. Blackwell Scientific Publications, Oxford, London, 1990.

57. S. J. Plimpton, Fast Parallel Algorithms for Short-Range Molecular Dynamics, J Comp Phys, 117, 1-19 (1995).

58. Zakharov, V. V.; Brodskaya, E. N.; Laakonsen, A. Surface Tension of water droplets: a molecular dynamics study of model and size dependencies. J. Chem. Phys., 107 (24), 1997.

59. Stokes, G. G. *On the effect of the internal friction of fluids on the motion of pendulums*. Proc. Cambridge Philos. Soc. 9, 8 (1851).

60. Brenner, H. *The slow motion of a sphere through a viscous fluid towards a plane surface*. Chem. Eng. Sci. 16, 242 (1961).

61. Alley, W. E.; Alder, B. *Generalized transport coefficients for hard spheres.* J. Phys. Rev. A 27, 3158 (1983).

62. Vergeles, M.; Keblinski, P.; Kopli, J.; Banavar, J. R. Stokes Drag at Molecular Level. Phys. Rev. Let. 75(2), 232, 1995.

63. Vergeles, M.; Keblinski, P.; Koplik, J.; Banavar, J. R. Stokes drag and lubrication flows: A molecular dynamics study. Phys. Rev. E, 53(5), 4852, 1996.

64. Koplik, J.; Banavar, J. R.; Willemsen, J. F. *Molecular dynamics of fluid flow at solid surfaces*. Phys. Fluids A 1, 781, 1989.

65. McNeill, V. F; Patterson J; Wolfe, G. M; Thornton, J. A. The effect of varying levels on the reactive uptake of N_2O_5 to aqueous aerosols. Atmos. Chem. Phys., 6, 1635-1644, 2006.

66. McNeill, V. F; Wolfe, G. M; Thornton, J. A. The oxidation of oleate in submicron aqeous salt aerosols: evidence of a surface process. J. Phys. Chem. A, 2007, 111, 1073- 1083.